E9074
10-1-96

NASA Contractor Report 195375

Quick-Mixing Studies Under Reacting Conditions

May Y. Leong and G.S. Samuelsen
University of California
Irvine, California

September 1996

Prepared for
Lewis Research Center
Under Grant NAG3–1110

National Aeronautics and
Space Administration

QUICK-MIXING STUDIES UNDER REACTING CONDITIONS

CONTRACTORS REPORT

May Y. Leong
G. S. Samuelsen

UCI-ARTR-95-8

June 1995

UNIVERSITY OF CALIFORNIA

IRVINE CA 92697-3550

ABSTRACT

Quick-Mixing Studies Under Reacting Conditions

The low-NO_x emitting potential of rich-burn/quick-mix/lean-burn (RQL) combustion makes it an attractive option for engines of future stratospheric aircraft. Because NO_x formation is exponentially dependent on temperature, the success of the RQL combustor depends on minimizing high temperature stoichiometric pocket formation in the quick-mixing section. An experiment was designed and built, and tests were performed to characterize reaction and mixing properties of jets issuing from round orifices into a hot, fuel-rich crossflow confined in a cylindrical duct. The reactor operates on propane and presents a uniform, non-swirling mixture to the mixing modules. Modules consisting of round orifice configurations of 8, 9, 10, 12, 14, and 18 holes were evaluated at a momentum-flux ratio of 57 and jet-to-mainstream mass-flow ratio of 2.5. Temperatures and concentrations of O_2, CO_2, CO, HC, and NO_x were obtained upstream, downstream, and within the orifice plane to determine jet penetration as well as reaction processes. Jet penetration was a function of the number of orifices and affected the mixing in the reacting system. Of the six configurations tested, the 14-hole module produced jet penetration close to the module half-radius and yielded the best mixing and most complete combustion at a plane one duct diameter from the orifice leading edge. The results reveal that substantial reaction and heat release

occur in the jet mixing zone when the entering effluent is hot and rich, and that the experiment as designed will serve to explore satisfactorily jet mixing behavior under realistic reacting conditions in future studies.

TABLE OF CONTENTS

LIST OF FIGURES

LIST OF TABLES

NOMENCLATURE

C_d	discharge coefficient
DR	jet-to-mainstream density ratio
FAR	fuel-air ratio
d	orifice axial height, or round hole diameter
J	jet-to-mainstream momentum-flux ratio = $(\rho V^2)_{jet} / (\rho V^2)_{main}$
MR	jet-to-mainstream mass-flow ratio
P	pressure
ppm	part per million by volume
r	radial distance from center of module
R	radius of the quick-mix module
R_1	radius one-third of R from the center
R_2	radius two-thirds of R from the center
SLPM	standard liters per minute
T_i	temperature of component i (i = jet, mainflow)
V_{ref}	reference velocity
VR	jet-to-mainstream velocity ratio
z	axial distance from leading edge of orifice
ϕ	equivalence ratio = $(\text{fuel/air})_{actual}/(\text{fuel/air})_{stoichiometric}$

CHAPTER 1

INTRODUCTION

1.1 Overview

Jet mixing with a crossflow has been well-researched because of its occurrence in a wide range of applications such as pollution control, vertical short takeoff/landing (VSTOL) aircraft, and gas turbine design. Understanding the dynamics of jets interacting with a crossflow is essential in predicting jet trajectory and mixing in these systems.

The gas turbine combustor relies heavily on jet-crossflow mixing to achieve flame stability, completion of reaction, and cool uniform exit temperatures. The importance of jet mixing with a crossflow is further evident in the Rich burn-Quick mix-Lean burn (RQL) combustion concept. The RQL scheme is a low-NO_x combustor being considered for powering the next generation fleet of supersonic aircraft (Shaw, 1991). The premise behind the RQL combustor lies in staging the combustion process in fuel-rich and fuel-lean zones to avoid the high temperatures associated with near-stoichiometric combustion. High temperatures encourage the production of NO_x, a pollutant which when released into the upper atmosphere participates in the destruction of stratospheric ozone.

The success of the RQL combustor rests with the performance of the quick-mixing section that bridges the rich and lean zones. Rapid and thorough mixing of jet air with a crossflow of rich products to complete the reaction is desired in order to decrease the formation and residence time of stoichiometric pockets of fluid. These fluid pockets are undesirable because NO_x production is accelerated by the high temperatures induced by stoichiometric conditions.

The key to reducing NO_x formation in the quick-mixing section lies in determining the effect of orifice configurations on jet penetration and mixing uniformity. Investigations have focused on varying flow and geometric parameters to determine configurations that lead to uniform mixing within a specified duct length. Multiple jet mixing experiments have mainly been performed under non-reacting rather than reacting conditions because fewer complications are involved. Reacting flow investigations reported in the literature have mainly consisted of numerical studies, and the few existing experimental reacting studies have not been directed at understanding the dynamics of jet mixing with a rich reacting crossflow.

1.2 Research Goal and Objectives

Previous studies conducted by Hatch, *et al.* (1996), Kroll, *et al.* (1996), and Sowa, *et al.* (1994) investigated the mechanistic properties of jet mixing with a heated cylindrical crossflow under non-reacting conditions. The current research project builds upon the non-reacting experiments by initiating performance studies of the cylindrical quick-mixing region under reacting conditions, with the goal being to characterize jet mixing and reaction for selected orifice configurations.

The objectives that need to be accomplished in order to attain the research goal are:

1) Conduct a detailed literature review on research and issues related to the RQL combustor.
2) Design, construct, and validate a test stand with reacting flow capability.
3) Ensure experimental apparatus integrity and rich product uniformity.
4) Design a test protocol and matrix, and conduct reacting flow experiments to measure temperature and species concentration profiles.
5) Analyze acquired data.

CHAPTER 2

BACKGROUND

2.1 High Speed Civil Transport Program

A joint effort between the National Aeronautics and Space Administration (NASA) and aircraft-related industries has been formed to develop technology needed to support production of a fleet of High Speed Civil Transport (HSCT) aircraft by the twenty-first century. This second-generation civilian supersonic aircraft (Figure 2.1) is planned to become more commercially successful than its Concorde predecessor with its improved fuel efficiency and capability to transport three times as many passengers at twice the distance (Strack and Morris, 1988). Certain technological issues need to be resolved, however, before such a fleet of supersonic aircraft can be realized.

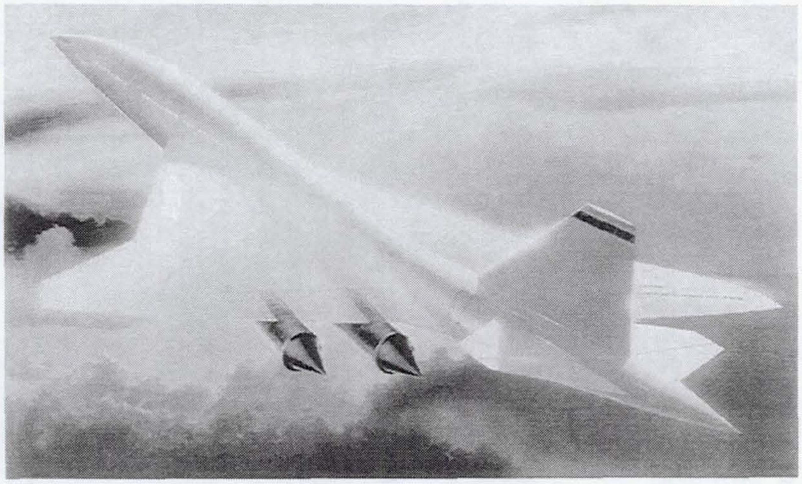

Figure 2.1 High Speed Civil Transport

The High Speed Research Program (HSRP) was initiated in 1990 by NASA to study the issues involved with developing and supporting a fleet of advanced supersonic aircraft. Although technical and economic issues require consideration in ensuring the viability of the program, environmental barriers relating to noise and emissions are preventing the aircraft from leaving the ground. While the noise generated from the HSCT aircraft mainly impacts communities in the flight path or vicinity of airports, emissions into the atmosphere may produce adverse effects over a global area and population.

The HSCT aircraft is designed to cruise between 18.3-27.4 km (60-90,000 ft.) at speeds of Mach 2-3 for optimal fuel economy (Koff, 1994). The planned flight altitude falls in the domain of the stratosphere, a stable region in the atmosphere where the ozone layer resides. In the 1970s an evaluation of the impact of stratospheric flight on the environment was carried out by the Climatic Impact Committee formed by the National Research Council, the National Academy of Sciences, and the National Academy of Engineering (Grobecker, *et al.*, 1974). The committee determined that of all the emissions from stratospheric aircraft (including water, carbon dioxide, carbon monoxide, sulfur oxides, nitrogen oxides, and soot), nitrogen oxides (NO_x) were a primary concern because of their deleterious effect on the stratospheric ozone layer (Climatic Impact Committee, 1975). Due to current adverse public opinion toward environmentally detrimental technologies, the industrial sector is hesitating in developing the HSCT aircraft until its potential for depleting stratospheric ozone is resolved.

2.2 Stratospheric Ozone Depletion

The stratosphere contains up to 90% of the ozone (O_3) in the entire atmosphere, with maximum concentrations found between 15-25 km in the lower stratosphere (Rowland, 1991). The ozone that resides in the stratosphere forms a thin blanket over the Earth which absorbs the UV-B waveband, or ultraviolet radiation shorter than 320 nm. UV-B radiation destroys cells of plants and animals and leads to skin cancer, eye cataracts, and deterioration of the immune system in humans. The destruction of the ozone layer increases terrestrial exposure to harmful UV-B radiation and increases urban air pollution caused by the photolysis of formaldehyde in photochemical smog (Masters, 1991). On an atmospheric scale, the gradual loss of the ozone layer decreases the stratospheric temperature and consequently, the circulation in the atmosphere (Wayne, 1985).

The stratospheric ozone production and destruction cycle can be described in the following series of steps (equations 2.1-2.4) proposed by Chapman (1930):

$$O_2 + UV\ (\lambda < 242\text{nm}) \rightarrow O + O \qquad (2.1)$$

$$O + O_2 + M \rightarrow O_3 + M \qquad (2.2)$$

$$O_3 + UV \rightarrow O + O_2 \qquad (2.3)$$

$$O + O_3 \rightarrow O_2 + O_2 \qquad (2.4)$$

where λ represents the radiation wavelength. The Chapman reactions, however, consistently overpredict the amount of ozone recorded in experiments. The explanation for the occurrence of lower than expected concentrations of ozone was first suggested by Bates and Nicolet (1950) as being caused by destructive catalytic processes. The following series of free radical catalytic reactions (equations 2.5-2.6) reflecting the additional destruction of ozone was then appended to the sequence to compensate for the overprediction:

$$X + O_3 \rightarrow XO + O_2 \qquad (2.5)$$

$$XO + O \rightarrow X + O_2 \qquad (2.6)$$

$$\text{net} \quad O + O_3 \rightarrow O_2 + O_2 \qquad (2.7)$$

where X is a catalyst representing either HO_x, NO_x, or ClO_x. The pair of ozone-destroying reactions in equations 2.5 and 2.6 can continue indefinitely until the catalyst X is removed. Unfortunately, the catalyst may linger for a long period of time in the stratosphere due to the temperature inversion which inhibits the vertical mixing that would normally aid in its removal.

The role of NO_x in stratospheric ozone destruction via the catalytic reactions emphasizes the need to reduce NO_x emissions from the gas turbine combustors that will power the HSCT aircraft. In order to control NO_x production during the combustion process, the mechanism and chemistry behind NO_x formation must be understood.

2.3 NO_x Formation

Oxides of nitrogen (NO_x) are pollutants formed during the combustion process that are partially responsible for the degradation of the ozone layer. The NO_x label represents both nitric oxide (NO) and nitrogen dioxide (NO_2). However, because NO_2 comprises less than 10% of the total amount of NO_x, NO_x is almost all NO.

During the combustion process, NO_x can be formed via three pathways known as prompt, fuel, and thermal NO_x. Prompt NO_x is formed in the primary reaction zone during the initial stages of combustion when hydrocarbon radicals or fuel fragments attack atmospheric nitrogen molecules (N_2) (Fenimore, 1971). The resulting atomic nitrogen product from the dissociation of N_2 reacts with oxygen molecules to form NO. Prompt NO_x formation, however, comprises a relatively small fraction of the total NO_x formed.

Fuel NO_x is formed when the nitrogen in the fuel is oxidized. The fuel-bound nitrogen is typically bonded to carbon and hydrogen in the form of ammonia, pyridine, and other amines (Glassman, 1987). Fuel NO_x can be controlled by choosing fuels with lower nitrogen content.

Thermal NO_x formed from atmospheric nitrogen is the main source of NO_x emissions for combustion systems operating at high temperatures and with long residence times. The series of reactions listed as equations 2.8 and

2.9, known as the Zeldovich mechanism (Zeldovich, 1946), describes the production of thermal NO_x.

$$N_2 + O \rightarrow NO + N \qquad (2.8)$$

$$N + O_2 \rightarrow NO + O \qquad (2.9)$$

The first reaction (equation 2.8) is the rate-limiting step because it requires a high activation energy to initiate the reaction by breaking the triple bond that holds the nitrogen molecule together.

For rich and near-stoichiometric flames the second reaction (equation 2.9) can be replaced by the extended Zeldovich mechanism listed as equation 2.10.

$$N + OH \rightarrow NO + H \qquad (2.10)$$

The dependence of the NO reaction rate on temperature is shown in Figure 2.2. Above a temperature of 1800K (2780°F) the reaction rate constant and hence production of NO increases exponentially. To control thermal NO production, the temperature of the reaction should be maintained below this critical temperature.

The reaction temperature is dependent on the fuel-air equivalence ratio ϕ, defined in equation 2.11 as

$$\phi = \frac{(\text{fuel}/\text{air})_{\text{actual}}}{(\text{fuel}/\text{air})_{\text{stoichiometric}}} \qquad (2.11)$$

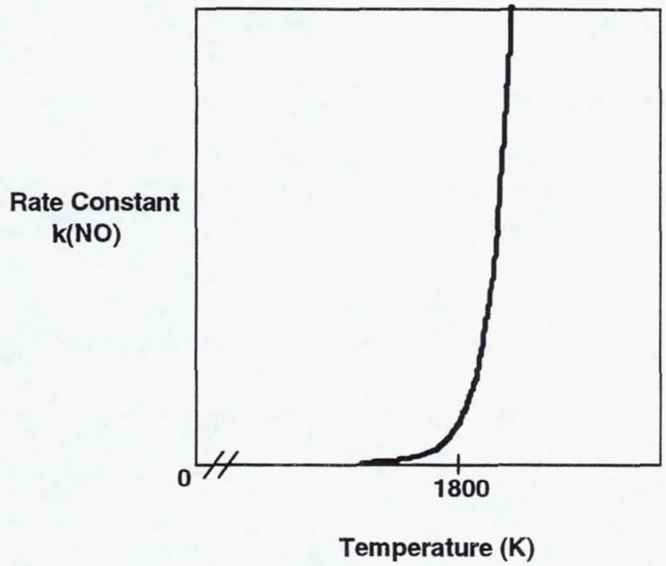

Figure 2.2 Effect of Temperature on NO Reaction Rate
(Adapted from Samuelsen, 1975)

or the overall ratio of the actual to stoichiometric fuel-air ratios. A reaction that is stoichiometric ($\phi = 1$) contains no excess fuel or air in the combustion products. At near-stoichiometric conditions the adiabatic flame temperature, or the highest theoretical reaction temperature, is attained. As the reactant composition approaches fuel-rich ($\phi > 1$) or fuel-lean ($\phi < 1$) conditions, temperatures decrease sharply. The NO formation dependency on equivalence ratio, shown in Figure 2.3, shows a bell-shaped curve that also corresponds to flame temperature dependency on equivalence ratio. The peak of the curve is shifted slightly toward the lean condition due to an abundance of oxygen radicals. This O-atom overshoot slightly increases the NO formation rate at leaner conditions.

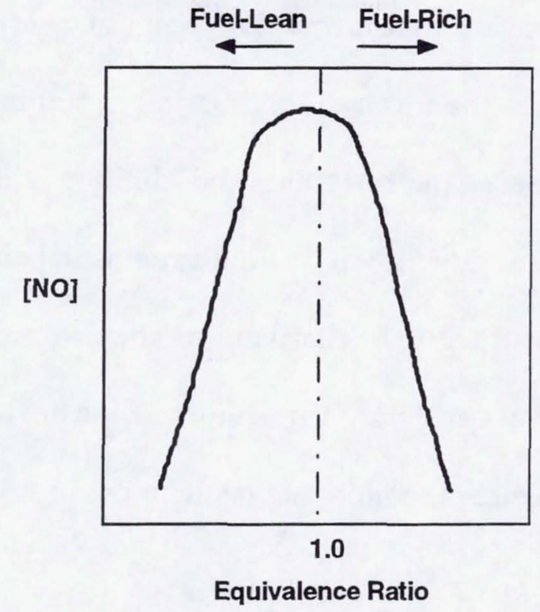

Figure 2.3 Effect of Equivalence Ratio on NO Formation
(Adapted from Samuelsen, 1975)

Because high inlet temperatures from the compressor stage contribute to the even higher combustion temperatures occurring in the combustor, the thermal mechanism is the primary mode of NO_x production in a gas turbine. Control of reaction temperature by varying the equivalence ratio and minimizing the residence time of the reaction at high temperatures is the key to reducing NO_x production rates in a gas turbine combustor.

2.4 The Gas Turbine Combustor

2.4.1 Description

In a typical aircraft engine the combustor is situated between the compressor and turbine (Figure 2.4). Using the hot air from the compressor stage, the combustor transforms the chemical energy in fuel into the heat energy that drives the turbine. The basic gas turbine combustor (Figure 2.5) consists of primary, intermediate, and dilution zones. The primary zone houses the dome region in which liquid fuel is vaporized and mixed with air. Additional air is added to the partially combusted products in the intermediate zone to complete the reaction. The dilution zone mixes in air with the complete combustion products to tailor the gas temperatures to turbine blade material specifications.

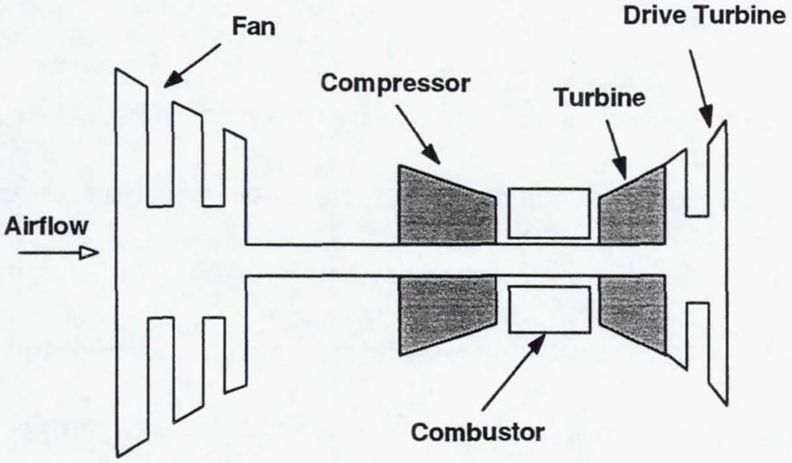

Figure 2.4 Aircraft Engine Schematic (Adapted from Koff, 1994)

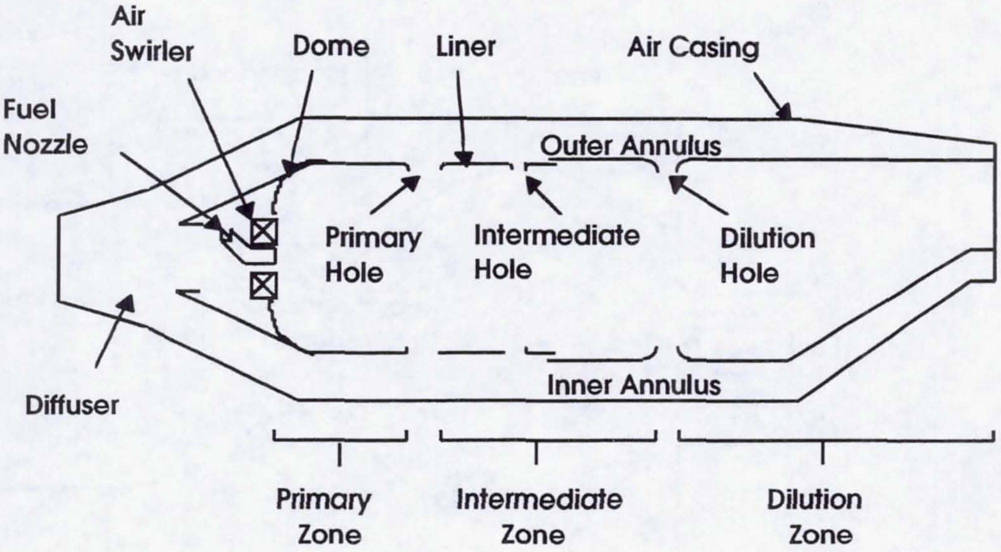

Figure 2.5 Combustor Parts and Zones (Adapted from Lefebvre, 1983)

The combustor operates via a process of continuous combustion in which fresh reactants are continually injected, burned, and exhausted from the combustor (Figure 2.6). A flame stabilizer such as a bluff body or a swirler creates a recirculation region in the primary zone that funnels hot reactants back to the dome region. The hot reactants provide a source of ignition for the fresh fuel and air mixture injected into the combustor.

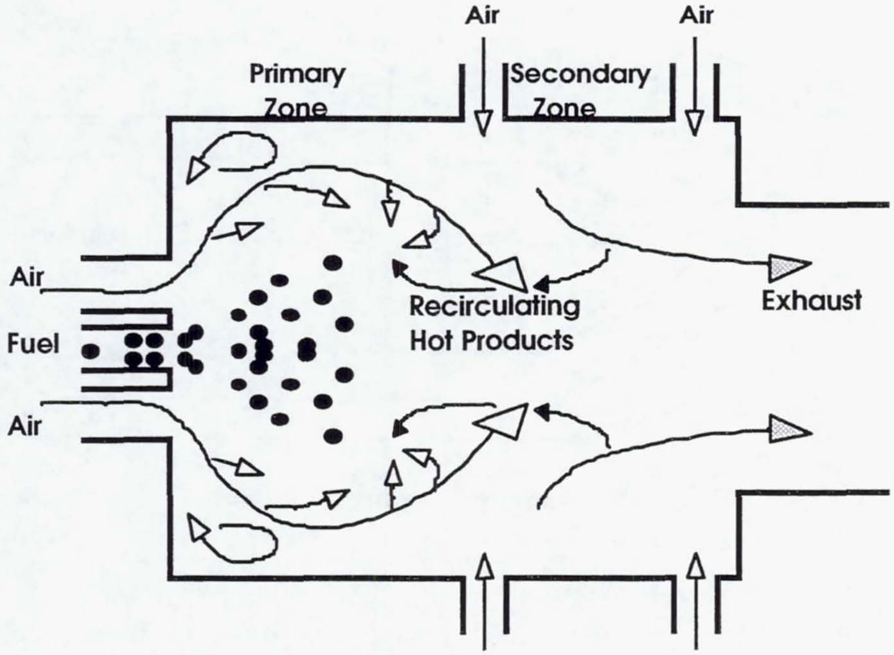

Figure 2.6 Continuous Combustion Aerodynamics
(Adapted from Samuelsen, 1975)

2.4.2 Ultra Low-NO_X Combustors

Current commercial engines produce a NO_x Emissions Index (EI), which is a mass-based measurement of pollutant emitted for a given amount of fuel, between 40-60 g NO_x/kg fuel. Based on this EI, a projected fleet of 500 supersonic aircraft flying in the lower stratosphere could decrease ozone levels annually by 20% on a global basis. However, if the HSCT aircraft complies with the HSRP goal of an EI of 5 g NO_x/kg fuel, the potential destruction of ozone could be as low as 2-3% (Johnston, *et al.*, 1989).

To attain the HSRP EI goal without sacrificing engine efficiency, ultra low-NO_x combustor technologies are being investigated. The most promising concepts for meeting the EI requirement are the Lean Premixed-Prevaporized and the Rich burn-Quick mix-Lean burn systems. These ultra low-NO_x concepts reduce thermal NO_x formation by operating at lean or rich environments to take advantage of the lower temperatures associated with non-stoichiometric equivalence ratios.

The Lean Premixed-Prevaporized (LPP) concept (Figure 2.7) involves a single stage of combustion under fuel-lean conditions. The liquid fuel is completely vaporized and mixed thoroughly with air before combustion. NO_x formation is reduced since the lean operating condition reduces flame temperatures while the avoidance of droplet burning eliminates near-stoichiometric fluid pockets. The LPP concept, however, faces technological

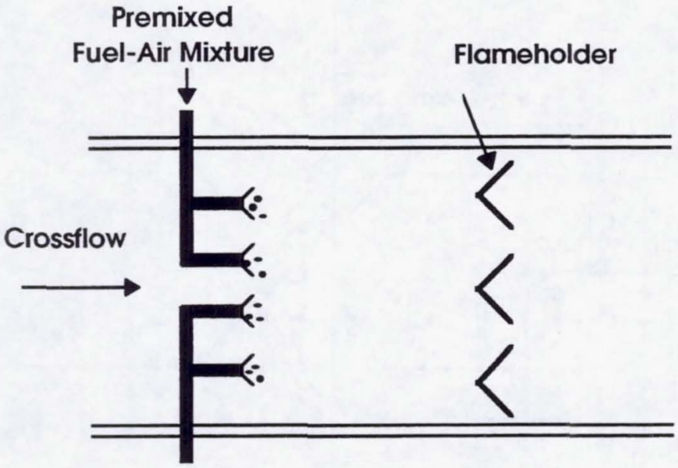

Figure 2.7 Lean Premixed-Prevaporized Concept (Adapted from Shaw, 1991)

and safety issues such as incomplete fuel-air mixing, the potential for autoignition due to high inlet temperatures, flashback (flame propagation back to the fuel source), flame blowout at low power conditions, and poor re-light capability (Lefebvre, 1983).

The Rich burn-Quick mix-Lean burn (RQL) combustor (Figure 2.8) has a wider combustion stability limit and does not incur the hazards of autoignition apparent in the LPP combustor. The RQL combustor was originally conceived as a means to control fuel NO_x because a fuel-rich environment decreases fuel-bound nitrogen conversion to NO_x (Tacina, 1990). However, the concept is being applied to thermal NO_x reduction because it operates on a two-stage combustion process which limits the time spent at near-stoichiometric conditions. Fuel and air are first burned in a fuel-rich environment with a limited amount of oxygen available for NO production. The rich products are then rapidly mixed with jets of air in the quick-mixing region to bring the

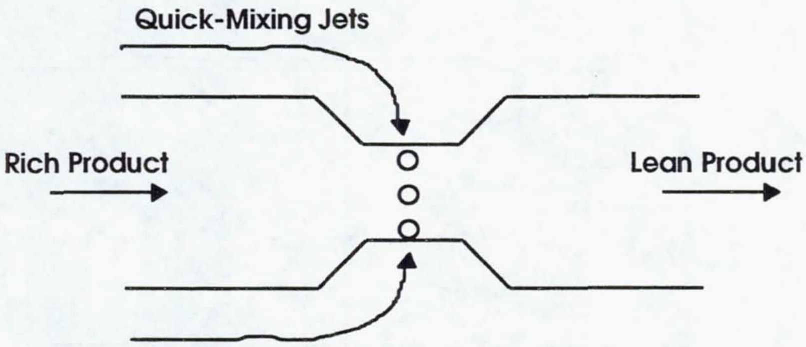

Figure 2.8 Rich Burn-Quick Mix-Lean Burn Concept

reaction to completion in a fuel-lean environment. The quick-mixing section is necked-down to prevent the backflow of products into the rich zone.

In a literature review of experiments performed on the LPP and RQL combustors, Tacina (1990) determined that the LPP combustor produces a lower amount of NO_x than the RQL combustor. The higher NO_x emissions from the RQL combustor was attributed to the near-stoichiometric fluid pockets formed in the quick-mixing section. Though the RQL concept still possesses an ultra low-NO_x emission potential, its ultimate success hinges on the performance of the quick-mixing section that bridges the rich and lean zones. The mixing of jet air with a rich effluent must be performed rapidly and uniformly in order to decrease the time of transition between the two zones and the occurrence of near-stoichiometric fluid pockets. The challenge of optimizing the mixing process in the quick-mix section of the combustor rests with understanding the mechanism behind jet mixing in a crossflow.

2.5 Jets in Crossflow

2.5.1 Single Jet Structure

The jet-in-crossflow problem has been studied extensively due to its broad range of applicability to such diverse fields as gas turbine cooling and staging, fuel-air premixing, vertical short takeoff/landing (VSTOL) aircraft, and pollutant discharge from stacks or pipes.

A round jet entering a crossflow forms a complex three-dimensional free turbulent shear flow (Figure 2.9). The structure of the jet in a crossflow is dependent on the interplay between the jet and crossflow momenta. Toward the base of the jet, the crossflow splits around the jet flow as it would around a solid body. Farther up along the jet, mixing occurs between the two fluids.

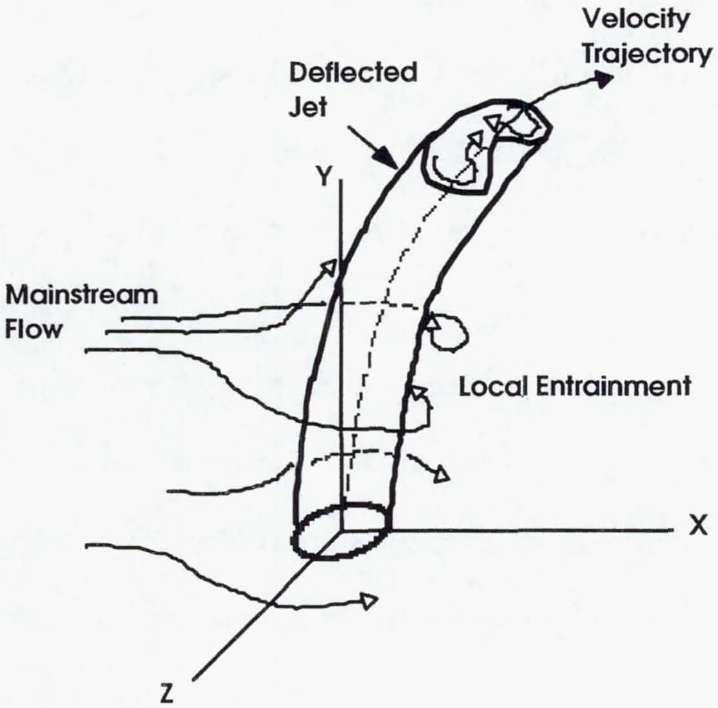

Figure 2.9 Round Jet Deflection and Crossflow Entrainment
(Adapted from Lefebvre, 1983)

A reverse flow region occurring in the wake accelerates fluid from the crossflow and entrains the fluid into the jet. The vorticity of the crossflow interacts with the circular vortical field of the jet to produce a bound vortex shaped like a horseshoe. The vortical field induces the formation of a pair of counter-rotating vortices within the jet that deform the round jet into a kidney shape (Andreopoulos and Rodi, 1984). Downstream from the jet entrance, the diffusion of vorticity weakens the pair of vortices: the jet loses its coherency and subsequently disperses into the crossflow.

The characterization of the single jet in a non-reacting crossflow has been pursued in experimental and analytical modeling studies. Turbulence measurements verifying the structure of the jet-crossflow interaction (Andreopoulos and Rodi, 1984; Andreopoulos, 1985; Fearn and Weston, 1974; Kamotani and Greber, 1972; Sherif and Pletcher, 1989) as well as temperature distributions of heated jet mixing with a crossflow have been obtained (Kamotani and Greber, 1972). Analytical models have been developed that characterize the vortex behavior of a hot or cold jet in a crossflow (Karagozian, *et al.*, 1986) and that predict the jet vortex trajectory (Karagozian, 1986). These theoretical studies contribute to the understanding of the general structure of a single jet in a crossflow, and subsequently help in the analysis of multiple jet mixing in a crossflow.

2.5.2 Multiple Jets in a Confined Non-Reacting Crossflow

The quick-mixing section of the RQL combustor is comprised of a row of jet orifices spaced around the circumference of the combustor. The crossflow is confined to either a cylindrical or annular combustor geometry. In a confined crossflow problem, flow properties such as the jet-to-mainstream density, mass-flow, and momentum-flux ratios as well as the geometries constraining the jet and crossflow influence the degree of mixing that occurs. The most important flow variable in the confined subsonic crossflow system is the jet-to-mainstream momentum-flux ratio J (Holdeman, 1993), defined in equation 2.12 as

$$J = \frac{(\rho V^2)_{jet}}{(\rho V^2)_{main}} \qquad (2.12).$$

The momentum-flux ratio must be determined before an orifice configuration of a certain number, shape, and placement can be designed.

Extensive experimental and numerical studies on jets in a confined crossflow have been performed under non-reacting conditions to examine the effect of jet orifice configurations on mixing in different duct geometries and at various momentum-flux ratios. Non-reacting studies of jets issuing into rectangular (Bain, *et al.*, 1992, 1994, 1995; Liscinsky, *et al.*, 1992, 1993, 1994, 1996) and cylindrical duct geometries (Hatch, *et al.*, 1995a, 1995b; Howe, *et al.*, 1991; Kroll, *et al.*, 1993; Oechsle, *et al.*, 1992, 1993; Smith, *et al.*, 1991; Sowa, *et al.*, 1994; Talpallikar, *et al.*, 1992; Vranos, *et al.*, 1991) have been studied for their applicability to annular and can combustor configurations.

Among the primary goals of non-reacting research on jet mixing in a confined crossflow is to determine orifice configurations that lead to optimal mixing within a specified duct length. In the cylindrical duct geometry, experimental surveys of the effect of momentum-flux ratio and the shape, orientation, and number of orifices on mixing were performed by Hatch, *et al.* (1995a) and Kroll, *et al.* (1993) in order to gain a mechanistic understanding of jet penetration and mixing dynamics. A systematic optimization scheme on experimental data was then undertaken by Sowa, *et al.* (1994) to determine the orifice configurations leading to optimal mixing at a set momentum flux ratio. A non-linear relationship between orifice shape, number, and orientation was revealed with respect to mixing, and allowed for the possibility of more than one optimal orifice combination.

Non-reacting flow experiments have been conducted in lieu of reacting experiments in order to benefit from the advantages (less complicated, more amenable to diagnostic interrogation, more amenable to modeling) of the non-reacting environment. A numerical study by Oechsle, *et al.* (1994) showed that qualitatively similar mixture non-uniformity flow fields were obtained in reacting and non-reacting simulations. Another numerical study by Talpallikar, *et al.* (1992) showed non-reacting and reacting flows exhibiting optimum mixing at the same momentum-flux ratio for a particular slotted orifice configuration. These studies lend credence to the use of non-reacting tests as a screening tool for potential RQL mixing configurations. The screening potential of the non-reacting tests has led to the development of numerical codes that predict NO_x production at actual flight conditions based on non-reacting mixing parameters (Hatch, *et al.*, 1995b). Despite the insight gained from non-reacting tests on jet mixing, an experimental correlation between non-reacting and reacting tests has yet to be established conclusively. Extensive experimental data from reacting tests are required to help validate the use of non-reacting tests in predicting mixing under reacting conditions.

2.5.3 Multiple Jets in a Confined Reacting Crossflow

Numerical studies on jet mixing in a reacting crossflow have been undertaken to characterize the flowfield and NO_x production and to relate the results to non-reacting flows. Howe, *et al.* (1991) varied the jet momentum-flux ratio in a study comparing non-reacting and reacting cases. In both environments, the momentum-flux ratio affected jet penetration depth. The reacting case produced jets with a lower penetration depth than the non-reacting case because the increase in mainstream velocity from the reaction heat release decreased the momentum-flux ratio.

Oechsle, *et al.* (1994) found that at set momentum-flux, mass-flow, and density ratios, the reacting flow exhibited a lower degree of mixing than the non-reacting case. Jet core diffusion and mixing with the crossflow was also found not to be as great in the reacting case as in the non-reacting case. The studies by Howe, *et al.* and Oechsle, *et al.* verify the importance of the momentum-flux ratio mixing parameter in affecting jet penetration and the degree of mixing.

Oechsle and Holdeman (1995) performed a numerical reacting flow study at HSCT flight conditions in a cylindrical geometry. The momentum-flux ratio and orifice shape were varied, and non-uniformity mixing parameters based on equivalence ratio and statistical analysis were used to evaluate jet mixing. Results showed that jet penetration affected both the mixing flow field and NO_x production, as the over- and underpenetration of jets led to higher NO_x production.

A few experimental studies have been performed to characterize the reacting flow in a model gas turbine combustor (Noyce, *et al.*, 1981; Heitor and Whitelaw, 1986). The results, though, are not applicable to the quick-mixing regime of the RQL combustor where rapid jet mixing and high momentum-flux ratios occur. As this moment, only one experimental study specific to the RQL combustor is reported in the open literature. Zarzalis, *et al.* (1992) performed a reacting experiment to determine the effect of different inlet pressures and temperatures on NO_x emissions. However, their study did not address the mechanistic processes governing jet mixing in the quick-mixing section.

This study builds upon the research of Hatch, *et al.* (1996), Kroll, *et al.* (1996), and Sowa, *et al.* (1994) on non-reacting jet mixing in a cylindrical crossflow by initiating similar performance studies under reacting conditions. The purpose of the study was to obtain, for a rich reacting flow in a cylindrical RQL simulation, species concentration and temperature distributions in order to evaluate jet penetration and mixing, and provide an initial database for numerical simulations.

CHAPTER 3

APPROACH

The goal of characterizing jet mixing in a rich reacting crossflow was addressed in four phases: (1) reacting flow facility construction, (2) rich product uniformity evaluation, (3) test matrix specification, and (4) data analysis.

Phase 1: Facility Construction

This phase encompassed the retrofitting of the non-reacting facility used previously by Hatch, *et al.* (1996) and Kroll, *et al.* (1996) for their mixing studies. The upgraded facility features a refractory-lined can combustor with a removable top section to insert a flow conditioner, an aluminum cylindrical chamber that serves as a plenum feed for the quick-mix jets, and quartz modules to house the reaction in the quick-mixing regime.

Phase 2: Rich Product Uniformity Evaluation

The design of the rich product generator was an iterative process that involved reconfiguring and interchanging the system with various parts to produce an experiment that was safe to operate as well as able to produce a uniform rich combustion product.

Several options were pursued in achieving an ultimate design that produced a rich zone equivalence ratio ϕ approaching 1.7. Space limitations led to the initial use of a Lean Burn Injector (LBI) to mix fuel and air rapidly in a short combustor length. However, because the swirling inflow of rich products induced by the LBI/swirler assembly was not desirable for the objectives of this study, an alternate means of generating rich products was pursued.

A premixed fuel and air system that used a ceramic foam matrix as a flameholder for the reaction was proposed to replace the swirler as a flame stabilizer. However, the ceramic foam failed to hold the reaction in its porous structure at the desired rich equivalence ratio. The resulting product from the system was also green, which signified the presence of C_2 radicals in the reaction (Glassman, 1987). Species concentration profiles obtained in the green-tinged effluent showed high O_2 concentrations when 0% was expected, high unburned hydrocarbon concentrations, and lower than expected CO and CO_2 concentrations. These observations suggested that the reaction did not attain a residence time that was long enough to convert the radicals to the expected rich product concentrations.

One solution to increasing the residence time was to increase the length of the combustor, but space limitations precluded this option. The final design re-incorporated the swirler in the premixed fuel-air and ceramic foam system. Instead of functioning as a flameholder, the foam was used as a swirl dissipater. Several iterations were required to determine the placement of the foam with respect to the swirler. The resulting scheme placed the foam five duct diameters downstream from the swirler to allow enough distance for the recirculation zone. Rich product evaluations with species concentration and temperature measurements showed the attainment of a relatively uniform product composition.

Phase 3: Test Matrix and Data Grid Design

The reacting experiment was designed as a continuation of the previous non-reacting experiments performed by Hatch, *et al.* (1996), Kroll, *et al.* (1996), and Sowa, *et al.* (1994). The experimental conditions were designed to simulate the conditions tested by Sowa, *et al.* where the momentum-flux ratio J was 40 and the mass-flow ratio was 2.5. These momentum-flux and mass-flow ratios are representative of the design values for the proposed HSCT aircraft engines.

Six modules with 8, 9, 10, 12, 14, and 18 orifices were used for the experiment. The round hole geometry was chosen as the baseline configuration. The choice of the 9-hole configuration was based on the non-reacting optimization results of Sowa, *et al.* which determined that the 9-hole case produced the best mixing at a momentum-flux ratio J of 40. The 8- and 10-hole cases were chosen to bracket the 9-hole case. In the course of testing, it was discovered that the optimum penetration was not obtained with the 9-hole case, and successive tests were performed with the 12-, 14-, and 18-hole modules in order to encompass the overpenetrating to underpenetrating cases.

The elapsed time to traverse to the specified grid point, to wait for the readings to stabilize, and to obtain a datum point lasted between 1.5 to 2 minutes. The time constraint of operating the experiment in one continuous run per module necessitated the use of a coarse data grid across two orifices at six axial locations. Temperature and species concentrations were obtained to evaluate reaction and mixing occurring in the quick-mix module.

Phase 4: Analysis and Evaluation of Data

The temperature and species concentration measurements obtained were processed and graphed to give a pictorial indication of the jet penetration and its effect on mixing and reaction. Recommendations for future tests and improvements were formulated based on the conclusions and experiences gained from the baseline tests and from bringing the reacting experiment to fruition.

CHAPTER 4

EXPERIMENT

4.1 Facility

The atmospheric model RQL combustion facility pictured in Figure 4.1 was designed for fuel-rich reacting flow capability. Air and fuel flows to the up-fired facility were regulated through a flow panel. The experiment

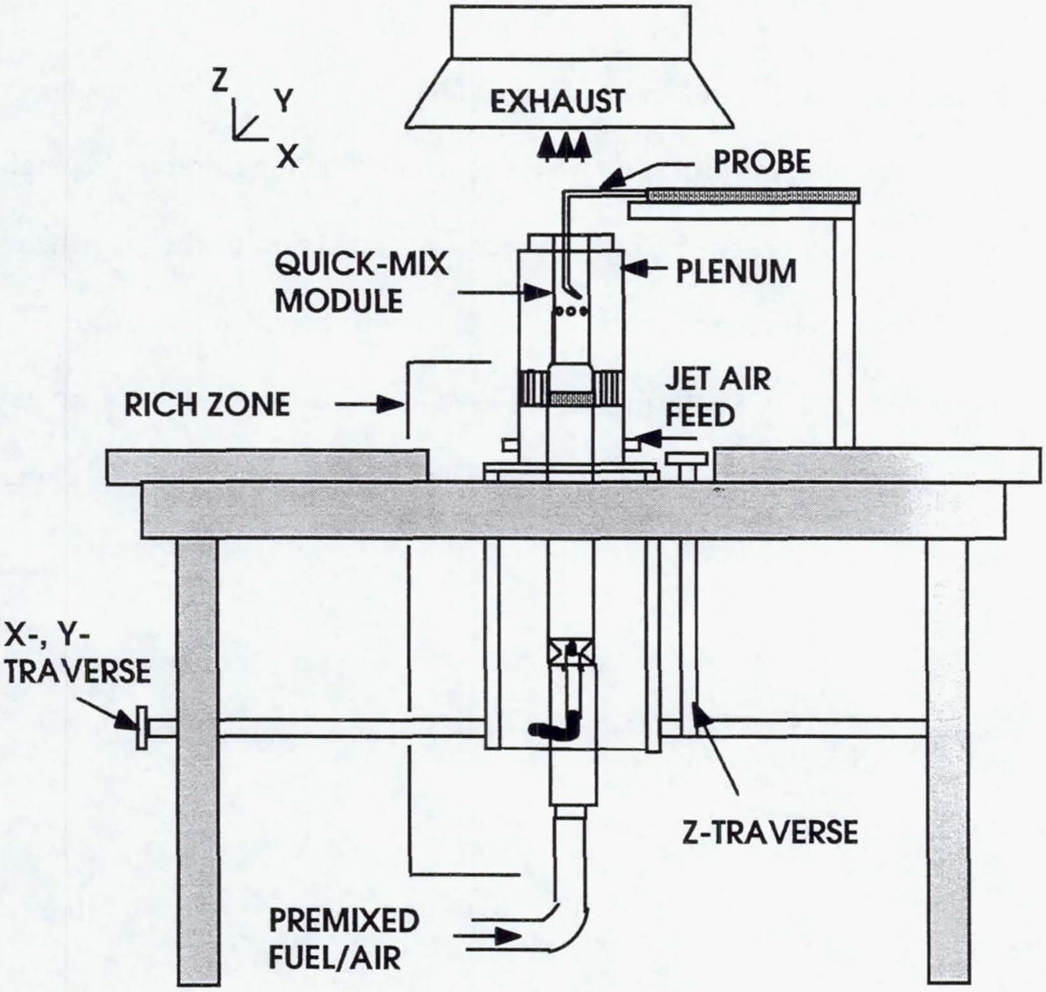

Figure 4.1 Reacting Experiment Facility

consisted of a fuel-air premixing section, a refractory-lined stainless steel can which supported rich combustion, and a plenum-fed quick-mixing section that exhausted into a fume hood. Data were acquired via an intrusive probe that was kept stationary while the entire test stand was traversed.

4.1.1 Air and Fuel Flow Supply

Air and fuel flow regulation was accomplished through a centralized flow panel network shown schematically in Figure 4.2. A flow circuit previously used by Hatch, *et al.* (1996) and Kroll, *et al.* (1996) supplied the air flows to the facility. Dried and filtered air was supplied by an on-site air compressor factory.

The main air flow to the rich combustion section and the air flow to the four independent jet air pathways were metered by sonic venturis. An additional rotameter was used to monitor fuel flow rates to the combustor. The fuel rotameter and sonic venturis were calibrated with a Laminar Flow Element.

The choice of fuel for this experiment was based on operational and chemical considerations. The use of a gaseous fuel was desired in order to eliminate the complexities associated with liquid fuel atomization. Natural gas, though available to the experiment in ample supply, was not utilized because its highly refractory chemistry and rich flammability limit were not able to sustain a stable source of combustion products at an equivalence ratio ϕ

above 1.3 in preliminary tests. The possible impurity and daily variation of natural gas composition also did not ensure a constant fuel composition to the experiment.

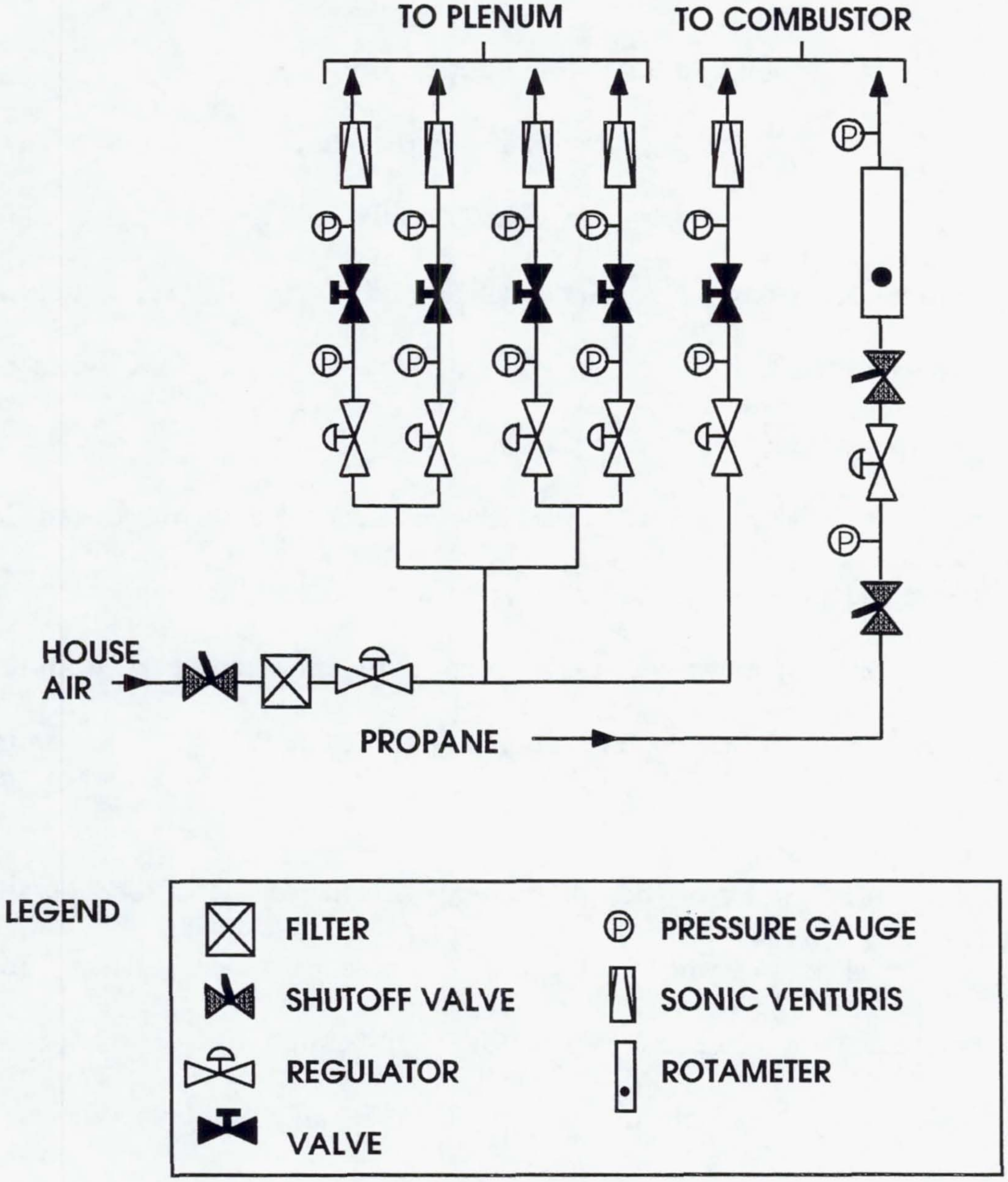

Figure 4.2 Schematic of Flow Panel (Adapted from Hatch, *et al.*, 1996)

Propane (C_3H_8) was chosen because its pyrolysis and thermal decomposition kinetics simulate the properties of jet fuel. Propane also possesses a rich flammability limit above an equivalence ratio ϕ of 2.0, thus enabling the attainment of the rich equivalence ratio desired for the experiment. The fuel was supplied by 94.6 L (25 gal.) tanks of liquefied propane.

4.1.2 Rich Product Generation

The challenge in designing the rich product generator for the experiment was to produce a consistent and uniform effluent of non-swirling, rich products into a cylindrical mixing module. Hardware durability and safety issues applied additional constraints on the design.

The final design of the rich product generator incorporated in the experiment is shown in Figure 4.3. Propane and air at room temperature (25°C) were mixed along a 4.3 m length of a 5 cm diameter pipe before the ignition region. The ignition source was provided by an industrial spark plug placed in the center of a quarl section. The quarl provided a 3.8 cm contraction to prevent the backflow of combustion products.

The pipe and combustor sections upstream and downstream of the quarl were cast with an aluminum oxide (Al_2O_3) refractory material. The refractory material was cast in the upstream pipe section to form an inner diameter of 3.8 cm, and cast in the downstream combustor section to form an inner diameter of

8 cm to match that of the quick-mix module. The wall thickness of the cast ceramic compound was approximately 1.3 cm. The refractory material, which is rated up to 1870°C, insulates the reaction and prolongs the life of the stainless steel combustor.

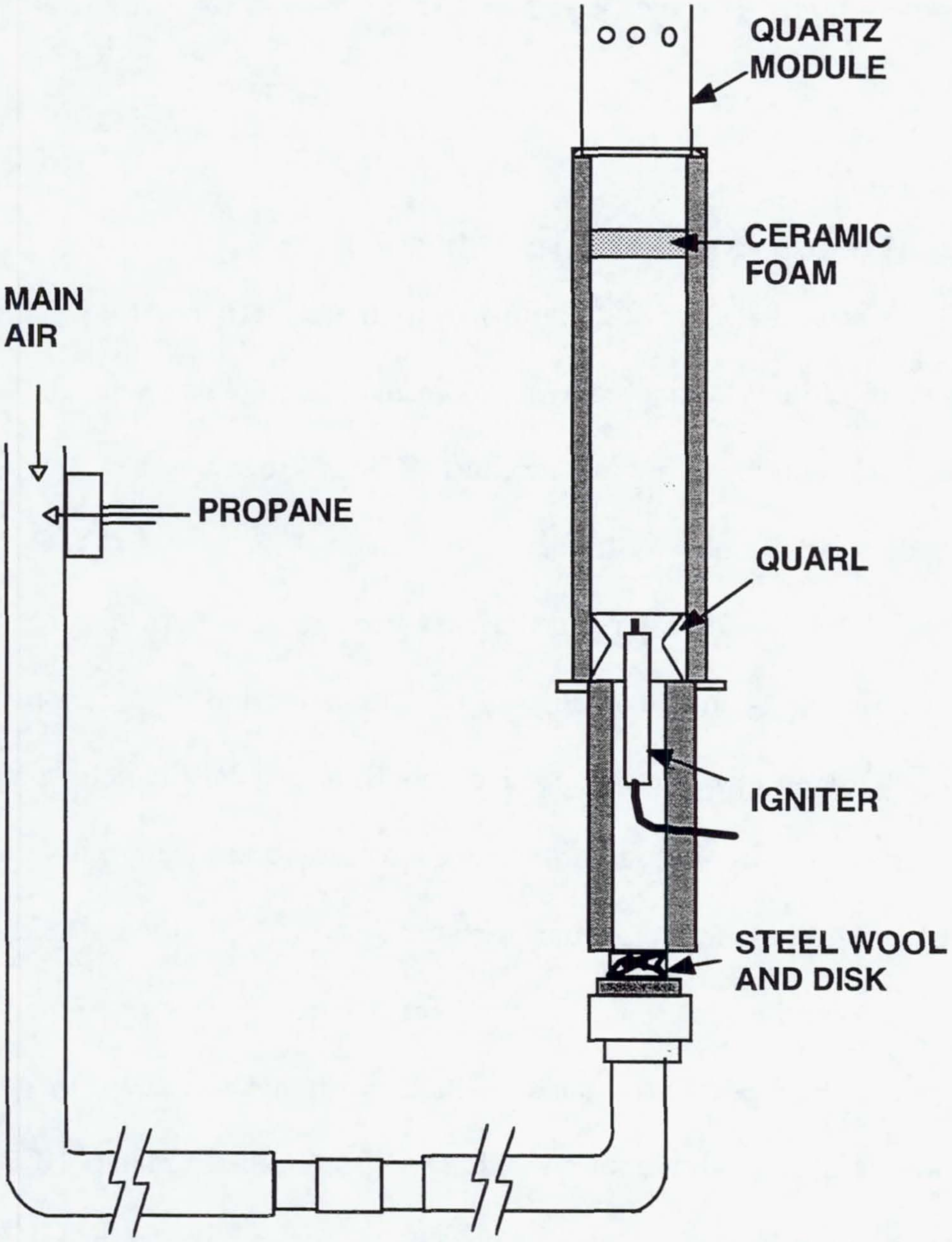

Figure 4.3 Rich Product Generator

The ignition procedure was formulated to eliminate the flashback concern associated with a premixed fuel-air system. The jet air was first supplied to cool the combustor and to prevent the reaction from exiting the module through the orifices. The main air was then supplied to the system at a flow rate of 11.3 standard liters per minute (SLPM), which ensured a 10 m/s flow velocity through the quarl contraction. Assuming a turbulent flame speed of 2 m/s, the velocity provided by the initial main air flow rate was sufficient to prevent flashback. The propane flow rate was increased and the spark plug switch was depressed until ignition occurred. The air flow rate was subsequently increased to a final setting of 22.7 SLPM, whereupon the fuel flow rate was increased to 1.51 SLPM.

A recirculation region was needed to promote the stable continuous combustion of the fresh incoming fuel and air mixture. With the space constraints of the facility imposing a limit on the reaction residence time, the swirler offered the best solution to providing a compact recirculation region. Stable combustion was achieved through the use of a cast swirler with 45° vanes and holes dispersed around the outer circumference of the vanes. The design promoted mixing by impinging axial air flow through the holes with the swirling air flow.

Though the swirler aided in producing a stable reaction, a uniform plug flow was desired in order to avoid complications with data analysis and to provide a baseline case for future tests. An oxide-bonded silicon carbide

(OBSiC) ceramic foam matrix was used to dissipate the swirl imparted on the flow by the swirler. The ceramic is rated up to 1200°C and has been able to withstand thermal shock and stress loading due to periodic testing. The 7.62 cm diameter, 2.54 cm-thick matrix was positioned such that it was five duct diameters downstream of the quarl section and one duct diameter upstream of the quick-mix module. The porosity of the foam, rated at 4 pores per cm (10 pores per inch), was sufficient in allowing the required flow rate through the 2.54 cm thickness at a negligible 0.3% pressure drop in the system.

Profile measurements obtained across diameters of the rich zone showed that relatively uniform product concentrations and temperatures were achieved. The structural integrities of the ceramic foam and of the combustor refractory lining and parts were assessed after the apparatus was subjected to continuous testing lasting up to three hours per run. The apparatus has already undergone over 100 hours of total testing with no noticeable damage.

In summary, the challenge of producing a rich product generator was met with the construction of a system that was safe to operate, exhibited part durability over continuous testing and cyclic loading, and produced a stable reaction and uniform rich effluent to the quick-mixing region.

4.1.3 Jet Plenum Delivery

The plenum feeding the jet air to the quick-mixing module was fabricated from aluminum pipe 15.2 cm in inner diameter to give a 3.4 cm clearance between the plenum wall and quick-mix module. The air feeding the quick-mixing jets also served to cool the wall of the top two-thirds of the rich combustor length. Convective wall cooling is utilized in rich combustor wall cooling (Zarzalis, *et al.*, 1992) because conventional liner cooling schemes, which introduce film air into the rich reaction, encourage the formation of hot stoichiometric pockets.

Air for the quick-mixing jets was directed through flexible hoses to four air ports located near the bottom of the plenum. A high-temperature steel flow straightener 7.6 cm high with cell diameters of 0.95 cm was placed between the combustor and plenum walls to condition and promote an equal distribution of jet air entering the quick-mixing module. A pressure tap and a K-type chromel-alumel thermocouple monitored the pressure drop across the quick-mixing module and the temperature of the jet air, respectively. Optical access into the plenum was provided by two Pyrex windows situated 180° apart.

4.1.4 Quick-Mixing Modules

The modular quick-mixing section allowed for testing different jet orifice configurations by interchanging cylindrical quartz modules. The modules were held in place by a sealing mechanism which compressed the module against the combustor. Ceramic fiber paper consisting of a blend of alumina and silica that was rated up to 1260°C under continuous usage served as the gasket material between the quartz module and stainless steel surfaces.

The 80 mm inner diameter, 85 mm outer diameter modules were 280 mm long, with the orifices equally spaced along the circumference of the tubing (Figure 4.4). The six geometries tested were the 8-, 9-, 10-, 12-, 14-, and 18-round orifice configurations.

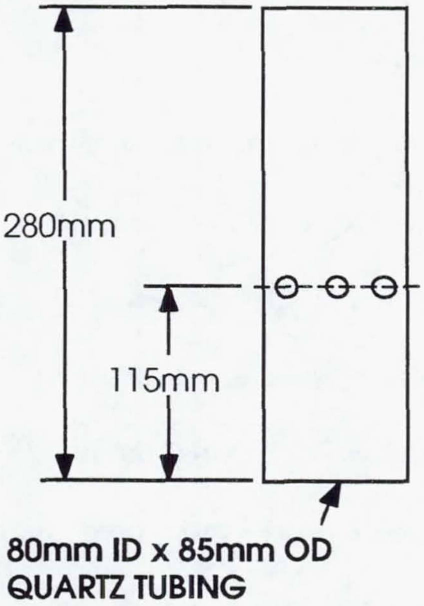

Figure 4.4 Quick-Mix Module Dimensions

The total area for each orifice configuration was 1237 mm^2 and was based on a design momentum-flux ratio of 40 and discharge coefficient of 0.65. The calculation of the jet orifice area appears in Appendix A.

4.2 Data Acquisition

Data were acquired with a stationary probe while the experimental apparatus was moved through the x-, y-, and z- traverses to the desired data point. A digital encoder (Mitutoyo) monitored the position of the probe tip with respect to the center of the quick-mix module. A sector of data was obtained at each of six planes situated throughout the length of the module. Measurements of temperature and species concentration were obtained.

4.2.1 Probe Design

A double-jacketed water-cooled stainless steel probe 30 cm in length was used to extract gas samples from the quick-mixing section (Figure 4.5). The

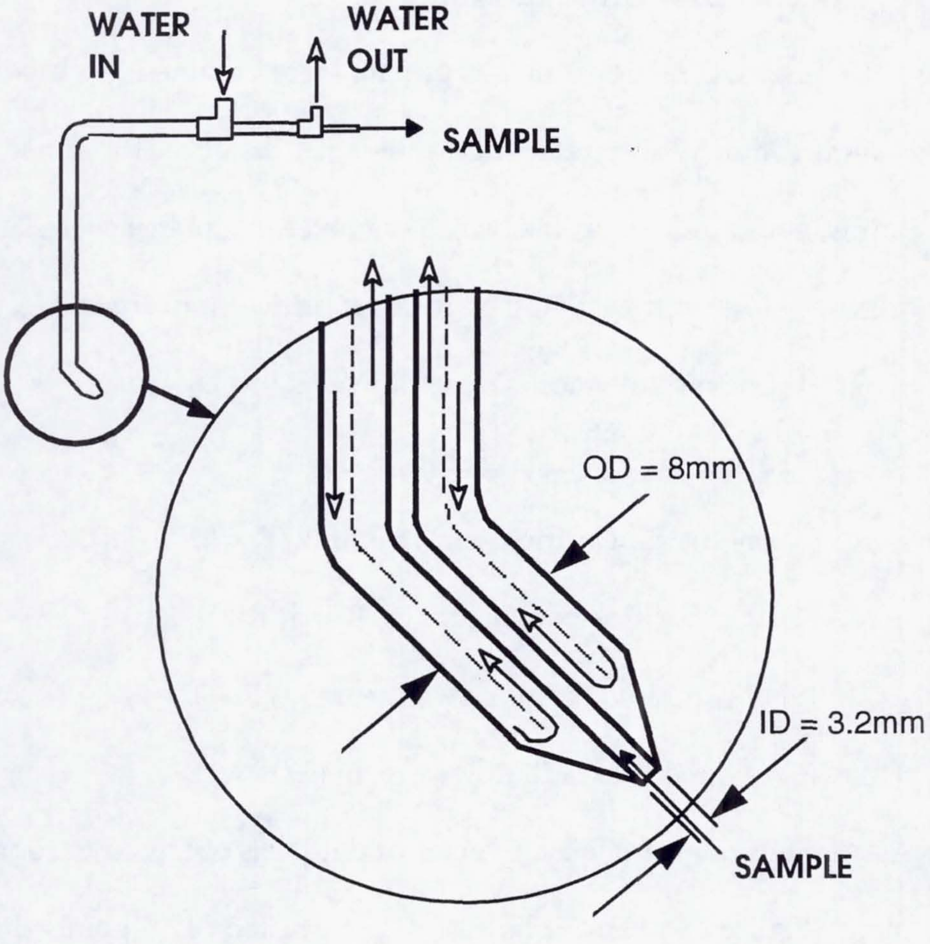

Figure 4.5 Probe Design

probe measured 8 mm in outer diameter and tapered down to a 3.2 mm tip. A 45-degree bend was made one inch from the tip. The probe design was influenced by the research of Sowa, *et al.* (1994), who found that a thermocouple probe with a 45-degree angled tip was the best design for acquiring temperature data that biased the mainstream and incoming jet flow equally in the orifice region. The plane of the angled probe tip was positioned such that the tip pointed toward the center of the sector wall.

4.2.2 Data Grid and Planes

Six cross-sectional planes of data were obtained per module as depicted in Figure 4.6. With z referring to the axial distance, R defined as the module radius, and d defined as the orifice diameter, the planes were situated, with the origin z = 0 set at the leading edge of the orifice, at positions

(1) one module radius upstream (z/R = -1),

(2) at the orifice leading edge (z/R = 0),

(3) one-half the orifice axial height (z/R = (d/2)/R),

(4) at the orifice axial height (z/R = d/R),

(5) one module radius downstream (z/R = 1),

(6) two module radii downstream (z/R = 2).

Assuming flow symmetry, a sector of data was obtained to represent the entire plane (Figure 4.7). Each plane of data consisted of 16 points distributed across

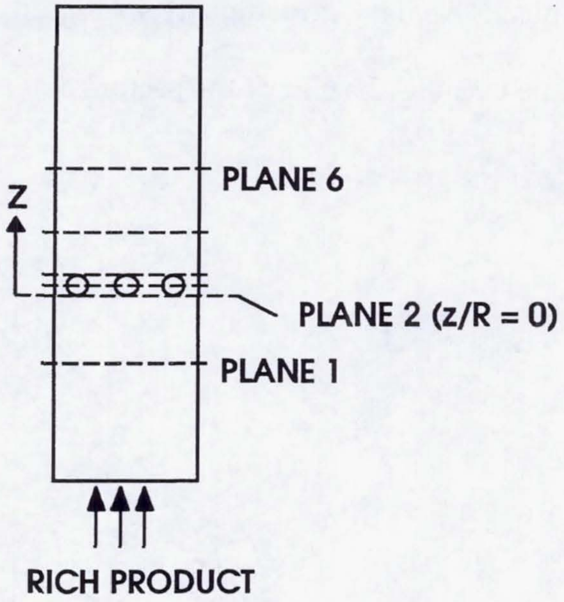

Figure 4.6 Measurement Planes

a sector that encompassed two orifices. One point was located at the center while the rest of the points were positioned along the arc lengths of three radii at 12.7 mm, 25.4 mm, and 38.1 mm. Five points were positioned along each arc length such that their positions formed radial-axial planes that bisected either the orifices or the wall region between the orifices. Of the resulting radial-axial planes, two were aligned with the orifices and three were aligned with the wall.

A 90° sector was used for the 8-hole module, an 80° sector for the 9-hole module, a 72° sector for the 10-hole module, a 60° sector for the 12-hole module, a 51.4° sector for the 14-hole module, and a 40° sector for the 18-hole module. The data grid density increased with the number of orifices in the module because the size of the sectors decreased.

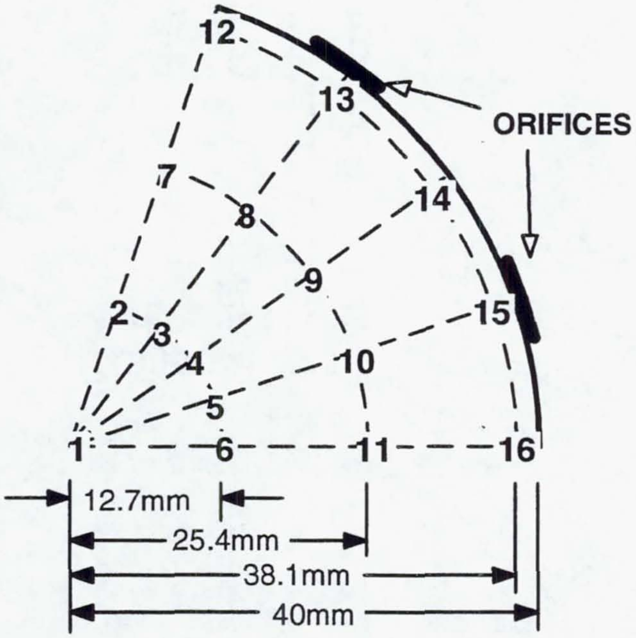

Figure 4.7 Data Grid Sector over Two Orifices

4.2.3 Temperature Measurements

A B-type platinum-rhodium thermocouple was constructed from a set of bare 30% versus 6% Rhodium wires 0.254 mm in diameter. The range of the B-type thermocouple, which falls between 0° and 1700°C, provided a suitable range for the reaction temperatures that were measured. The error associated with the thermocouple wire was 0.5°C for temperatures above 800°C.

Both wires, with one ensconced in a cloth sheath, were inserted into plastic tubing that was shrunk though heat-treatment. The thermocouple end that would be inserted into the reacting flow had its wires threaded separately through two channels of a 2.5 cm length of ceramic tubing. The ends of the wire exiting the ceramic were joined with a spot weld.

The thermocouple had a thickness that was less than 3 mm to facilitate its threading through the probe. The unjoined ends of the thermocouple exiting from the probe were connected to an analog-to-digital screw terminal panel attached to a personal computer. An ice water bath served as the reference point for the thermocouple. Figure 4.8 depicts a schematic of the temperature acquisition set-up.

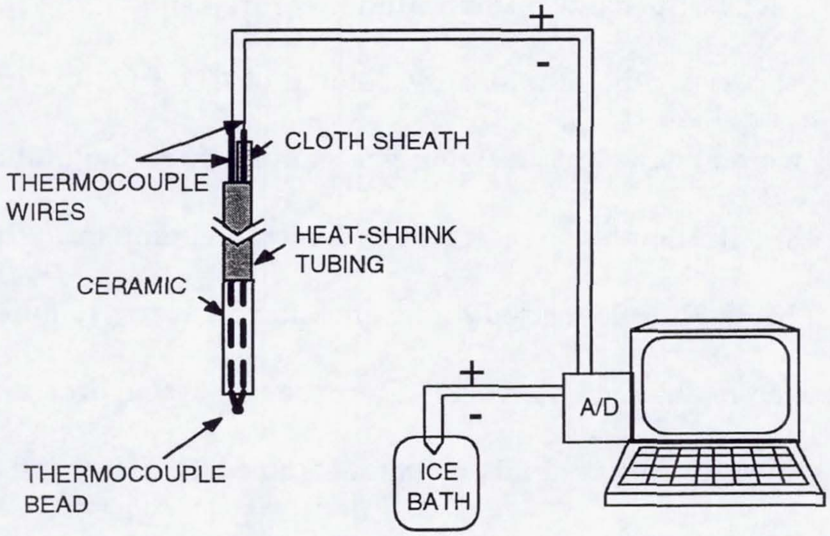

Figure 4.8 Temperature Data Acquisition Set-Up

A data acquisition program (Omega Engineering, Inc.) was modified to read the voltage signal from a B-type thermocouple. The program sampling rate was set at approximately 100 readings per 15 seconds. Voltage measurements were obtained at a point as soon as the readings stabilized after a period of approximately 45 seconds. The fluctuation in temperature measurement was highest in the jet orifice region, where fluctuations reached at most 100°C, or 10% of the mean measured value.

The readings acquired by the program were compared to readings obtained from a digital meter (Analogic AN2402) at several points in the rich section of the combustor. The difference between the readings was determined to be less than 5%.

4.2.4 Species Concentration Measurements

Species concentrations by volume of CO, CO_2, O_2, unburned HC, and NO_x were obtained by drawing gas samples from the points in the flowfield planes. The samples were drawn by a vacuum pump from the probe through a 15 m heated line connected to the emission analyzers (Figure 4.9). The heated line was maintained above 100°C to prevent water drop out in the line and subsequently the possibility of water-soluble NO_x dissolving in the condensate.

The analyzers (Horiba Instruments, Inc.) utilized non-dispersed infrared (NDIR), paramagnetic, flame ionization detection (FID), and chemiluminescence techniques to measure both CO_2 and CO, O_2, unburned HC, and NO_x, respectively. Appendix B describes further the principles behind the detection methods employed by the emission analyzers.

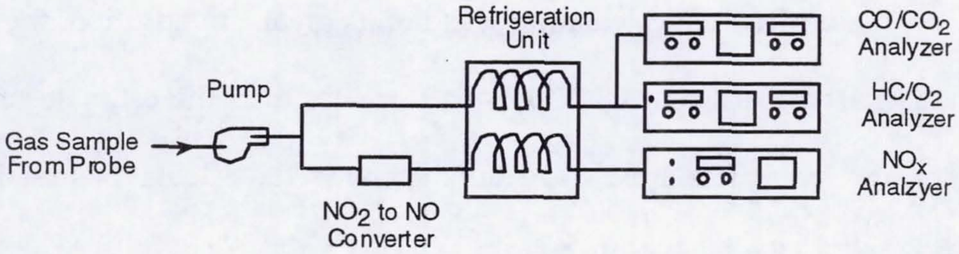

Figure 4.9 Emission Analyzer Routing (Courtesy of M. Miyasato)

Prior to testing, the analyzers were set to zero by flowing nitrogen gas (or air for the FID analyzer only) through the system. The analyzers were then calibrated with their respective span gases.

A measurement was obtained at a point after the readings on the console stabilized (approximately 45 seconds). Data were acquired with an acquisition program that read 100 samples in 20 seconds and returned an averaged quantity. The uncertainty in the analyzer species concentration measurement was 1% of the full scale reading.

4.3 Experimental Conditions

The operating conditions under which the tests were run are noted in Table 4.1. The actual momentum-flux ratio was higher than expected because the orifice area was based on a rich zone adiabatic flame temperature of 1800K (see Appendix A) while the measured temperature was 20% lower. The jet temperature had also been underestimated, but the effect of the jet temperature on the orifice area calculation was not as great. In addition, the actual orifice discharge coefficient C_d of 0.73 was greater than the estimate of 0.65 used to design the orifice area. Appendix C shows the calculations made in deriving the values listed in Table 4.1.

Table 4.1 Operating Conditions

Parameter	Value
P (kPa)	101
rich equivalence ratio ϕ	1.66
overall ϕ	0.45
T_{main} (K)	1500
T_{jet} (K)	480
V_{ref} (m/s)	18
momentum-flux ratio J	57
mass ratio MR	2.5
density ratio DR	3.3
velocity ratio VR	4.2
discharge coefficient C_d	0.73

CHAPTER 5

RESULTS AND DISCUSSION

5.1 Overview

Temperature and species concentration measurements were obtained for 8-, 9-, 10-, 12-, 14- and 18-hole configurations of equal orifice area at a set momentum-flux ratio of 57 and mass-flow ratio of 2.5. The results are presented in three different formats: (1) histograms to depict the distribution of the raw data, (2) contour plots of radial-axial sections to show the axial evolution of the flow, and (3) contour plots of sectors to show planar symmetry and the extent of mixing and reacting processes.

Table 5.1 summarizes the z/R values for each of the six planes measured per module. Planes 3 and 4 are situated at the orifice mid-height and height levels. Differing z/R values for each configuration occur because the orifice area is kept constant to keep the jet-to-mainstream momentum-flux ratio set.

Table 5.1 Normalized Axial Length z/R per Plane per Module

	z/R Values					
Plane	8 Holes	9 Holes	10 Holes	12 Holes	14 Holes	18 Holes
1	-1	-1	-1	-1	-1	-1
2	0	0	0	0	0	0
3	0.175	0.165	0.157	0.143	0.133	0.117
4	0.350	0.331	0.314	0.286	0.265	0.234
5	1	1	1	1	1	1
6	2	2	2	2	2	2

5.2 Reacting Flow Field Description: 8-Hole Module

The description of the reacting flow field of the 8-hole case is discussed first to gain a sense of jet mixing and reaction in a rich reacting crossflow.

5.2.1 Temperature Profiles

Figure 5.1 depicts histograms of temperature measurements obtained for the 8-hole configuration. The histograms provide information on the temperature distribution per plane at 16 grid points (recall Figure 4.7). Point 1 lies in the center of the module, Points 2-6 lie along the arc length at one-third of the module radius (hereafter denoted as R_1), Points 7-11 lie at two-thirds of the module radius (denoted as R_2), and Points 12-16 lie near the module radius R. Points 3, 5, 8, 10, 13, and 15 are aligned with the orifices.

Plane 1 ($z/R= -1$), which is representative of the rich product entering the quick-mixing module, shows a relatively uniform temperature distribution. Temperatures near 1500K were measured at points at the center and on the R_1 and R_2 arcs. Slightly lower temperatures ranging from 1300 to 1450K were obtained at the wall. The lower temperatures are attributed to the convective cooling of the outer module wall by the plenum air.

At the orifice leading edge (Plane 2, $z/R=0$), the temperatures still hover near 1500K with the exception of deviations at Points 13 and 15. The lower temperatures occur since the points are in the near field of the jet entrance.

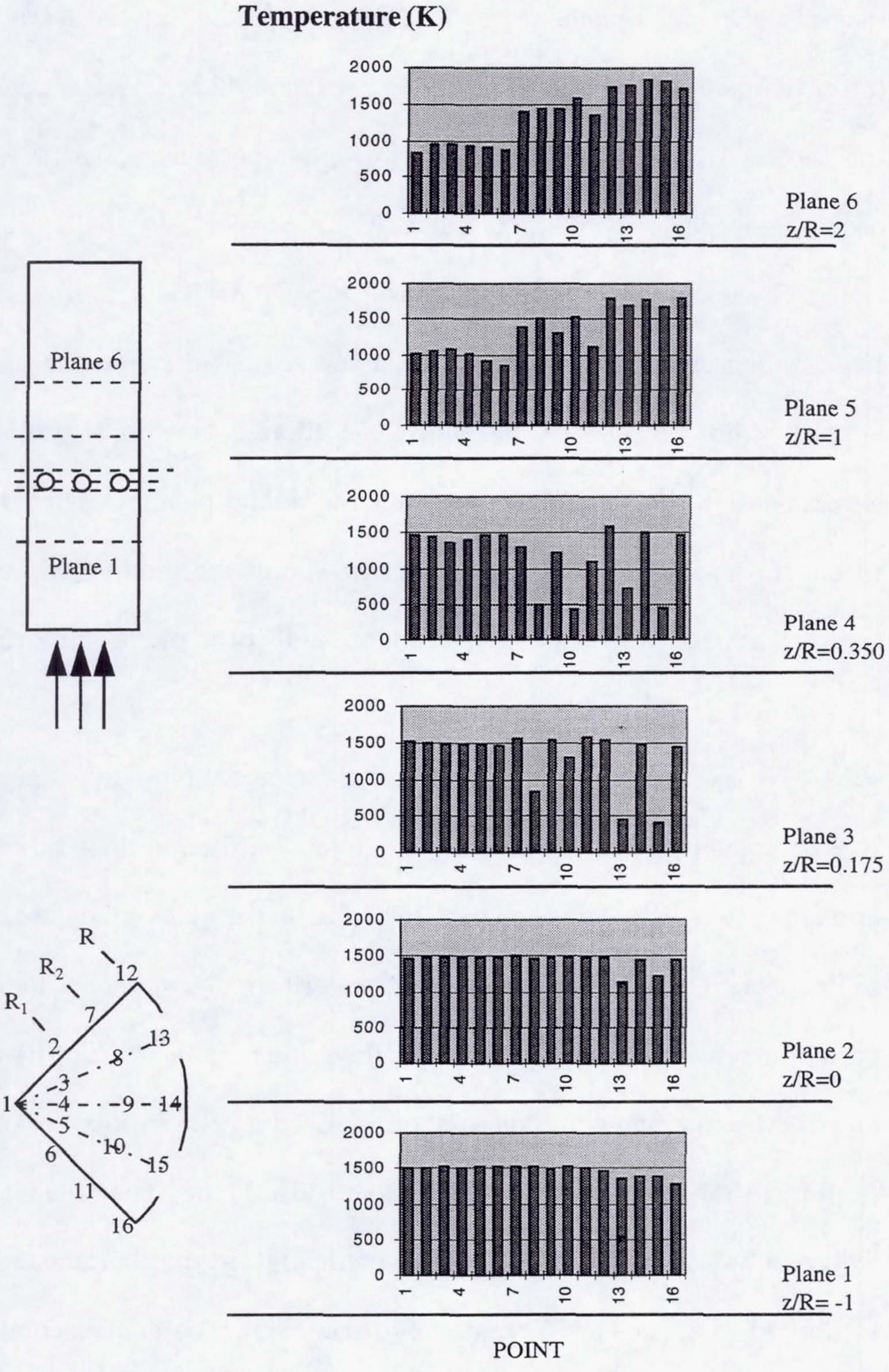

Figure 5.1 Temperature Distribution for the 8-Hole Module

By the orifice half-plane (Plane 3, z/R=0.175), the temperatures at a majority of points remain at 1500K. However, jet entrance is clearly seen with lower temperatures near 400K occurring at Points 13 and 15. Jet penetration to the second radius R_2 is marked by lower temperatures of 810K and 1300K occurring respectively at Points 8 and 10.

The unequal temperatures measured at Points 8 and 10 should not occur if jet and crossflow symmetries are assumed. The symmetry assumptions appear valid because of the flow conditioning methods utilized in the experiment: a flow straightener installed in a long plenum chamber was used to ensure an equal distribution of jet flow into the module while a porous ceramic matrix was used to condition and promote a uniform reacting crossflow.

To investigate the cause of the asymmetry, pitot tube measurements were obtained under non-reacting conditions at the entrance of both orifices and along two diameters across the inlet duct to the quick-mixing section (at the z/R= -1 plane). The measurements at the orifices showed a 3% to 5% velocity variation which suggests that the jet flow entering the two orifices is nearly equal. Measurements of the crossflow showed a near-uniform velocity profile (within a 15% range). Because Points 8 and 10 at Plane 3 lie in the vicinity of the jet-crossflow interface, the unequal temperature measurements could be attributed to a fluctuation created by fluid interaction and reaction processes. Time-resolved measurements are needed to verify this hypothesis.

At the orifice trailing edge (Plane 4, z/R=0.350), all of the jet fluid has entered the module. The jets penetrate to the second-third mixer radius R_2 but have not yet fully dispersed and mixed with the neighboring node points. Note that the central core temperatures are still maintained near 1500K.

Substantial reaction and mixing occurring between the plane at the orifice trailing edge (Plane 4) and the plane one duct radius downstream of the orifice leading edge (Plane 5, z/R=1) is suggested by major differences between the two histogram profiles. At Plane 5, mixing and reacting processes have produced the following evenly distributed, stratified bands of temperature: a 1000K band at the center and first mixer radius R_1, a 1400K band at the second mixer radius R_2, and a 1750K band near the module radius R. The 1750K temperatures in the outer band R are higher than the initial rich effluent temperature of 1500K, which suggests the occurrence of chemical reaction in that region.

Jet fluid penetration to the central core is inferred by the temperatures observed in the central core which are overall lower than the 1500K temperature of the entering rich effluent. The 1000K temperature band at the center and at R_1 are higher than the initial 400K temperature of the jet fluid, which suggests the occurrence of either reaction, mixing, or both processes. However, the extent to which the higher temperatures are attributed to reaction rather than to mixing cannot be determined without measuring conserved scalar quantities to derive the mixture fraction field.

The histogram profile obtained two duct radii downstream of the orifice leading edge (Plane 6, z/R=2) is nearly identical to that obtained at Plane 5. The similar profiles, which show a lack of extensive mixing and reacting activity between the two planes, indicate that the bulk of the reaction and mixing profiles appears to have been completed within one duct radius of the jet entrance.

The contour plots in Figures 5.2a and 5.2b offer a spatial view of the temperature distributions. The radial-axial and sector cross-sectional plots respectively depict the longitudinal and planar evolution of the flow field.

The radial-axial plots (e.g. in Figure 5.2a) depict two cross-sections: one which is aligned with the wall midpoint between the orifices (a "midplane" cross-section) and one which is aligned with the orifice (a "centerplane" cross-section). The midplane cross-section is an average of the three lines of data aligned with the wall while the centerplane cross-section is an average of the two lines of data aligned with the hole. The data are plotted on axial versus radial length scales z and r normalized with respect to the mixer radius R. Sector plots such as those seen in Figure 5.2b are an unaveraged depiction of the interpolated 16 points of data obtained per sector.

A nearly uniform temperature distribution in the rich flow, with the exception of the small band of lower temperatures occurring at the wall, enters the quick-mixing regime. Jet introduction into the flow is seen at the orifice mid-plane (Plane 3, z/R=0.175), with the full introduction of jets occurring by

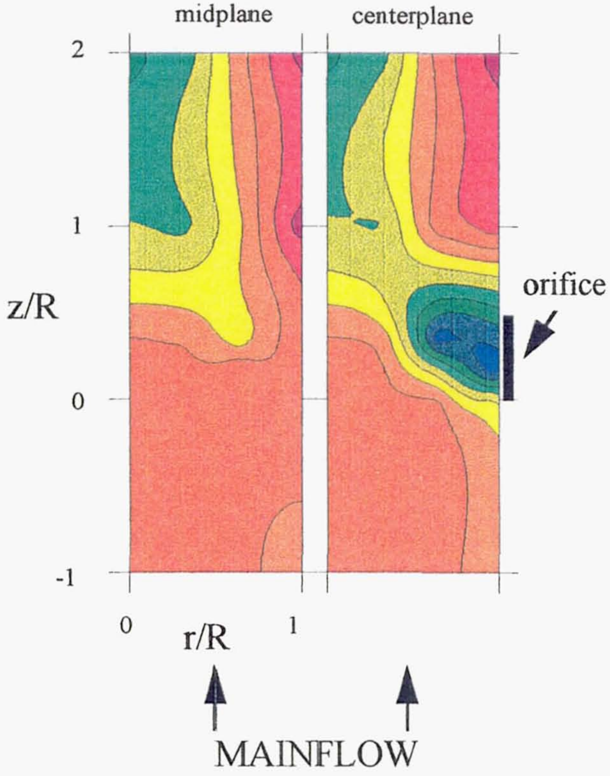

Figure 5.2a Averaged Axial Temperature Profiles for the 8-Hole Module

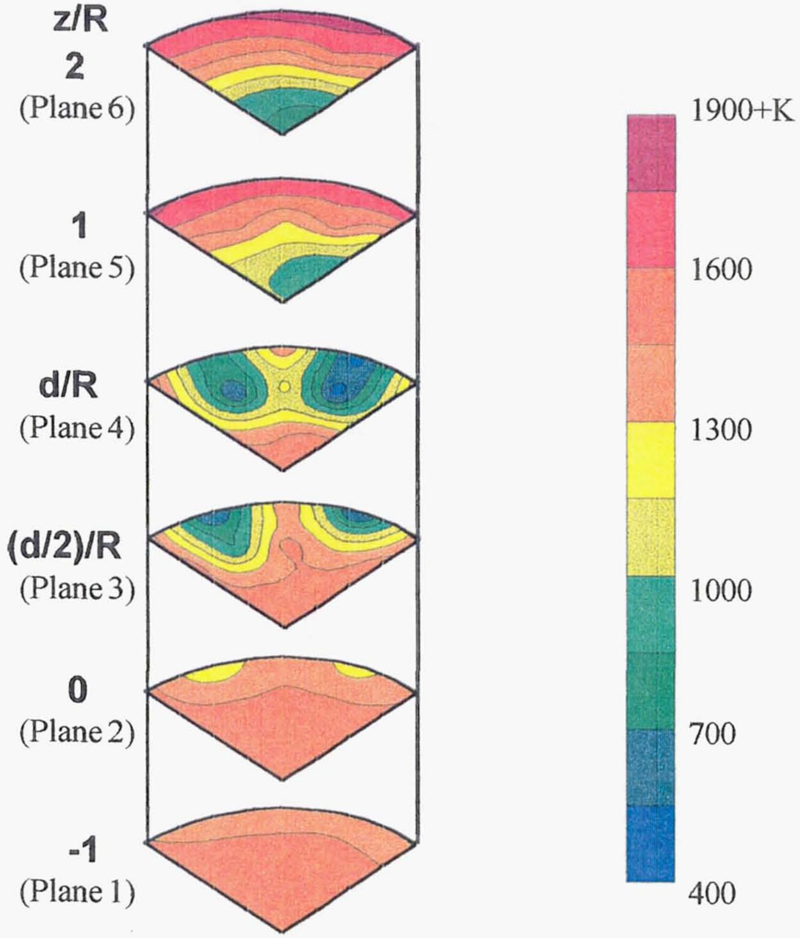

Figure 5.2b Temperature Sector Profiles for the 8-Hole Module

the orifice trailing edge (Plane 4, z/R=0.350). The longitudinal centerplane plot (Figure 5.2a) depicts jet penetration toward the centerline within one duct radius (Plane 5, z/R=1). The midplane cross-section shows relative symmetry with the centerplane cross-section in the flow downstream of the z/R=1 plane.

Directly downstream of the orifices, temperatures are lower than the initial mainflow temperature as the cooler jet fluid entrains and mixes with the hot crossflow fluid. At one duct radius downstream (z/R=1) the jets penetrate toward the center and displace the rich crossflow to the wall. The displaced fluid undergoes an increase in temperature as some of the jet fluid mixes with the crossflow to initiate the CO oxidation reaction. As a result, a band of temperatures higher than the initial rich effluent is formed.

The sector cross-sections in Figure 5.2b show the occurrence of temperature stratification beginning at Plane 5. At two duct radial lengths (Plane 6, z/R=2) the stratification becomes more distinct but does not change drastically in distribution.

5.2.2 Species Concentration Profiles

Figures 5.3a and b show the histogram distributions of O_2, CO_2, CO, HC, and NO_x concentrations measured for the 8-hole module. The concentrations are measured in terms of either % or parts per million (ppm) by volume. The distributions at Plane 1 reveal uniform rich zone concentrations of 0% O_2, 5.2% CO_2, 12% CO, and 1.5 ppm NO_x. The HC concentrations, while overall

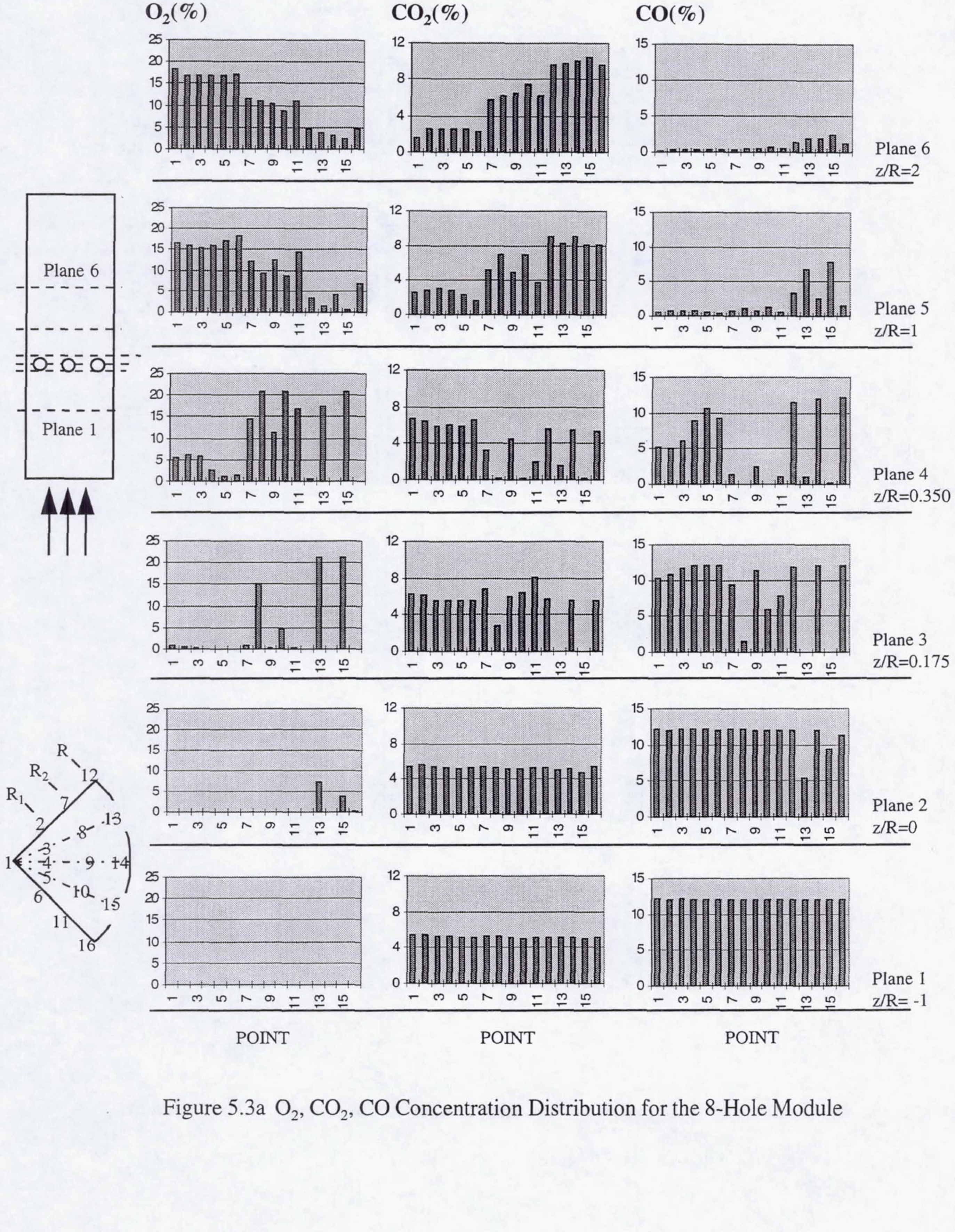

Figure 5.3a O$_2$, CO$_2$, CO Concentration Distribution for the 8-Hole Module

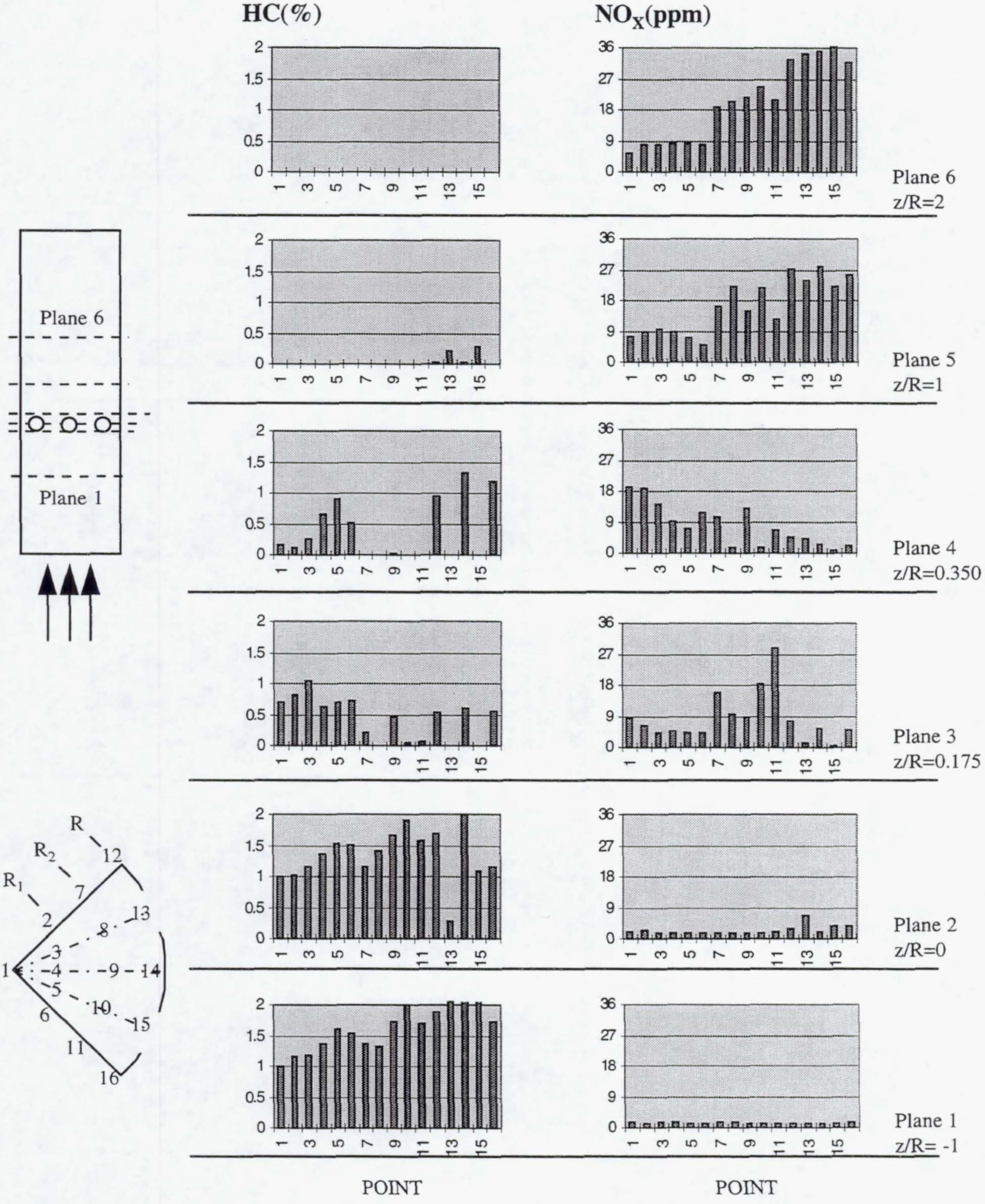

Figure 5.3b HC and NO_X Concentration Distribution for the 8-Hole Module

relatively uniform, show more variability. 1% to 1.6% concentrations occur in the central core while higher concentrations up to 2% are present in the wall region. HC species are comprised of products of incomplete combustion (PICs) that have not oxidized because of either a lack of oxidant or temperature to propagate the reaction. The latter explanation applies in this case, where the lower wall temperatures seen in Figures 5.1, 5.2a, and 5.2b promote the higher HC levels near the wall region.

Mass balances of carbon, hydrogen, oxygen, and nitrogen were performed on the rich products measured at Plane 1 to determine the integrity of the measurements. The reaction of propane (C_3H_8) and air was assumed to yield products of CO, CO_2, unburned C_3H_8, O_2, NO, N_2, and H_2O. The fuel and air flow rates are known; CO, CO_2, unburned C_3H_8, O_2, and NO are measured; and N_2 is assumed to make up the rest of the exhaust gas volume. The only unknown quantity in the reaction is the mole fraction of H_2O, which has been dropped out from the sample by a condenser before the sample enters the emission analyzers. As a result, the mole fraction of water is calculated from a separate mass balance performed on each element and is compared for equivalency.

The resulting analysis (see Appendix D) shows the water mole fraction for all elements except carbon to be within the same range. However, a comparison between the measured species concentrations obtained in the rich product region with output from the NASA chemical equilibrium code shows similar results: under room temperature and atmospheric pressure the NASA equilibrium code predicts that the combustion of propane at an equivalence ratio of 1.7 yields 0% O_2, 4.1% CO_2, 12.3% CO, and 1.3 ppm NO_x. Another major constituent that the equilibrium code predicts but that was not measured in the experiment is H_2, for which a 9.4% concentration was predicted. The neglection of H_2 in the mass balance equation may have greatly affected the closure of the equation.

Inferences related to jet penetration and mixing can be formed from the axial distribution of species concentrations. The O_2 charts in Figure 5.3a, for example, show the evolution of jet penetration from the leading edge of the orifices (Plane 2). Farther downstream at the orifice mid-height plane (Plane 3), the jets fill the outer mixer radius R to near-21% concentrations at Points 13 and 15, which are aligned with the orifices. The jet fluid then migrates toward the second radial band R_2 (Plane 4), as seen by 21% O_2 concentrations at Points 8 and 10, and begins to disperse, as noted by the appearance of oxygen at neighboring points 7, 9, and 11. At one and two mixer radii downstream of the orifice leading edge (Planes 5 and 6) the jet fluid penetrates to the central core.

At the orifice leading edge and mid-orifice planes (Planes 2 and 3) the points at which O_2 levels are measured (Points 13 and 15 in Plane 2, Points 8, 10, 13, and 15 in Plane 3) correspond to the decrease or increase in the other species concentrations measured at the same points. The decrease in CO_2 levels at Points 13 and 15, and at Points 8 and 10 at Plane 3 is attributed to jet dilution (see Figure 5.3a). The slight increase of CO_2 concentrations at other points in the plane reflect reaction. Similarly, the dilution of CO (Figure 5.3a) and HC (Figure 5.3b) at Points 13 and 15 correlates to the presence of O_2 concentrations at the same points in Plane 2.

The occurrence of reactions that consume CO and HC is corroborated by a comparison between the overall concentrations measured at Planes 2, 3, and 4. Plane 3 shows a decimation of HC concentrations that had been present in abundance in Plane 2. The CO concentrations are also decreased, though not as rapidly as HC, because of the slower CO reaction. Between Planes 3 and 4, additional CO has reacted while no further reaction of HC occurs.

The presence of reaction in Planes 2 and 3 is verified by the NO_x histograms (Figure 5.3b). At Plane 2, Points 13 and 15 show slightly higher NO_x concentrations, a sign that reaction processes occurring at the jet-crossflow interface are increasing temperatures to levels that promote the formation of NO_x from the nitrogen in the air. The reaction continues in Plane 3 where points at the second radius R_2 register higher levels of NO_x. Between Planes 3 and 4, however, jet displacement processes dominate as the body of jet fluid is introduced into the crossflow. No further evidence of substantial NO_x production is seen; the NO_x produced in the second radial region migrates to the first radius R_1 and the centerline.

At planes within the vicinity of the orifices (Planes 3 and 4), all of the measured species show asymmetric concentrations in the second radial band R_2

where the points aligned with the orifices (Points 8 and 10) and the points aligned with the wall (Points 7, 9, and 11) should show equal concentrations within each group. The asymmetric species concentrations measured in the second radial band may be attributed to fluctuations caused by reacting and mixing processes occurring at the jet-crossflow interface, as explained for the unequal temperature distribution similarly noted in section 5.2.1.

The bulk of the reaction takes place in the zone downstream of the holes (between Planes 4-5) where the jets penetrate toward the center and begin to disperse throughout the crossflow. In this region of reaction between Planes 4 and Plane 5, CO_2 and NO_x concentrations rise, particularly in the wall region, while CO and HC concentrations decrease significantly. Most of the reaction terminates by the z/R=1 plane (Plane 5) since the magnitude of the profiles measured at that plane and at z/R=2 (Plane 6) do not change substantially.

The contour plots in Figures 5.4a and 5.4b give an alternative presentation of the species concentration profiles. The radial-axial profiles (Figure 5.4a) illustrate the evolution of jet penetration and flow field characteristics in the module while the sector plots (Figure 5.4b) offer another view which indicate species distribution symmetry.

From Figures 5.4a and 5.4b, the species entering the module are generally uniform up to the plane of jet entry. Evidence of early jet penetration is apparent at the orifice leading edge (z/R=0). Full jet penetration is apparent for all species by the orifice trailing edge (z/R=0.350).

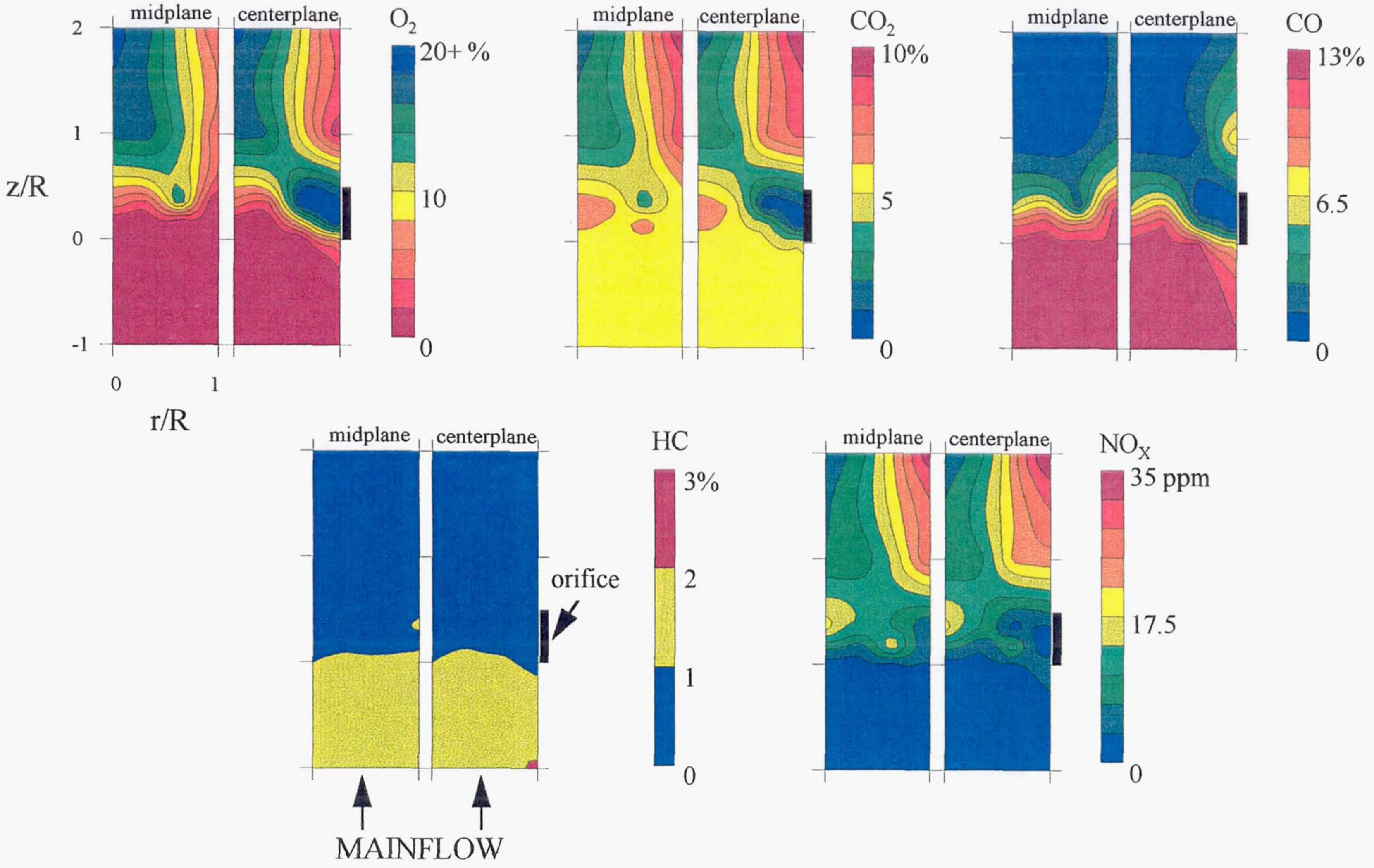

Figure 5.4a Axial History of Species Concentrations for the 8-Hole Module

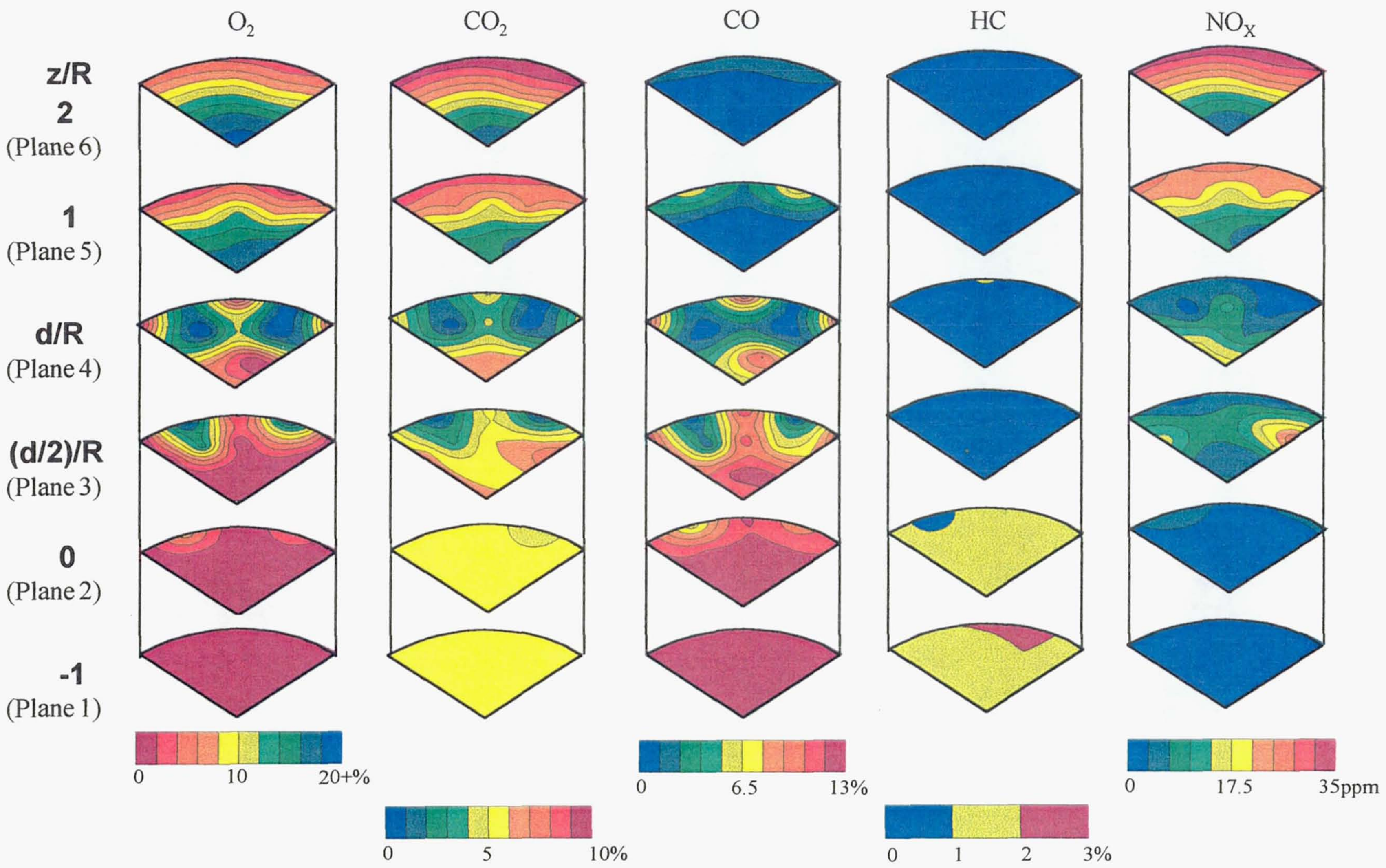

Figure 5.4b Sector Profiles of Species Concentrations for the 8-Hole Module

Jet penetration as seen in the O_2 profiles is represented by a high concentration of jet fluid in the orifice region that enters the crossflow nearly intact before dispersing throughout the mixer radius (see Figure 5.4a). The jet appears to penetrate toward the center within one mixer radius length (i.e., at Plane 5, z/R=1).

The centerplane profiles show a transition region in the jet wake formed by the initial reaction between the jets and the entrained rich crossflow. Downstream of the z/R=1 plane the penetrating jets displace the rich reacting fluid toward the wall, as evidenced by the pocket of high CO concentration at the wall. The small pocket of CO subsequently disappears as CO reacts with the jet to form CO_2. This source of CO_2 increases concentrations at the wall from the z/R=1 to z/R=2 plane. The higher NO_x values also occurring at the wall downstream of the z/R=1 plane correspond to the higher temperatures (recall Figure 5.2a) that are associated with the CO oxidation reaction.

In addition to showing the extent of reaction and of mixing occurring between the jets and the rich mainstream, the sector plots in Figure 5.4b give an indication of jet and flow field symmetry. Although at the orifice midplane (z/R=0.175) the first jet appears to dominate over the second jet, by the orifice trailing edge (z/R=0.350) the jet flows are essentially symmetrical. At the z/R=1 plane, the flow field of stratified concentration bands is radically different from the previous plane which shows discrete jets. At the z/R=2 plane the stratified bands become more well formed but the overall flow field does not change drastically. This observation as well as the virtual disappearance of CO and HC between the z/R=1 and z/R=2 planes show that the jets have almost entirely reacted with the rich crossflow within one duct radius of jet entry for the 8-hole configuration.

5.3 Comparison of 8-, 9-, 10-, 12-, 14-, and 18-Hole Modules

The mixing and reaction performance of the six orifice configurations is assessed with a comparison of radial-axial and sector contour plots for each module. The objective of comparing the six mixing modules is to determine a configuration that leads to optimal jet trajectory penetration and hence optimal mixing and reaction within one duct radius of the jet entrance (i.e., at z/R=1). In combustor design, the attainment of a short combustor length is desirable to maintain the compactness of the engine. For the RQL configuration it is thus preferable to attain complete mixing in a minimal length. The one duct radius limitation has been used as an arbitrary reference plane of comparison by Hatch, *et al.* (1996), Kroll, *et al.* (1996), and Sowa, *et al.* (1994).

For the module performance comparison, only the contour plots are presented here. Stacked histogram plots of the temperature and species concentration profiles for the other module configurations (9-, 10-, 12-, 14-, 18-hole) may be found in Appendix E.

5.3.1 Temperature Profiles

Figure 5.5 shows the axial evolution of temperature profiles at the center- and midplane sections of all the cases tested. All six cases show rich inlet product temperatures of 1500K as well as cooler wall temperatures between z/R= -1 and z/R=0. The modules share other similar flow features such as a 400K temperature occurring where the jet enters the orifices and a band of hot fluid at the wall downstream of z/R=1.

The jet trajectory, defined by the approximate locus of points showing minimal temperature with respect to distance, is represented on the centerplane plots by a red line extending from the orifice mid-height to the z/R=1 plane. Beyond the z/R=1 plane, the disintegrating jet structure makes the determination of the trajectory difficult.

As the number of holes is increased, the jet penetration as indicated by the trajectory decreases and the jet flow disperses into the crossflow rather than accumulates in the central core. If the path of the trajectory is extended past the z/R=1 plane, the 8- through 12-hole modules produce jet impingement at the centerline and varying degrees of jet overpenetration. Jet trajectory inclination toward the center causes more fluid to concentrate in the center of the mixer at the z/R=2 plane, which is seen in the 8- to 12-hole cases by the cooler fluid temperatures there. The 14-hole case shows the attainment of a near-uniform temperature distribution between 1300 and 1600K (orange bands) by the z/R=2 plane whereas the 18-hole produces a hot core throughout the length of the

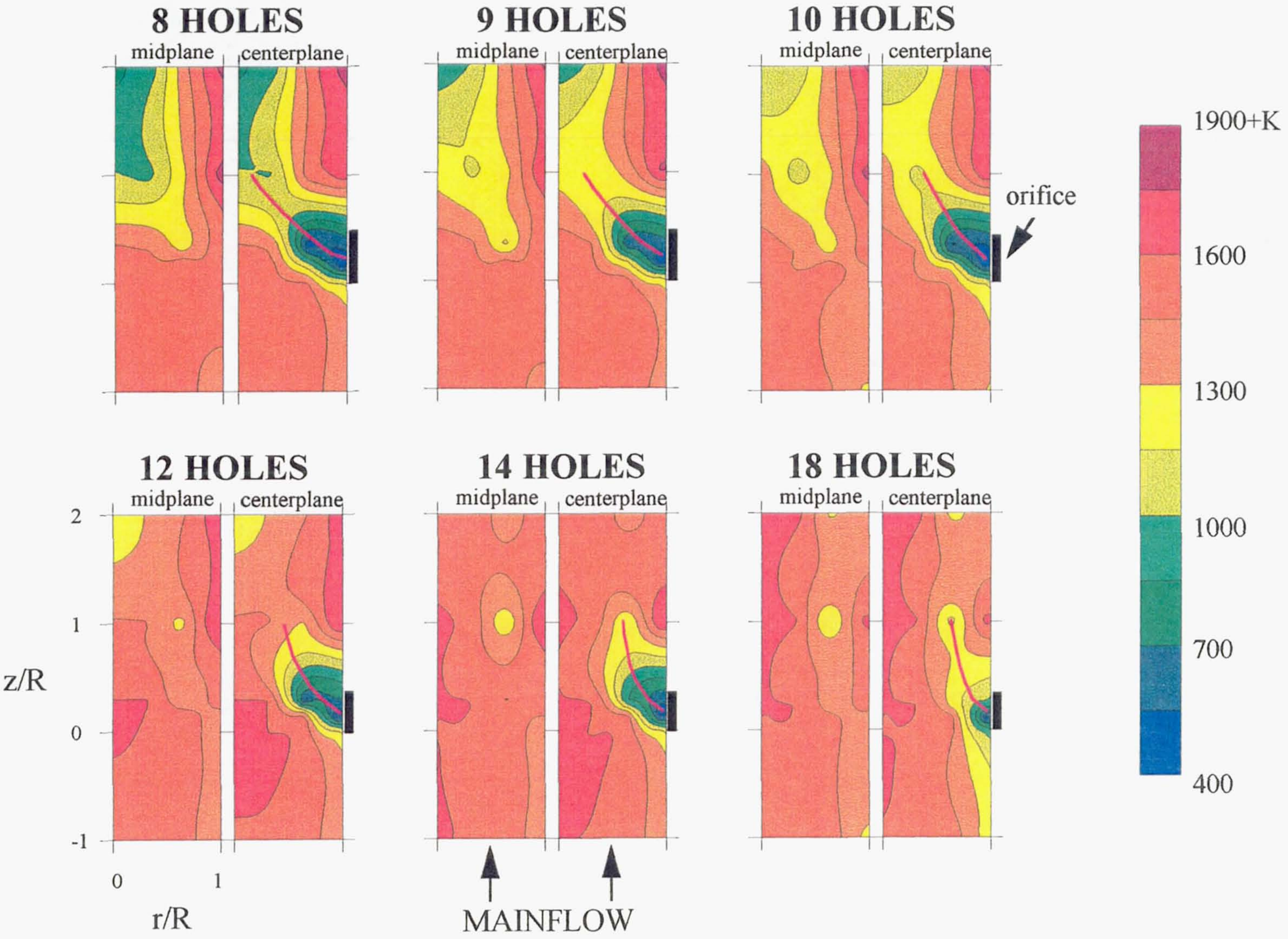

Figure 5.5 Axial History of Temperature at Two Radial-Axial Cross Sections

module which suggests jet underpenetration. Hence, the uniform temperature distribution produced by the 14-hole case shows that the configuration is optimal for this experiment. In this case, the jet trajectory reaches the half-radius of the mixer by the z/R=1 plane.

The sector profiles in Figure 5.6 show a stratification of fluid temperatures occurring by the z/R=1 plane which becomes more concentrically formed by the z/R=2 plane. In each case, there is an increase in temperature occurring between the z/R=1 and 2 planes, which suggests the occurrence of further reaction beyond one duct radius of jet entry. The increase is not as apparent in the 8-, 9-, and 10-hole cases as it is in the 12-, 14-, and 18-hole cases, which indicates more reaction occurring in the latter three configurations.

In the 8-hole case, the presence of fluid between 800K and 900K occurs in the center of the z/R=2 plane whereas the center temperatures at this plane for the 9-, 10-, and 12-hole modules are between 900K and 1100K. The 18-hole case shows a reverse trend where the center of the z/R=2 plane possesses hotter temperatures ranging between 1600 and 1750K and the outer annular region contains cooler fluid temperatures between 1150 and 1450K. The 14-hole case exhibits the most evenly dispersed bands of temperatures at the z/R=2 plane.

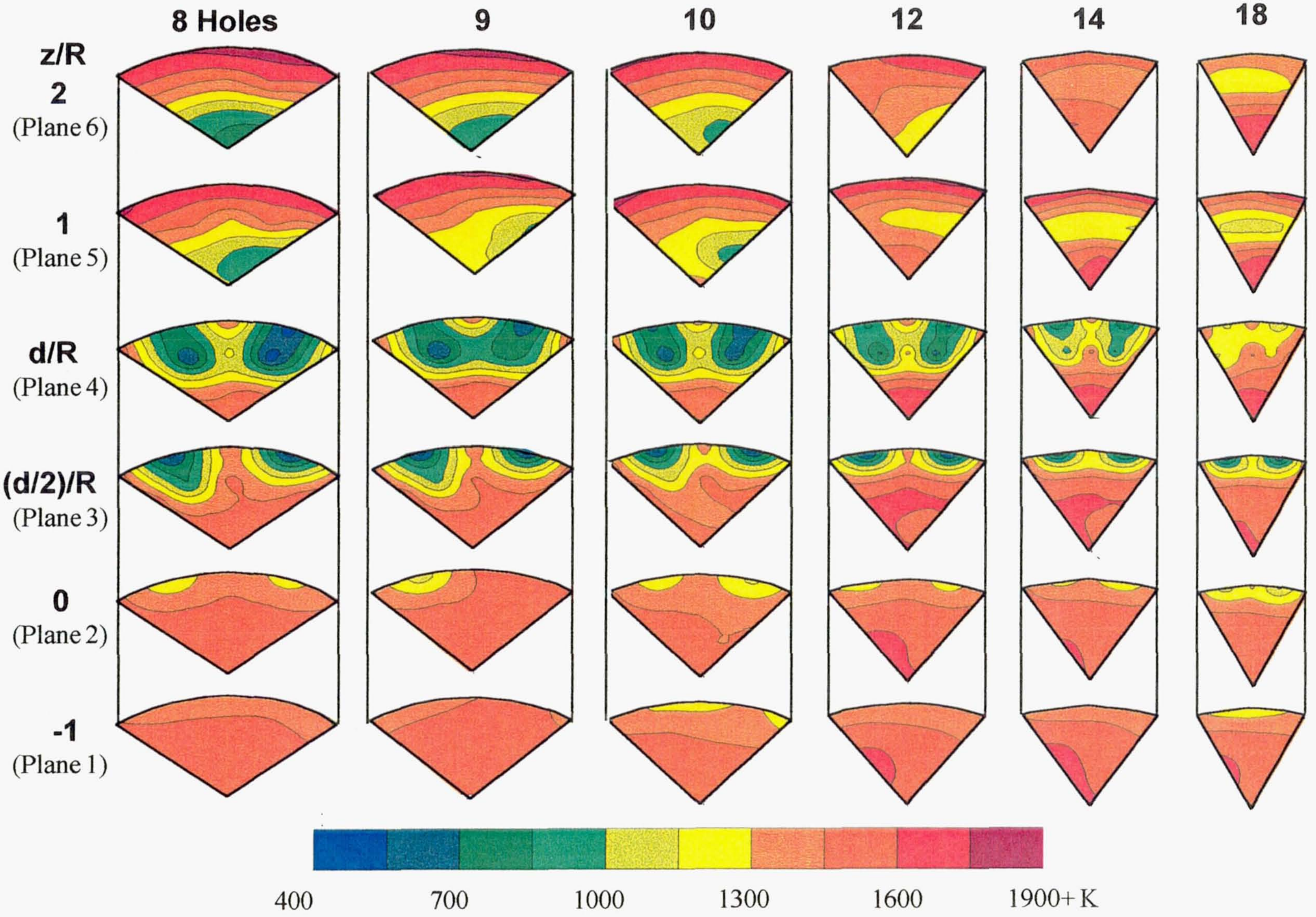

Figure 5.6 Sector Comparison of Temperature Profiles

5.3.2 Species Concentration Profiles

The effect of the number of holes on jet trajectory penetration is better illustrated in the radial-axial O_2 distributions of Figure 5.7. In the centerplane plots of all cases, discontinuities in color bands (yellow to blue bands) emanating from the jet orifice to the z/R=2 plane occur. The re-emergence of bands of high species concentration suggests the implausible production of additional O_2 in the reacting system. The lack of data measured between the orifice trailing edge and the z/R=1 planes, and between the z/R=1 and z/R=2 planes probably accounts for the discontinuous bands of O_2 concentration produced by interpolation.

The jet trajectory, defined as the locus of points showing maximal O_2 concentration as a function of distance, is drawn on the centerplane plots from the orifice midplane to the z/R=1 plane. The trajectories based on O_2 concentration nearly coincide with those based on temperature (see Figure 5.5).

High penetration of the jet trajectory causing fluid impingement at the centerline occurs in the 8-hole case and results in a large concentration of O_2 in the central core. This condition suggests that the 8-hole module is an overpenetrating case which is undesirable because the oxygen tends to accumulate in the center rather than disperse, mix, and react with the crossflow. Overpenetration also leads to less reaction since the accumulation of jet fluid in the center decreases the area of the jet-crossflow interface, or the promotion of reactant interaction. The 9-, 10-, and 12-hole cases also exhibit some degree of

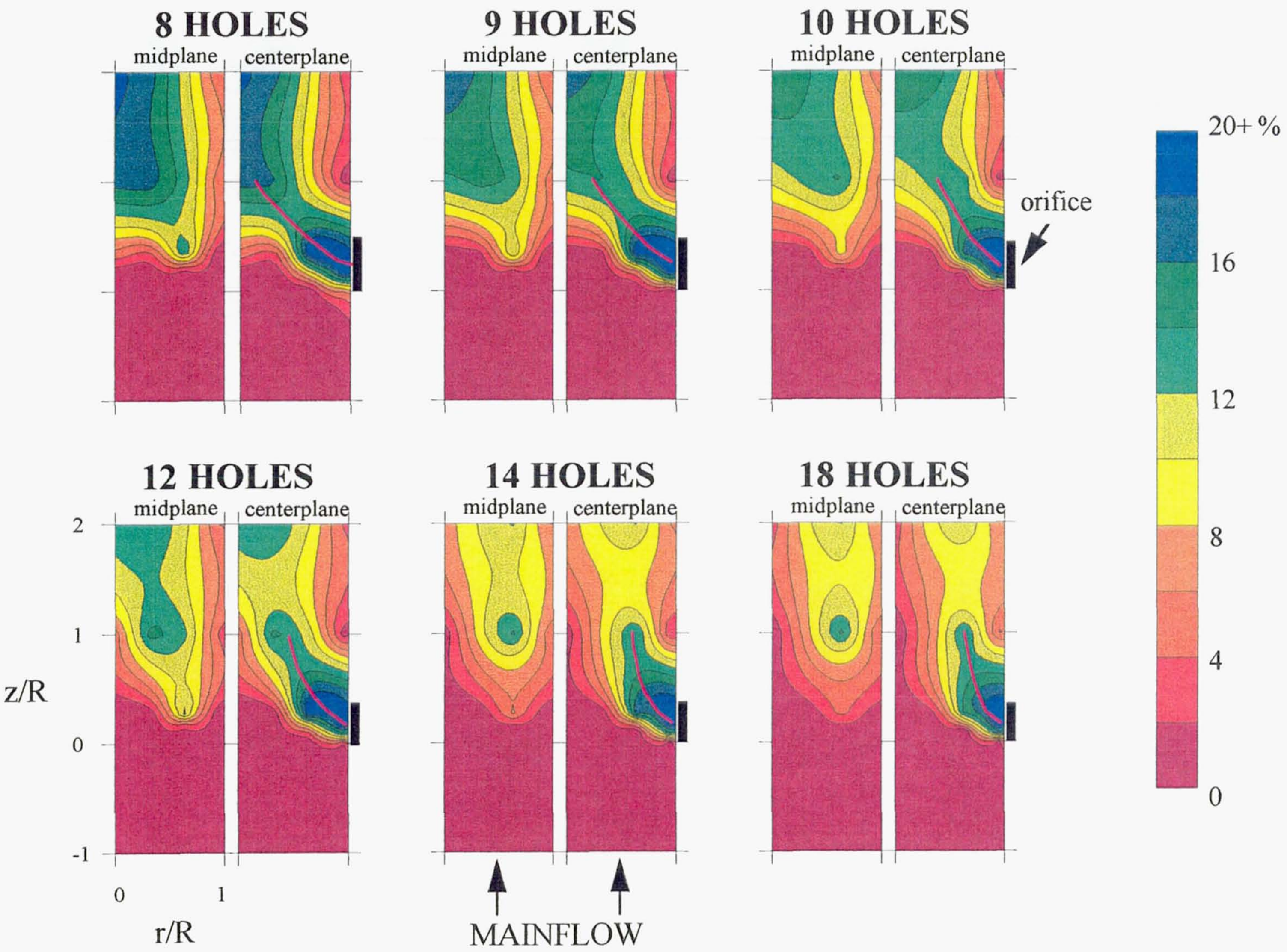

Figure 5.7 Axial History of O_2 Concentrations at Two Radial-Axial Cross Sections

overpenetration as the jet trajectory appears to intersect with the centerline by the z/R=2 plane.

The 14- and 18-hole cases produce a jet trajectory that does not penetrate to the center by the z/R=2 plane. Without jet impingement, a more lateral spreading of jet fluid, as evidenced by the narrower distribution of oxygen concentration values across the mixer radius, is achieved. The midplane O_2 profiles show that the 14- and 18-hole modules exhibit a smaller band of fluid devoid of O_2 at the wall (indicated in dark red and orange) between the z/R=1 and z/R=2 planes. The 18-hole case in fact shows no red bands between 0-4% in the jet wake, unlike the 14-hole case. However, the jet underpenetration property of the 18-hole case manifests itself with the occurrence of lower O_2 concentration bands in the core region. Like jet overpenetration, jet underpenetration decreases the maximal jet-mainflow surface area of reaction because a portion of the jet fluid is bounded by the wall of the module. Jet underpenetration allows the rich reaction products to exit the module without completing the combustion process, which is undesirable. In the 14-hole case, a larger jet surface area exposed to the crossflow accelerates jet dispersion and reaction such that more of the rich mainstream flow reacts with rather than bypasses the jets.

For cylindrical crossflow geometries, several investigations have determined a jet penetration depth that leads to better mixing. In a numerical study performed by Talpallikar, *et al.* (1992), results suggest that optimal mixing occurs when the jet penetrates to the mid-radius. Kroll, *et al.* (1993) infers from experimental results that optimal mixing occurs when the jet penetrates to the radius that divides the mixer into an equal core and annular area, or at a radial distance 30% from the wall. For the cases tested in this experiment, the jet trajectory as determined by both oxygen and temperature measurements intersects the z/R=1 plane beyond the radial midpoint from the wall for the 8-, 9-, and 10-hole cases; appears to approach the mid-radius for the 12- and 14-hole cases; and lies at a point before the mid-radius and toward the wall for the 18-hole case. The Talpallikar, *et al.* criteria support either the 12- or 14-hole case as producing the jet penetration that promotes the best mixing out of the configurations tested while Kroll, *et al.* (1993) data supports the 14- or 18-hole case as being the optimal configuration.

The number of holes leading to optimal jet penetration can be predicted by an empirical relation developed for non-reacting jets injected into a subsonic cylindrical crossflow. The relation from Holdeman (1993) states that the appropriate number of holes n that will lead to optimal penetration may be determined by the following equation (5.1):

$$n = \frac{\pi\sqrt{2J}}{C} \qquad (5.1)$$

where J is the jet-to-mainstream momentum-flux ratio, and C is a constant whose value is 2.5 if an optimum, single row injection is desired. Note that this relation includes the assumption that the "optimum" spacing for a rectangular duct applies at the radius that divides the can into equal area can and annular sections (Holdeman, 1993). In the reacting experiment where J=57, the equation yields an optimal configuration of 13.4 holes. This calculation corroborates the designation of the 14-hole case as the optimal reacting case tested, but also suggests that distributions of an even higher if not comparable uniformity may be attained for a 13-hole configuration.

The corresponding cross-sectional sector plots for O_2 (Figure 5.8) show the jets entering the crossflow symmetrically for each module. It is observed again from the O_2 sector plots that increasing the number of holes lowers jet penetration. By the orifice trailing edge all of the jet fluid should have entered and been accounted for in Plane 4. The sector cross-sections show a larger bulk of jet fluid occurring per orifice in the 8-hole case and a successive decrease in bulk jet fluid per orifice as the number of orifices increases. This decrease in mass flow per orifice is attributed to the decrease in area per orifice, because the jet velocity through each orifice is constant for all six configurations. Decreasing the individual jet mass flow rate decreases the jet momentum, which consequently diminishes jet penetration into the crossflow.

The stratified concentration distributions at z/R=1 (Plane 5) differ substantially from Plane 4, which is situated at the orifice trailing edge. For the overpenetrating cases (8, 9, 10, 12 holes), reaction as seen by a decreased O_2 concentration occurs beyond the z/R=1 plane but is not as substantial as the further reaction that occurs beyond this plane for the optimal 14-hole and the

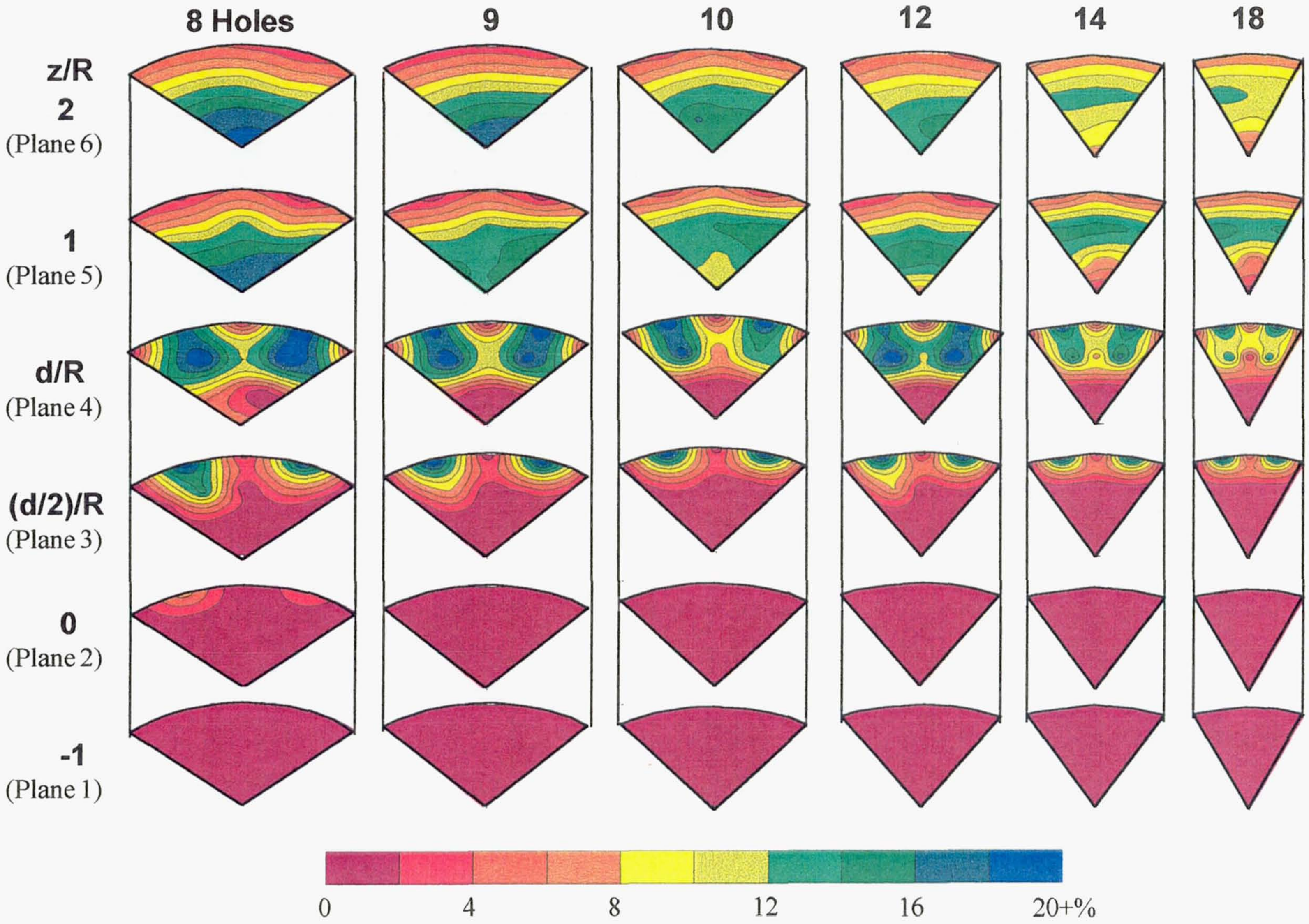

Figure 5.8 Sector Comparison of O_2 Concentration Profiles

underpenetrating 18-hole cases. Increasing the number of holes increases the total circumference, or the total available surface area of reaction between jet and rich reacting product, and this coupled with a near-optimal degree of penetration results in further reaction beyond z/R=1. The 18-hole case, though producing underpenetrating jets, does not produce a severe case that cause the jets to flow along the module wall and decrease the availability of the jet surface area that allows for further reaction.

The experiment was designed to transition from a ϕ=1.7, fuel-rich section (seen as Plane 1) to a ϕ=0.45, fuel-lean section (seen downstream of the jet orifices as Planes 5 and 6). For propane combustion at an equivalence ratio ϕ=0.45 at room temperature and pressure, the NASA equilibrium code predicts an O_2 concentration of 11.1%. From the scale for the O_2 concentration profiles, 11.1% falls within the yellow-green color band, which spans from 10-12% concentration. The O_2 sector plots in Figure 5.8 show that by the z/R=2 plane, the 14- and 18-hole configurations yield larger areas of the 10-12% color band.

A comparison of the CO_2 concentration profiles for all six hole configurations (Figures 5.9 and 5.10) yields similar observations gained from the O_2 species profiles in regard to the distribution of species concentrations. From the axial profiles (Figure 5.9) either the 14- or the 18-hole case appears to produce a more evenly dispersed CO_2 field downstream of the orifices. The sector profiles (Figure 5.10) offer a better viewpoint which shows the 14-hole case containing the least amount of gradient bands, or the most uniform profile

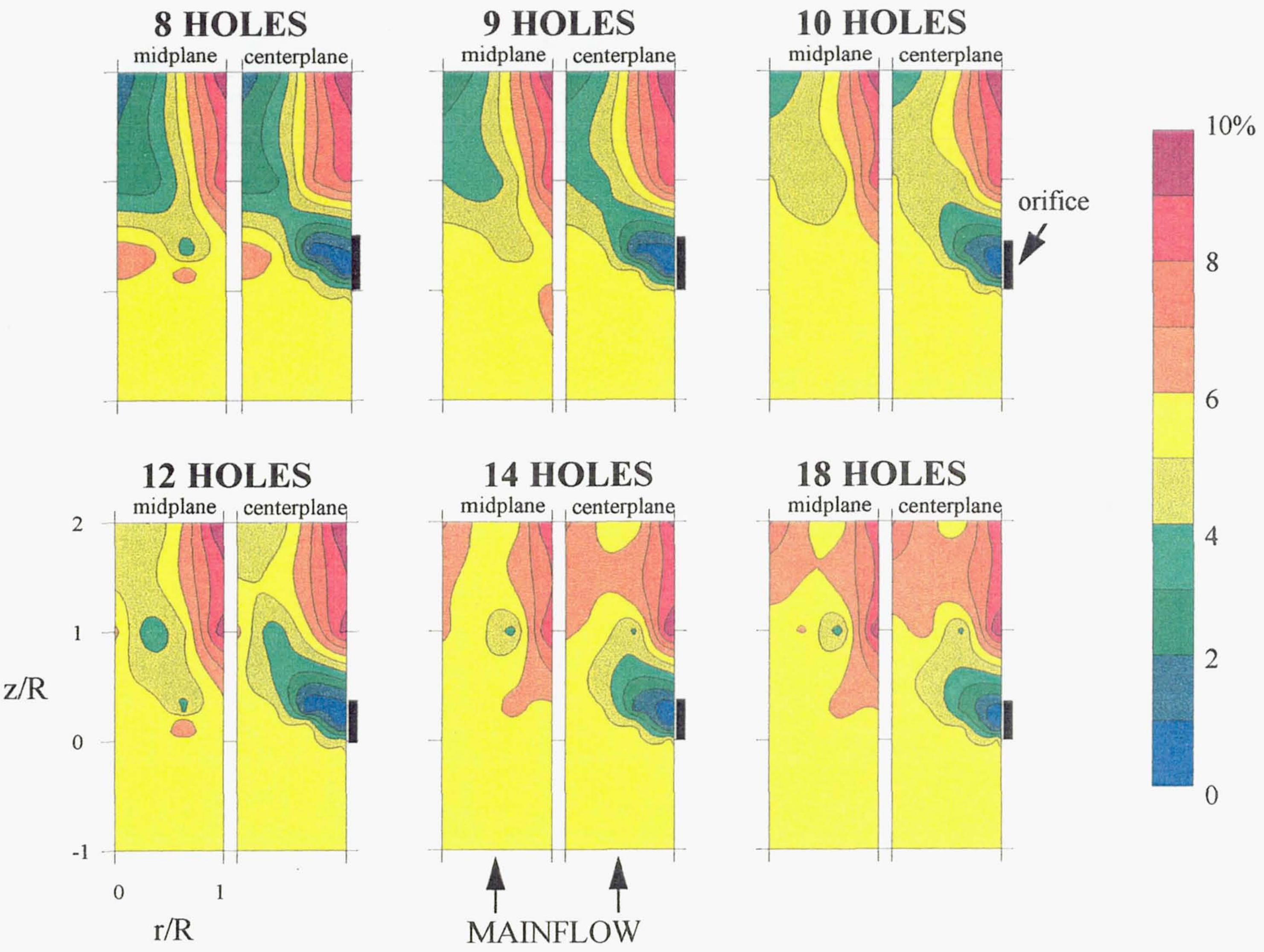

Figure 5.9 Axial History of CO_2 Concentrations at Two Radial-Axial Cross Sections

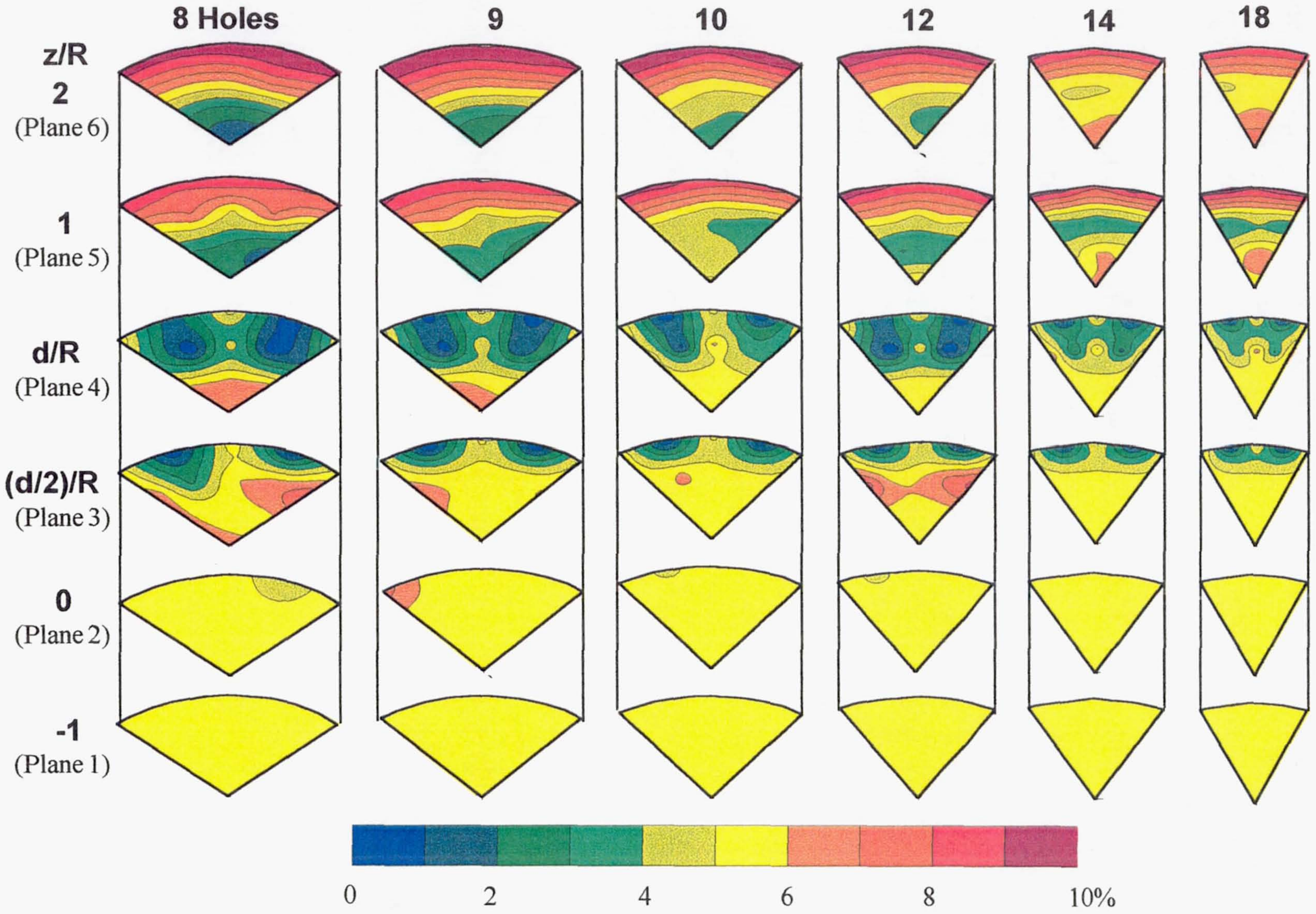

Figure 5.10 Sector Comparison of CO_2 Concentration Profiles

at the z/R=2 plane. The NASA equilibrium code prediction of a 5.47% CO_2 concentration for ϕ=0.45 falls within the yellow color band on the CO_2 plots. In the sector plots the 14-hole module exhibits a larger area with the yellow color band.

Both the 14- and 18-hole cases appear to produce the highest overall amount of CO_2 distributed in the sector plane at the z/R=1 and z/R=2 planes, which suggests that more complete reaction processes have occurred. In addition, both of these cases also show a higher degree of reaction occurring past the z/R=1 plane that was noted earlier in the O_2 sector plots.

A sense of the extent of reaction can be gleaned from the radial-axial CO profiles (Figure 5.11). Between z/R=1 and z/R=2, the presence of CO in the wake of the jet coupled with an increase of CO_2 in the same region suggests that the reaction of CO is a major contributor to the increased CO_2 at the wall (see Figure 5.9). As the number of orifices is increased, the pocket of rich CO-laden gases in the jet wake decreases in size and concentration until it is all nearly consumed by the 18-hole case. However, only the 18-hole case shows a higher CO concentration between 2.6 and 5.2% in the core by the final z/R=2 plane. The evidence of a rich product core in the 18-hole case supports its underpenetration designation.

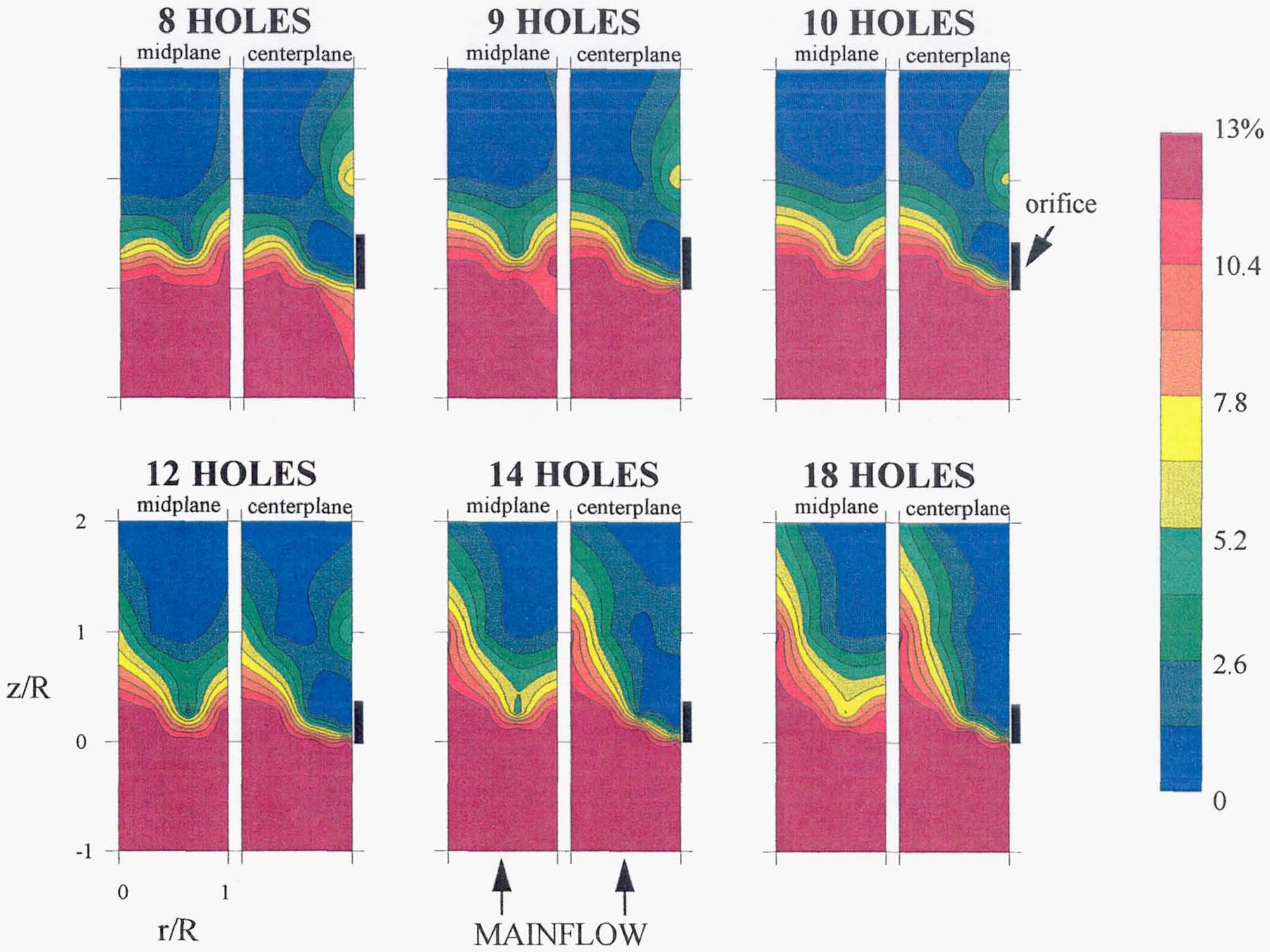

Figure 5.11 Axial History of CO Concentrations at Two Radial-Axial Cross Sections

Figure 5.12 shows the planar cross-sectional view of the CO distribution. For all of the modules a majority of CO has been consumed by the z/R=1 plane. However, CO-rich pockets in the jet wake are observed in the same plane for the overpenetrating 8- through 10-hole cases, a CO-rich core is seen in both the optimal 14-hole and the underpenetrating 18-hole cases, and a balance of both is seen in the overpenetrating 12-hole case. Curiously, by the z/R=2 plane, only the 12-hole case exhibits a uniform, low CO-concentration band less than 1.3%. The NASA equilibrium code prediction of CO concentration from atmospheric propane combustion at $\phi=0.45$ is in the ppb range and can be considered negligible, which leaves only the 12-hole case with the achievement of a lower overall CO concentration by the z/R=2 plane.

The HC contour plots (Figures 5.13 and 5.14) proffer little significant information. A comparison of HC profiles for each module in both axial and sector views shows a near-total consumption of HC which leads to a near-total concentration distribution of HC below 1% by the orifice trailing edge (Plane 4).

A NO_x profile comparison (Figures 5.15 and 5.16) yields the same general observations made in the other species profile comparisons. Similar to the CO_2 species distribution, the bulk of NO_x formation appears downstream of the orifices along the wall region for all cases, but also along the center region for the 14- and 18-hole cases. Among the six modules, the 14-hole case produces the most uniform NO_x concentrations across the z/R=1 and z/R=2 planes (see Figure 5.16).

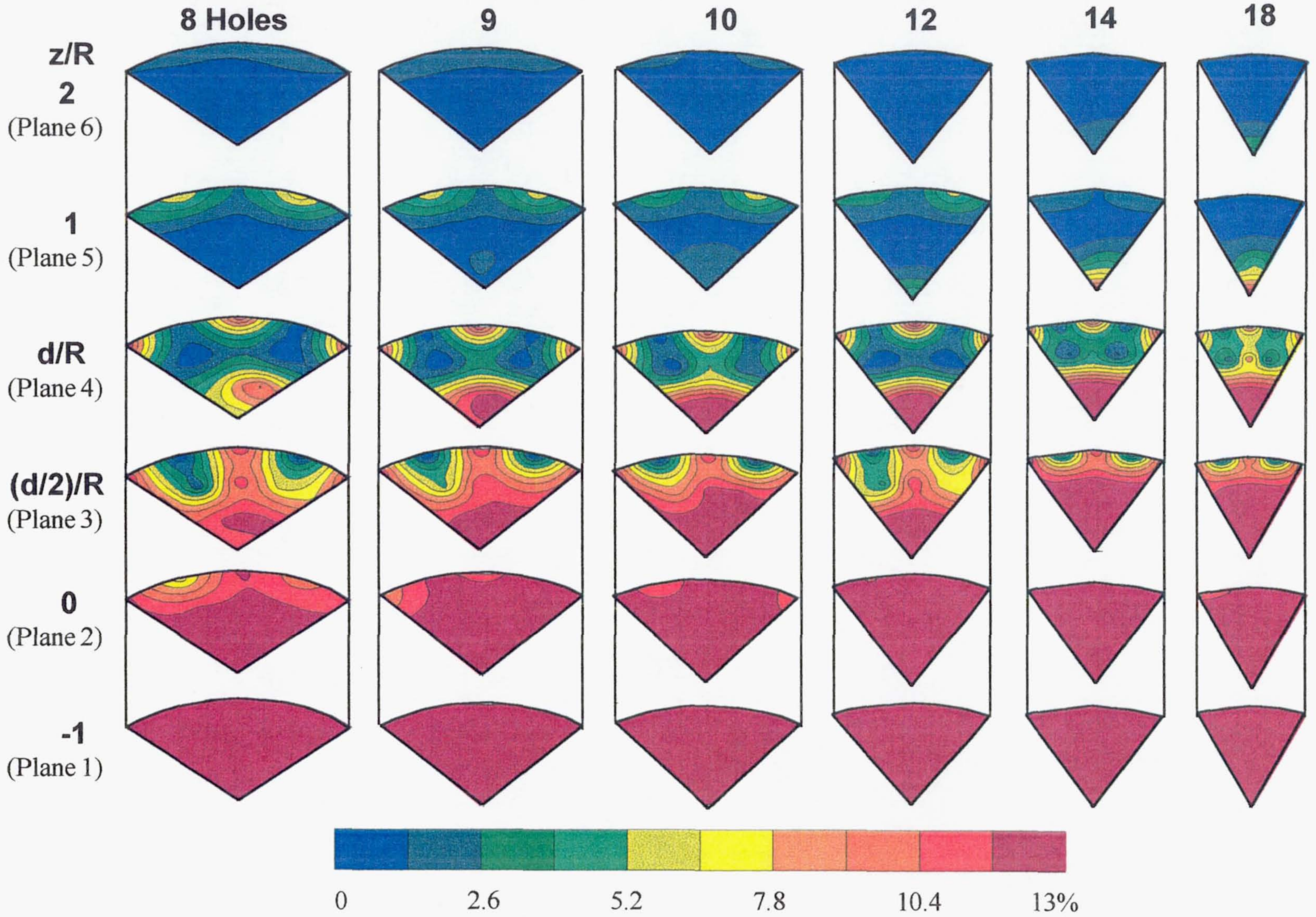

Figure 5.12 Sector Comparison of CO Concentration Profiles

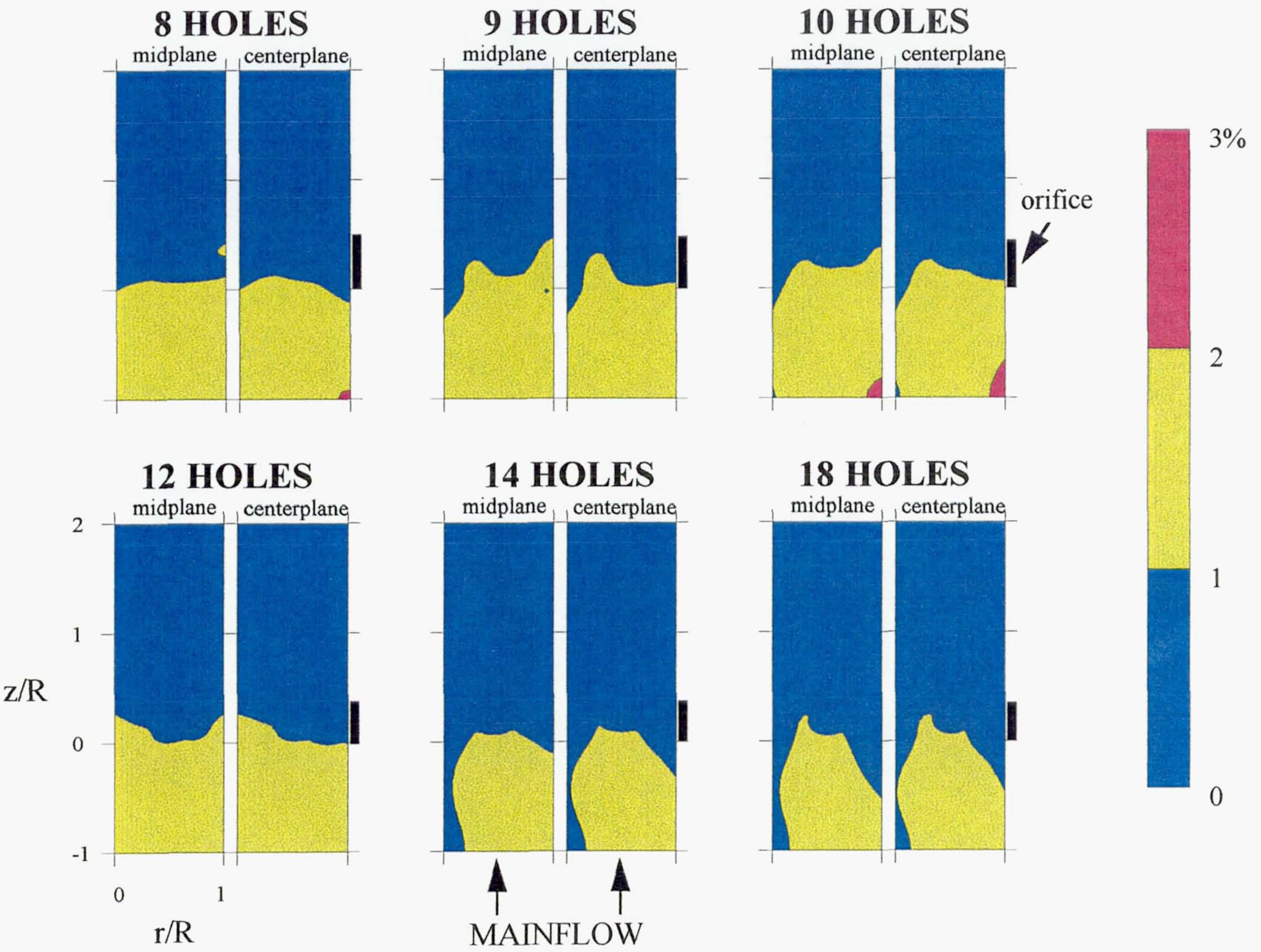

Figure 5.13 Axial History of HC Concentrations at Two Radial-Axial Cross Sections

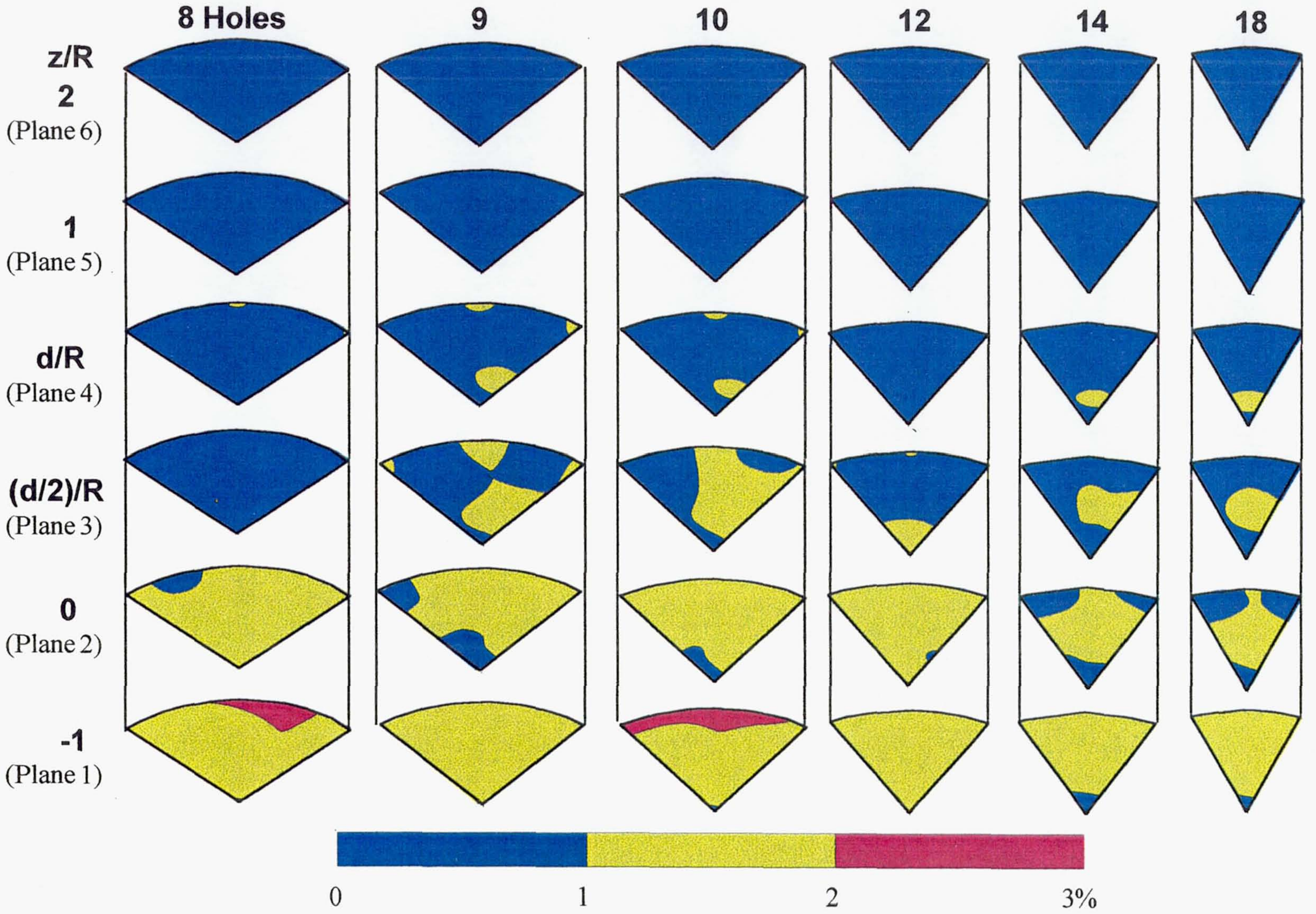

Figure 5.14 Sector Comparison of HC Concentration Profiles

The measured concentrations of NO_x were found to be less than 40 ppm per point. It is emphasized, however, that the NO_x concentrations measured in this experiment may not be indicative of thermal NO_x behavior because the experiment is not run with air preheat, and peak temperatures are therefore suppressed. Any correlation made at this juncture between jet mixing and NO_x production would not be reflective of situations occurring at actual engine operating conditions.

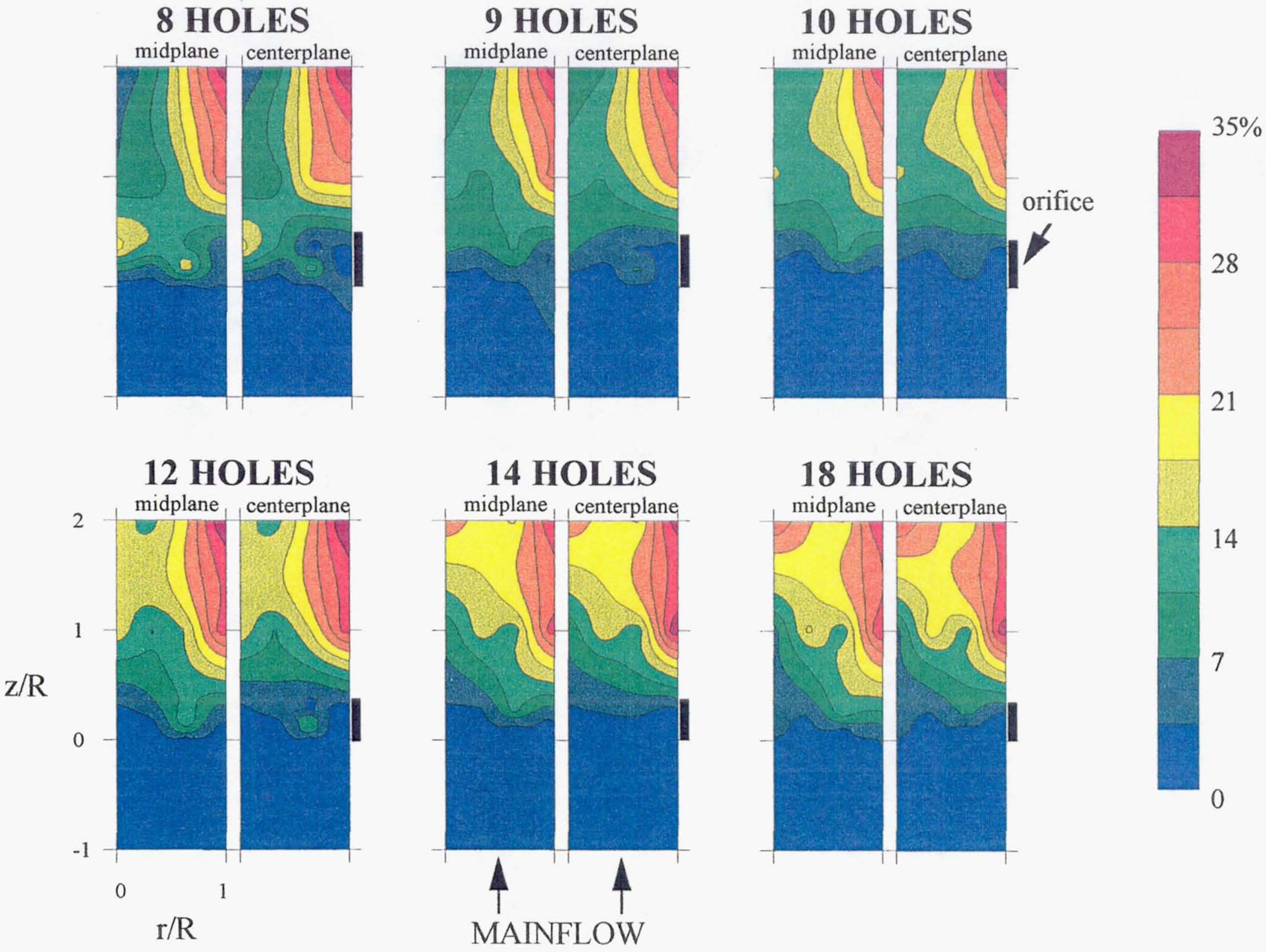

Figure 5.15 Axial History of NO_X Concentrations at Two Radial-Axial Cross Sections

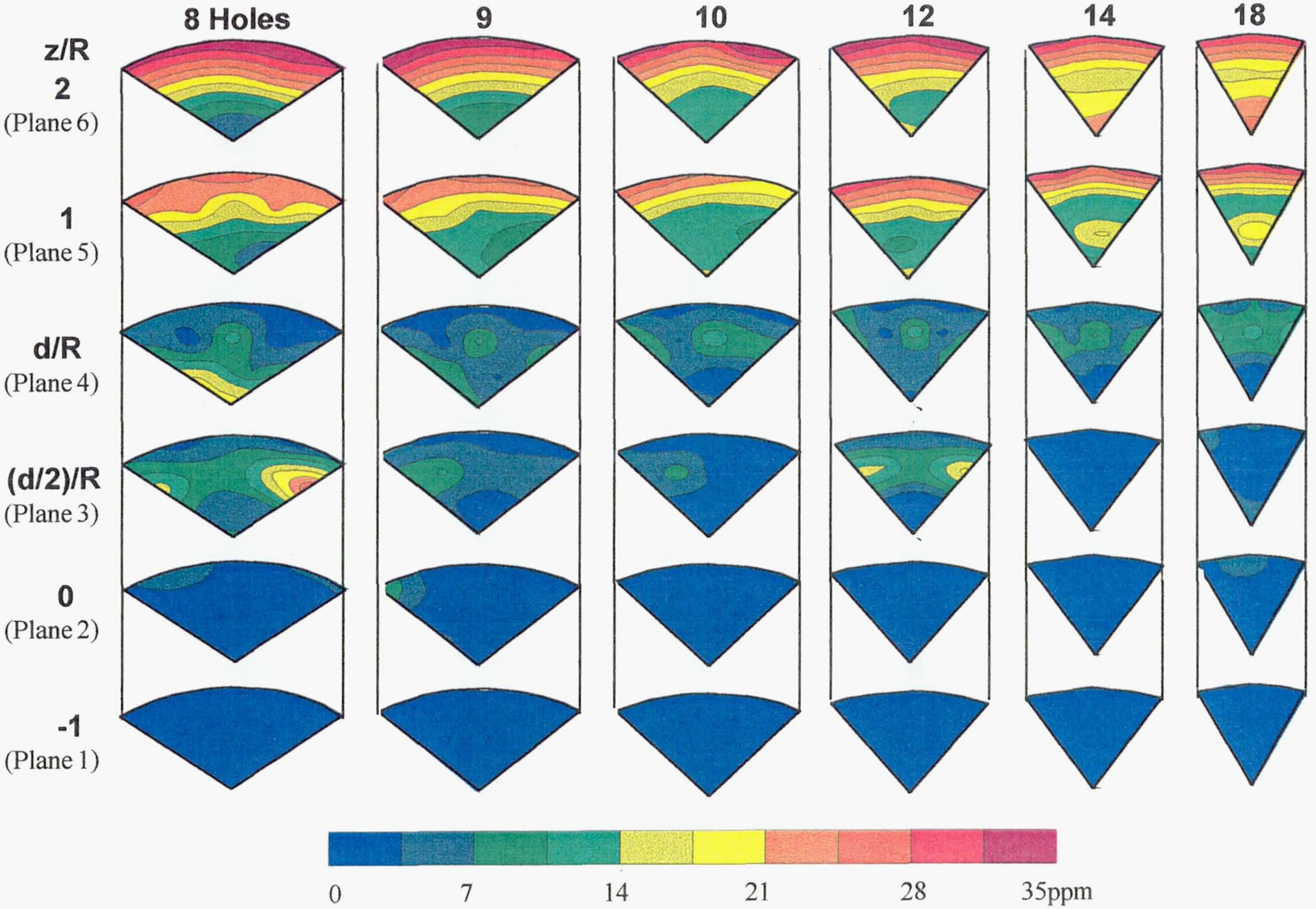

Figure 5.16 Sector Comparison of NO_X Concentration Profiles

CHAPTER 6

SUMMARY AND CONCLUSIONS

6.1 Conclusions

An experiment has been designed and successfully demonstrated to provide a test bed for the study of jet mixing in a rich reacting environment. In this initial demonstration, it was possible to determine the jet trajectory, as well as mixing and reacting processes, for six round hole configurations.

For a set momentum-flux ratio J = 57 and mass-flow ratio MR = 2.5 it was found (under atmospheric conditions) that:

- The data grid density and planar measurement distribution provide sufficient information to form general inferences and comparisons of mixing and reacting properties between various multiple-orifice configurations.
- Profiles of temperature and species concentration can be used to an extent to indicate general zones where mixing and reacting processes occur. However, the separation of reaction from mixing cannot, at this juncture, be determined. A conserved scalar measurement of, for example, an inert gas tracer will enable a pure characterization of mixing in the reacting flow field.

- The jet wake is the site of further reaction downstream of the one duct radius demarcation, and is seen by lower CO values coupled with higher CO_2 and NO_x values.
- Jet trajectories may be inferred from charting either the minimal temperatures or the maximal O_2 species concentrations as a function of downstream distance from the jet orifice.
- The temperature and species concentration profiles for the six configurations share the same general flow characteristics relative to jet penetration dynamics.
- When jet penetration increases beyond optimal as in the 8-, 9-, 10-, and 12-hole cases tested, the jet mass gravitates to and accumulates in the central core of the mixer rather than dispersing laterally throughout the radius of the mixer.
- When jet penetration decreases beyond the optimal point as in the 18-hole case, a hotter, rich core is allowed to bypass the jet region without completing the reaction toward the fuel-lean state.
- Of the six hole configurations tested, the 14-hole module exhibits jet trajectory penetration close to the mixer half-radius and produces the most complete reaction and the best uniform mixing by the z/R=2 plane.
- The overpenetrating 8-, 9-, and 10-hole cases yielded little reaction beyond the z/R=1 plane while the optimal 14-hole, the slighty

overpenetrating 12-hole, and the slightly underpenetrating 18-hole cases showed substantial reaction occurring after the plane.

- Although the profiles obtained are able to indicate general flow characteristics that allow for comparison between mixers, a denser data grid would be advantageous in order to capture specific gradients more precisely.

6.2 Recommendations

The results from this experiment present further questions that may be answered by:

- Acquiring mixture fraction fields using an inert gas tracer to establish the extent of mixing versus reaction in the flow field.
- Obtaining time-resolved measurements of temperature and species concentrations to determine the cause of jet flow asymmetry in the orifice vicinity.
- Determining the velocity flow field to quantify mass-flow rates of species concentration in the plane.
- Preheating the mainflow air to investigate the effect of higher inlet temperatures on jet reaction and mixing processes as well as on NO_x production.
- Comparing mixture and reaction fields from the reacting case to a non-reacting case performed at the same momentum-flux ratio J=57.

CHAPTER 7

REFERENCES

Andreopoulos, J. (1985). On the Structure of Jets in a Crossflow. *Journal of Fluid Mechanics*, **157**, 163-197.

Andreopoulos, J. and Rodi, W. (1984). Experimental Investigation of Jets in a Crossflow. *Journal of Fluid Mechanics*, **138**, 93-127.

Bain, D.B., Smith, C.E., and Holdeman, J.D. (1995). CFD Mixing Analysis of Axially Opposed Rows of Jets Injected into Confined Crossflow. *Journal of Propulsion and Power*, **11**, 885-893. (Also AIAA-93-2044 and NASA TM 106179).

Bain, D.B., Smith, C.E., and Holdeman, J.D. (1994). CFD Assessment of Orifice Aspect Ratio and Mass Flow Ratio on Jet Mixing in Rectangular Ducts. AIAA-94-0218 (Also NASA TM 106434).

Bain, D.B, Smith, C.E., and Holdeman, J.D. (1992). CFD Mixing Analysis of Jets Injected from Straight and Slanted Slots into Confined Crossflow in Rectangular Ducts. AIAA-92-3087 (Also NASA TM 105699).

Bates, D.R. and Nicolet, M. (1950). The Photochemistry of Atmospheric Water Vapour. *Journal of Geophysical Research*, **55**, 301.

Chapman, S. (1930). A Theory of Upper-Atmospheric Ozone. *Memoirs of the Royal Meteorological Society*, **3**, 103-125.

Climatic Impact Committee. (1975). *Environmental Impact of Stratospheric Flight: Biological and Climatic Effects of Aircraft Emissions in the Stratosphere*, National Academy of Sciences, Washington, D.C.

Fearn, R. and Weston, R.P. (1974). Vorticity Associated with a Jet in a Cross Flow. *AIAA Journal*, **12**, 1666-1671.

Fenimore, C.P. (1971). Formation of Nitric Oxide in Premixed Hydrocarbon Flames. 13th Symposium (International) on Combustion, 373-380.

Glassman, I. (1987). *Combustion*, Academic Press, Inc., Orlando.

Grobecker, A.J., Coronetti, S.C., Cannon Jr., R.H. (1974). The Effects of Stratospheric Pollution by Aircraft: Report of Findings. DOT-TS-75-50, December.

Hatch, M.S., Sowa, W.A., and Samuelsen, G.S. (1996). Influence of Geometry and Flow Variation on Jet Mixing and NO Formation in a Model Staged Combustor With Eight Orifices. NASA Contractor Report 194473.

Hatch, M.S., Sowa, W.A., Samuelsen, G.S., and Holdeman, J.D. (1995a). Jet Mixing into a Heated Cross Flow in a Cylindrical Duct: Influence of Geometry and Flow Variations. *Journal of Propulsion and Power*, **11**, 393-402. (Also AIAA-92-0773 and NASA TM 105390).

Hatch, M.S., Sowa, W.A., Samuelsen, G.S., and Holdeman, J.D. (1995b). Influence of Geometry and Flow Variations on NO Formation in the Quick Mixer of a Staged Combustor. *Journal of Engineering for Gas Turbines and Power* (in press). (Also NASA TM 105639).

Heitor, M.V. and Whitelaw, J.H. (1986). Velocity, Temperature, and Species Characteristics of the Flow in a Gas-Turbine Combustor. *Combustion and Flame*, **64**, 1-32.

Holdeman, J.D. (1993). Mixing of Multiple Jets with a Confined Subsonic Crossflow. *Progress in Energy and Combustion Science,* **7**, 31-70. (See also AIAA-91-2458 and NASA TM 104412).

Horiba Instruments, Inc. (1992). Horiba Instruction Manual for AIA-210/220 Infrared Analyzer, Manual #091891, 2-1 to 2-2.

Horiba Instruments, Inc. (1990). Horiba Instruction Manual for CLA-220, Chemiluminescent Analyzer, Manual #091216, 2-1 to 2-2.

Horiba Instruments, Inc. (1990). Horiba Instruction Manual for FMA-220, FIA-220/MPA-220 Flame Ionization, Magneto-Pneumatic Analyzer, Manual #091217, 2-1 to 2-3.

Howe, G.W., Li, Z., Shih, T.I-P., and Nguyen, H.L. (1991). Simulation of Mixing in the Quick Quench Region of a Rich Burn-Quick Quench Mix-Lean Burn Combustor. AIAA-91-0410.

Johnston, H.S., Kinnison, D.E., and Wuebbles, D.J. (1989). Nitrogen Oxides from High-Altitude Aircraft: An Update of Potential Effects on Ozone. *Journal of Geophysical Research*, **94**, D13, 16351-16363.

Kamotani, Y. and Greber, I. (1972). Experiments on a Turbulent Jet in a Cross Flow. *AIAA Journal*, **10**, 1425-1429.

Karagozian, A.R. (1986). An Analytical Model for the Vorticity Associated with a Transverse Jet. *AIAA Journal*, **24**, 429-436.

Karagozian, A.R., Nguyen, T.T. and Kim, C.N. (1986). Vortex Modeling of Single and Multiple Dilution Jet Mixing in a Cross Flow. *Journal of Propulsion and Power*, **2**, 354-360.

Koff, B.L. (1994). Aircraft Gas Turbine Emissions Challenge. *Journal of Engineering for Gas Turbines and Power*, **116**, 474-477.

Kroll, J.T., Sowa, W.A., Samuelsen, G.S. (1996). Optimization of Orifice Geometry for Cross-Flow Mixing in a Cylindrical Duct. NASA Contractor Report 198482.

Kroll, J.T., Sowa, W.A., and Samuelsen, G.S., and Holdeman, J.D (1993). Optimization of Circular Orifice Jets Mixing into a Heated Cross Flow in a Cylindrical Duct. AIAA-93-0249 (Also NASA TM 105984).

Lefebvre, A.H. (1983). *Gas Turbine Combustion*, Hemisphere Publishing Corporation, Washington.

Liscinsky, D.S., True, B., and Holdeman, J.D. (1996). Crossflow Mixing of Noncircular Jets. *Journal of Propulsion and Power*, **12**, 225-230. (Also AIAA-95-0732 and NASA TM 106865).

Liscinsky, D.S., True, B., and Holdeman, J.D. (1994). Mixing Characteristics of Directly Opposed Rows of Jets Injected Normal to a Crossflow in a Rectangular Duct. AIAA-94-0217 (Also NASA TM 106477).

Liscinsky, D.S., True, B., and Holdeman, J.D. (1993). Experimental Investigation of Crossflow Jet Mixing in a Rectangular Duct. AIAA-93-2037 (Also NASA TM 106152).

Liscinsky, D.S., True, B., Vranos, A., and Holdeman, J.D. (1992). Experimental Study of Cross-Stream Mixing in a Rectangular Duct. AIAA-92-3090 (Also NASA TM 105694).

Masters, G.M. (1991). *Introduction to Environmental Engineering and Science*, Prentice Hall, Englewood Cliffs, New Jersey.

Noyce, J. R., Sheppard, C.G.W. and F. D. Yamba. (1981). Measurements of Mixing and Species Concentrations Within a Gas Turbine Combustor. *Combustion Science and Technology*, **25**, 209-217.

Oechsle, V.L. and Holdeman, J.D. (1995). Numerical Mixing Calculations of Confined Reacting Jet Flows in a Cylindrical Duct. AIAA-95-0733 (Also NASA TM 106736).

Oechsle, V.L., Mongia, H.C., and Holdeman, J.D. (1994). Comparison of the Mixing Calculations of the Reacting and Nonreacting Flows in a Cylindrical Duct. AIAA-92-3090 (Also NASA TM 106194).

Oechsle, V.L., Mongia, H.C., and Holdeman, J.D. (1993). An Analytical Study of Dilution Jet Mixing in a Cylindrical Duct. AIAA-93-2043 (Also NASA TM 106181).

Oechsle, V.L., Mongia, H.C., and Holdeman, J.D. (1992). A Parametric Numerical Study of Mixing in a Cylindrical Duct. AIAA-92-3088 (Also NASA TM 105695).

Rowland, F.S. (1991). Stratospheric Ozone Depletion. *Annual Review of Physical Chemistry*, **42**, 731-768.

Samuelsen, G.S. (1975). The Combustion Aspects of Air Pollution. *Advances in Environmental Science and Technology*, **5**, 219-323.

Shaw, R.J. (1991). Engine Technology Challenges for a 21st Century High Speed Civil Transport. NASA TM 104363.

Sherif, S.A. and Pletcher, R.H. (1989). Measurements of the Flow and Turbulence Characteristics of Round Jets in Crossflow. *Journal of Fluids Engineering*, **111**, 165-171.

Smith, C.E., Talpallikar, M.V., and Holdeman, J.D. (1991). A CFD Study of Jet Mixing in Reduced Flow Areas for Lower Combustor Emissions. AIAA-91-2460 (Also NASA TM 104411).

Sowa, W.A., Kroll, J.T., Samuelsen, G.S., and Holdeman, J.D. (1994). Optimization of Orifice Geometry for Cross-Flow Mixing in a Cylindrical Duct. AIAA-94-0219 (Also NASA TM 106436).

Strack, W.C. and Morris, Jr., S.J. (1988). The Challenges and Opportunities of Supersonic Transport Propulsion Technology. AIAA-88-2985.

Tacina, R.R. (1990). Low NOx Potential of Gas Turbine Engines. AIAA Paper 90-0550.

Talpallikar, M.V., Smith, C.E., Lai, M.C. and Holdeman, J.D. (1992). CFD Analysis of Jet Mixing in Low NO_x Flametube Combustors. *Journal of Engineering for Gas Turbines and Power*, **114**, 416-424. (Also ASME-91-GT-217; NASA TM 104466).

Vranos, A., Liscinsky, D.S., True, B., and Holdeman, J.D. (1991). Experimental Study of Cross-Stream Mixing in a Cylindrical Duct. AIAA-91-2459 (Also NASA TM 105180).

Wayne, R.P. (1985). *Chemistry of Atmospheres: An Introduction to the Chemistry of the Atmospheres of Earth, the Planets, and Their Satellites*, Clarendon Press, Oxford.

Zarzalis, N., Joos, F., Glaeser, B., and Ripplinger, T. (1992). NOx-Reduction by Rich-Lean Combustion. AIAA-92-3339.

Zeldovich, J. (1946). The Oxidation of Nitrogen in Combustion and Explosions. *Acta Physicochim, URSS*, **21**, 577-628.

APPENDIX A

ORIFICE AREA CALCULATION

Design Conditions:

mass flow ratio	$MR := 2.5$
main flow cross-sectional area	$A_m := 0.005027 \cdot m^2$
jet to main flow momentum-flux ratio	$J := 40$
jet temperature	$T_j := 298K$
main flow temperature	$T_m := 1800K$
discharge coefficient	$C_d := 0.65$

$$J = \frac{(\text{jet density})*(\text{jet velocity})^2}{(\text{main density})*(\text{main velocity})2}$$

where universal gas constant R and pressure P of jets and main flow are assumed constant, and velocity is represented by: mass flow rate/density/area.

Effective Jet Area

$$A_{jet\_eff} := MR \cdot A_m \cdot \sqrt{\frac{1}{J} \cdot \frac{T_j}{T_m}} \qquad A_{jet\_eff} = 808.52 \cdot mm^2$$

Geometric Jet Area

$$A_{jet\_geom} := \frac{A_{jet\_eff}}{C_d} \qquad A_{jet\_geom} = 1.244 \cdot 10^3 \cdot mm^2$$

APPENDIX B

EMISSION ANALYZER OPERATION PRINCIPLES

The descriptions of the basic operation principles behind the non-dispersive infrared (NDIR), paramagnetic, flame ionization detection (FID), and chemiluminescence analyzers were summarized from the Horiba Instruments instruction manuals #091891, #091217, and #091216, respectively.

B.1 Infrared Analyzer

The measurement of CO and CO_2 concentrations in the experiment was accomplished by non-dispersive infrared analysis. The non-dispersive infrared analyzer (NDIR) (Figure B.1) distinguishes between different molecules by their unique infrared absorption band. The absorptivity of the sample in a specific band is proportional to the species concentration.

In the NDIR analyzer, a light source emits infrared light which is transformed into intermittent light by a chopper. The intermittent light is then passed through a measurement cell where it is absorbed by the sample. The absorptivity is compared by the detector to a reading from an adjacent reference cell. The change in intensity of light between the sample and reference cells causes a membrane in the detector to vibrate, which generates a measurable electrical signal.

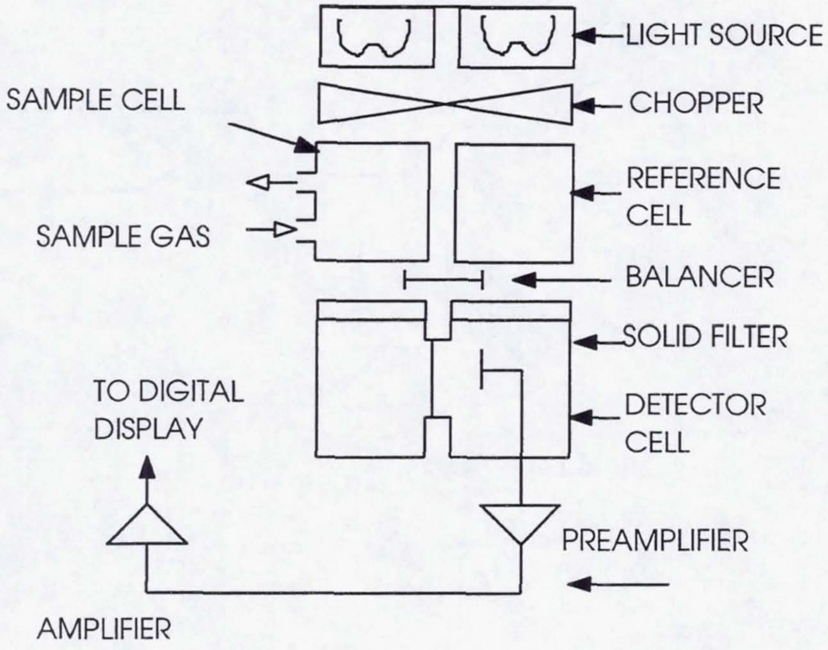

Figure B.1 Basic NDIR Detector Components
(Adapted from Horiba Manual #091891)

B.2 Flame Ionization Detector (FID)

Ionization occurs when a hydrocarbon sample is burned with a hydrogen flame. In the flame ionization detector (FID) (Figure B.2) a DC voltage is applied across two electrodes situated on opposite sides of the flame. The electrical potential induces a current, or movement of the ions produced from the burned hydrocarbon sample, which is proportional to the number of carbon atoms in the hydrocarbon sample. The current is amplified and converted to a voltage differential that is measured.

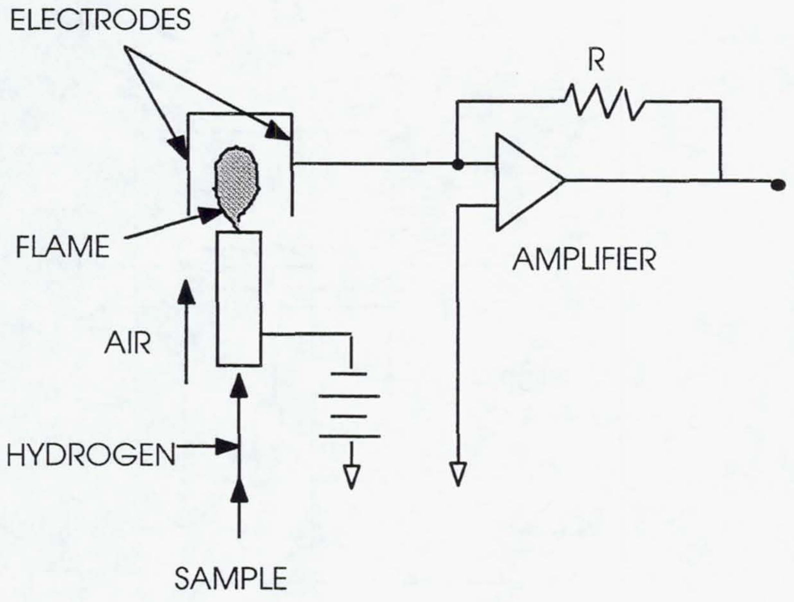

Figure B.2 Basic FID Components (Adapted from Horiba Manual #091217)

B.3 Magneto-Pneumatic Analyzer

The magneto-pneumatic analyzer (Figure B.3) is used to measure oxygen concentrations in a sample by utilizing the paramagnetic properties of gaseous oxygen. An uneven magnetic field applied to such a gas causes the molecules to migrate toward the portion of the field with the strongest attraction. The accumulation of gas raises the pressure at that point.

The pressure rise ΔP is directly proportional to the concentration C of paramagnetic gas, as shown in equation (B.1):

$$\Delta P = (1/2)*H^2*X*C \qquad \text{(B.1)}$$

where H represents the magnetic field strength and X represents the magnetic susceptibility of the paramagnetic gas. The changes in pressure are converted into electrical signals by a condenser microphone. The resulting electrical output is linearly proportional to the oxygen concentration.

To eliminate the pressure rise between sampling, a non-paramagnetic gas such as nitrogen (N_2) is required in the operation of the analyzer.

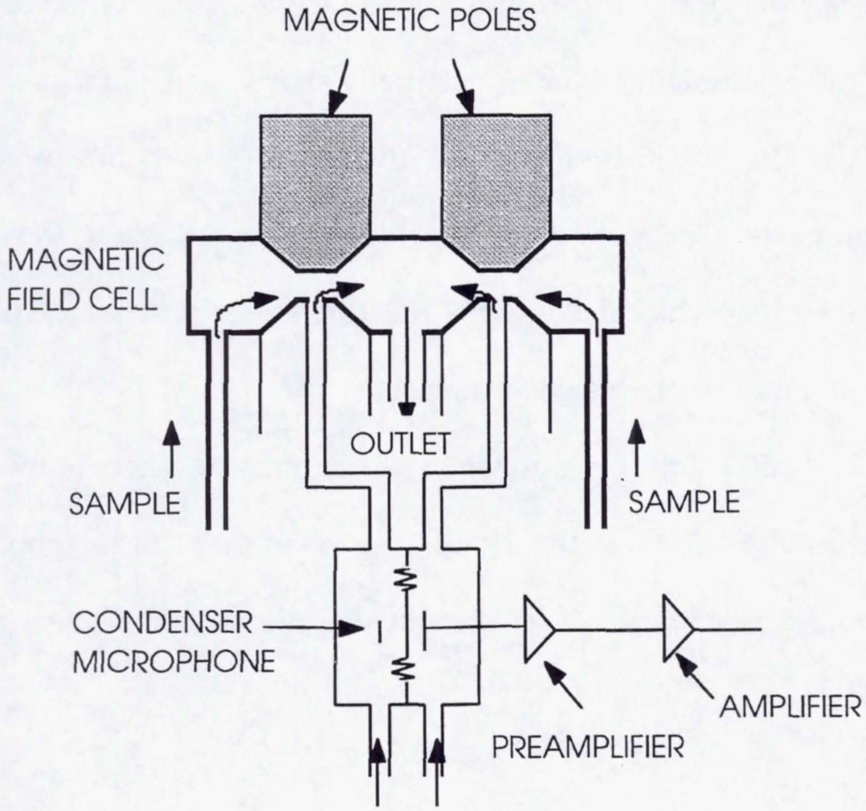

Figure B.3 Basic Paramagnetic Detector Components
(Adapted from Horiba Manual #091217)

B.4 Chemiluminescence

Chemiluminescence is used to detect NO_x by initiating a reaction sequence between the sample and ozone (O_3) to emit light. The sample is first routed through a chamber that dissociates the NO_2 present in the sample into NO. The gas is then channeled to another chamber where it reacts with O_3 in the following set of reactions listed as equations B.2 and B.3:

$$NO + O_3 \rightarrow NO_2^* + O_2 \qquad (B.2)$$

$$NO_2^* \rightarrow NO_2 + h\upsilon \qquad (B.3)$$

where h is Planck's constant, υ refers to the frequency of the light emitted, and the asterisk designates the electronically excited state of the molecule. The light emitted in the second reaction (Equation B.3) is measured by a silicon photodiode. The measurement is directly proportional to the concentration of the total NO, which includes the NO_2 dissociated prior to reaction with O_3, that entered the detector reaction chamber.

Unlike other instruments which measure chemiluminescence with a photomultiplier tube, the Horiba model utilizes silicon photodiodes, which increases the range of wavelength detection while decreasing noise in the reading.

APPENDIX C

EXPERIMENTAL CONDITIONS AND SETTINGS

Atmospheric, Room Temperature $P_{STD} := \left(1.013 \cdot 10^{5}\right) \cdot \frac{N}{m^2}$ $T_{STD} := 298K$

Gas Constants $R_{C3H8} := 0.1885 \cdot \frac{kJ}{kg \cdot K}$ $R_{air} := 0.2870 \cdot \frac{kJ}{kg \cdot K}$

Densities of propane and air at standard conditions. $\rho_{C3H8} = 1.803 \cdot kg \cdot m^{-3}$ $\rho_{air} = 1.184 \cdot kg \cdot m^{-3}$

Reacting Crossflow ("main") and Jet Areas and Temperatures

$A_{main} := 5.027 \cdot 10^{-3} \cdot m^2$ $T_{main} := 1500K$

$A_{jets\_geom} := 1.237 \cdot 10^{-3} \cdot m^2$ $T_{jets} := 480K$

Pressure Drop Across Quick-Mixing Orifices

$\Delta P_{jets} := 4480 \cdot Pa$

Experimental Mass Flow Rates

$Mass\_flow_{fuel} = 0.00296 \cdot kg \cdot sec^{-1}$

$Mass\_flow_{air} = 0.0275 \cdot kg \cdot sec^{-1}$ $Mass\_flow_{jets} = 0.0752 \cdot kg \cdot sec^{-1}$

Total rich crossflow mass flow rate (fuel and air):

$Mass\_flow_{main} := Mass\_flow_{air} + Mass\_flow_{fuel}$

$Mass\_flow_{main} = 0.0305 \cdot kg \cdot sec^{-1}$

C.1 CALCULATION OF EQUIVALENCE RATIO

Rich Experimental Fuel-Air Ratio (FAR):

$$FAR_{rich} := \frac{Mass\_flow_{fuel}}{Mass\_flow_{air}} \qquad FAR_{rich} = 0.108$$

Stoichiometric Fuel-Air Ratio:

Stoichiometric reaction assumes no excess fuel or air in products of complete combustion. The following is a mass balance of the combustion of propane.

$$C_3H_8 + 5(O_2 + 3.71\ N_2) \dashrightarrow 3CO_2 + 4H_20 + 18.55N_2$$

Species Molecular Weights

$$MW_C := 12 \cdot \frac{g}{mol} \qquad MW_{O2} := 32 \cdot \frac{g}{mol}$$

$$MW_H := 1 \cdot \frac{g}{mol} \qquad MW_{N2} := 28 \cdot \frac{g}{mol}$$

$$MW_{C3H8} := 3 \cdot MW_C + 8 \cdot MW_H$$

$$MW_{air} := MW_{O2} + 3.71 \cdot MW_{N2}$$

$$FAR_{stoich} := \frac{1 \cdot mol \cdot MW_{C3H8}}{5 \cdot mol \cdot MW_{air}} \qquad FAR_{stoich} = 0.065$$

Rich Zone Equivalence Ratio

$$\phi_{\text{rich}} := \frac{\text{FAR}_{\text{rich}}}{\text{FAR}_{\text{stoich}}} \qquad \phi_{\text{rich}} = 1.66$$

Overall Fuel-Air Ratio (FAR):

$$\text{FAR}_{\text{overall}} := \frac{\text{Mass\_flow}_{\text{fuel}}}{\text{Mass\_flow}_{\text{air}} + \text{Mass\_flow}_{\text{jets}}} \qquad \text{FAR}_{\text{overall}} = 0.029$$

Overall Equivalence Ratio

$$\phi_{\text{overall}} := \frac{\text{FAR}_{\text{overall}}}{\text{FAR}_{\text{stoich}}} \qquad \phi_{\text{overall}} = 0.45$$

C.2 CALCULATION OF MOMENTUM-FLUX RATIO J

Calculate main flow momentum flux

$$\rho_{main} := \frac{P_{STD}}{R_{air} \cdot T_{main}} \qquad \rho_{main} = 0.235 \cdot kg \cdot m^{-3}$$

$$V_{main} := \frac{Mass\_flow_{main}}{\rho_{main} \cdot A_{main}} \qquad V_{main} = 25.758 \cdot m \cdot sec^{-1}$$

$$Mom\_flux_{main} := \rho_{main} \cdot V_{main}^{2} \qquad Mom\_flux_{main} = 156 \cdot kg \cdot m^{-1} \cdot sec^{-2}$$

Calculate total jet momentum-flux

$$P_{jets} := P_{STD} + \Delta P_{jets} \qquad \rho_{jets} := \frac{P_{jets}}{R_{air} \cdot T_{jets}}$$

$$V_{jets} := \sqrt{2 \cdot \frac{\Delta P_{jets}}{\rho_{jets}}} \qquad \rho_{jets} = 0.768 \cdot kg \cdot m^{-3}$$

$$V_{jets} = 108.022 \cdot m \cdot sec^{-1}$$

$$Mom\_flux_{jets} := \rho_{jets} \cdot V_{jets}^{2} \qquad Mom\_flux_{jets} = 8.96 \cdot 10^{3} \cdot kg \cdot m^{-1} \cdot sec^{-2}$$

Momentum Flux Ratio J

$$J := \frac{Mom\_flux_{jets}}{Mom\_flux_{main}} \qquad J = 57$$

C.3 CALCULATION OF FLOW PARAMETERS

Reference Velocity

$$\rho_3 := \frac{P_{STD}}{R_{air} \cdot T_{STD}} \qquad \rho_3 = 1.184 \cdot kg \cdot m^{-3}$$

$$Mass\_flow_{ref} := Mass\_flow_{main} + Mass\_flow_{jets}$$

$$Mass\_flow_{ref} = 0.106 \cdot kg \cdot sec^{-1}$$

$$V_{ref} := \frac{Mass\_flow_{ref}}{\rho_3 \cdot A_{main}} \qquad V_{ref} = 17.742 \cdot m \cdot sec^{-1}$$

Mass Flow Ratio MR

$$MR := \frac{Mass\_flow_{jets}}{Mass\_flow_{main}} \qquad MR = 2.47$$

Density Ratio DR

$$DR := \frac{\rho_{jets}}{\rho_{main}} \qquad DR = 3.26$$

Velocity Ratio VR

$$VR := \frac{V_{jets}}{V_{main}} \qquad VR = 4.19$$

Effective Jet Area and Discharge Coefficient

$$A_{jets\_eff} := \frac{Mass\_flow_{jets}}{\rho_{jets} \cdot \sqrt{2 \cdot \frac{\Delta P_{jets}}{\rho_{jets}}}} \qquad A_{jets\_eff} = 9.062 \cdot 10^{-4} \cdot m^2$$

$$C_d := \frac{A_{jets\_eff}}{A_{jets\_geom}} \qquad C_d = 0.733$$

APPENDIX D

MASS BALANCE

Species Molecular Weights

$MW_{CO} := 28$ $MW_{O2} := 32$ $MW_{C3H8} := 44$

$MW_{CO2} := 44$ $MW_{N2} := 28$ $MW_{air} := 28.97$

$MW_{NO} := 30$ $MW_{C} := 12$ $MW_{HC} := 44$

$MW_{H2O} := 18$ $MW_{H} := 1$

Percent of Element in Air

$Air_{O2\%} := 0.2095$ $Air_{N2\%} := 0.7808$

Elemental Stoichiometric Coefficient of Element in H_2O

$\omega_{H} := 2$ $\omega_{O2} := 0.5$

Experimental Measurements

$$M_{fuel} := 0.00296 \cdot \frac{kg}{sec}$$

$$M_{air} := 0.0275 \cdot \frac{kg}{sec}$$

$M_{total} := M_{fuel} + M_{air}$ $M_{total} = 0.03 \cdot kg \cdot sec^{-1}$

$CO\% := 0.13$ $CO_{2\%} := 0.0532$

$O_{2\%} := 0$ $HC\% := 0.0129$

$NOx\% := 0.0000018$

(Assume N2 makes up the rest of the exhaust gas volume.)

$N_{2\%} := 1 - CO\% - CO_{2\%} - HC\% - NOx\% - O_{2\%}$ $N_{2\%} = 0.804$

Calculate Mass Flow Rate of each element entering system:

$$M_{H} := M_{fuel} \cdot MW_{H} \cdot \frac{8}{MW_{C3H8}} \qquad M_{H} = 5.382 \cdot 10^{-4} \cdot kg \cdot sec^{-1}$$

$$M_{C} := M_{fuel} \cdot MW_{C} \cdot \frac{3}{MW_{C3H8}} \qquad M_{C} = 0.002 \cdot kg \cdot sec^{-1}$$

$$M_{O2} := M_{air} \cdot MW_{O2} \cdot \frac{Air_{O2\%}}{MW_{air}} \qquad M_{O2} = 0.006 \cdot kg \cdot sec^{-1}$$

$$M_{N2} := M_{air} \cdot MW_{N2} \cdot \frac{Air_{N2\%}}{MW_{air}} \qquad M_{N2} = 0.021 \cdot kg \cdot sec^{-1}$$

Calculate Mass Flow of Dry Exhaust Gas Exiting System:

$$MW_{Gd} := \left(MW_{CO} \cdot CO\%\right) + \left(MW_{CO2} \cdot CO_{2\%}\right) + \left(MW_{NO} \cdot NOx\%\right) + \left(MW_{HC} \cdot HC\%\right) + \left(MW_{O2} \cdot O_{2\%}\right) + \left(MW_{N2} \cdot N_{2\%}\right)$$

$$MW_{Gd} = 29.058$$

Calculate Mole Fraction of Water per Element and Compare:

Carbon Balance

$$y_{H2OC} := \frac{MW_{C} \cdot M_{total} \cdot (CO\% + CO_{2\%} + HC\%) - M_{C} \cdot MW_{Gd}}{MW_{C} \cdot M_{total} \cdot (CO\% + CO_{2\%} + HC\%) - M_{C} \cdot (MW_{Gd} - MW_{H2O})} \qquad y_{H2OC} = 0.029$$

Hydrogen Balance

$$y_{H2OH} := \frac{MW_{H} \cdot M_{total} \cdot (2.67 \cdot HC\%) - M_{H} \cdot MW_{Gd}}{MW_{H} \cdot M_{total} \cdot (2.67 \cdot HC\% - \omega_{H}) - M_{H} \cdot (MW_{Gd} - MW_{H2O})} \qquad y_{H2OH} = 0.222$$

Oxygen Balance

$$y_{H2OO} := \frac{MW_{O2} \cdot M_{total} \cdot (0.5 \cdot CO\% + CO_{2\%} + 0.5 \cdot NOx\% + O_{2\%}) - M_{O2} \cdot MW_{Gd}}{MW_{O2} \cdot M_{total} \cdot (0.5 \cdot CO\% + CO_{2\%} + 0.5 \cdot NOx\% + O_{2\%} - \omega_{O2}) - M_{O2} \cdot (MW_{Gd} - MW_{H2O})} \qquad y_{H2OO} = 0.158$$

Nitrogen Balance

$$y_{H2ON} := \frac{MW_{N2} \cdot M_{total} \cdot (0.5 \cdot NOx\% + N_{2\%}) - M_{N2} \cdot MW_{Gd}}{MW_{N2} \cdot M_{total} \cdot (0.5 \cdot NOx\% + N_{2\%}) - M_{N2} \cdot (MW_{Gd} - MW_{H2O})} \qquad y_{H2ON} = 0.181$$

APPENDIX E

TEMPERATURE AND SPECIES CONCENTRATION HISTOGRAMS

Histogram plots of temperature and species concentration for the 8-hole module were shown previously in Figures 5.1, 5.2a, and 5.2b. For comparative purposes, the raw data histograms for the other module cases (9-, 10-, 12-, 14-, and 18-hole) are presented on the following pages.

Figures E.1a, E.1b show the temperature histograms for these cases. Each column of histograms corresponds to the particular module case, while each row represents the plane at which the 16 points of data were obtained.

The species concentration profiles are shown in Figures E.2a, E.2b for the 9-hole case; Figures E.3a, E.3b for the 10-hole case; Figures E.4a, E.4b for the 12-hole case; Figures E.5a, E.5b for the 14-hole case; and Figures E.6a, E.6b for the 18-hole case. Each column corresponds to the measured specie (either O_2, CO_2, CO, HC, or NO_x), and each row represents the plane that the data were obtained.

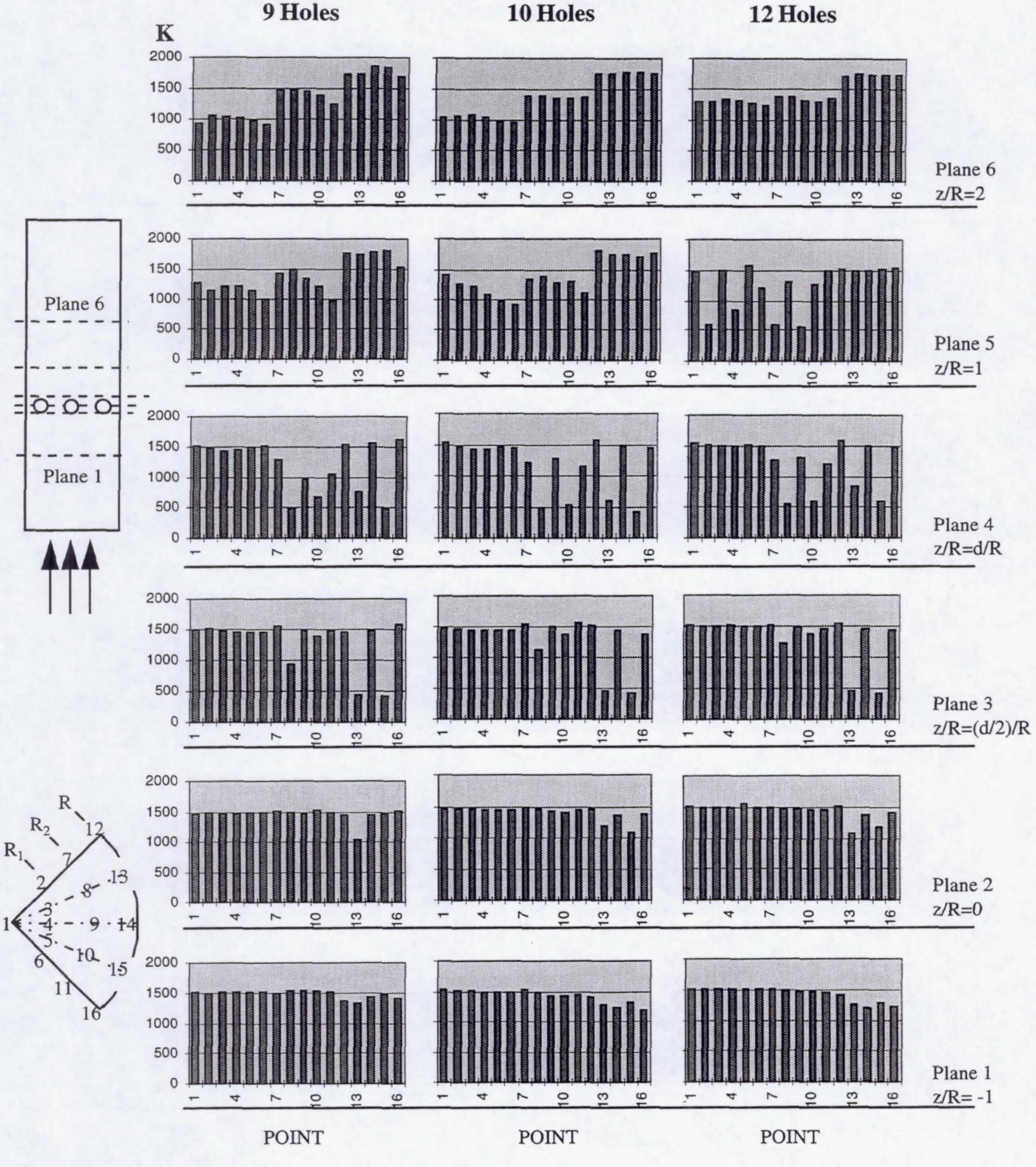

Figure E.1a Temperature Distribution for the 9-, 10-, 12-Hole Modules

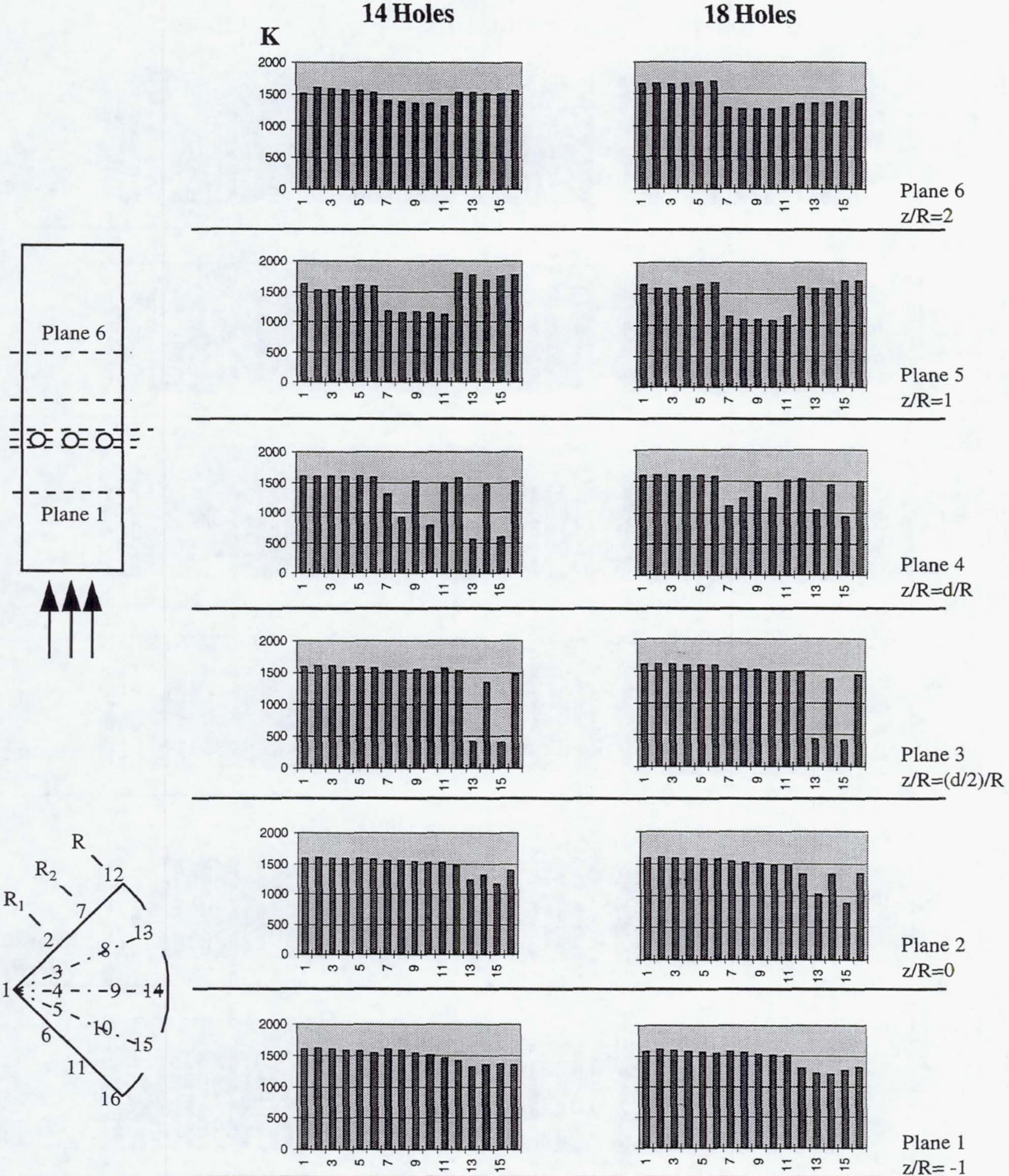

Figure E.1b Temperature Distribution for the 14- and 18-Hole Modules

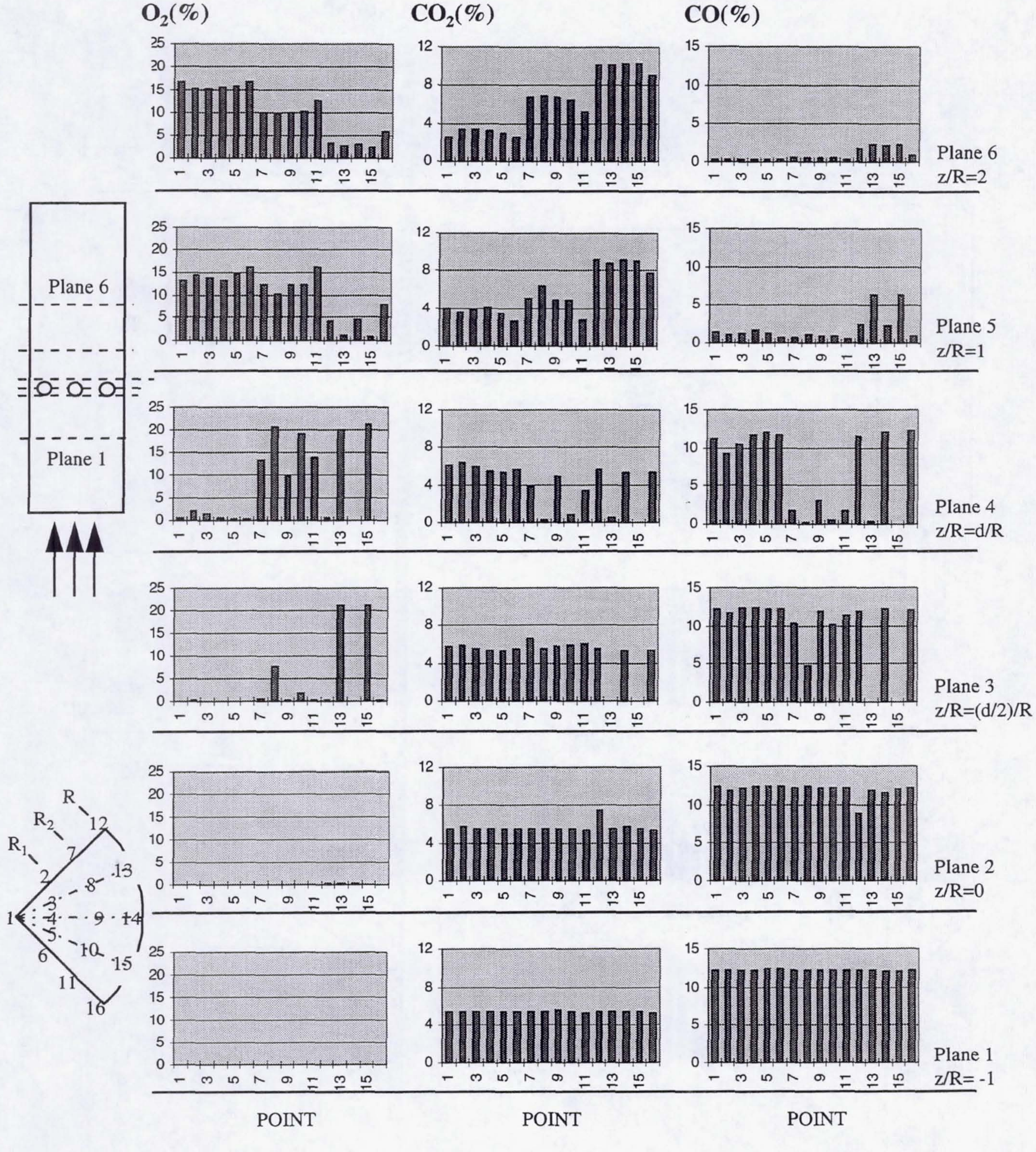

Figure E.2a O_2, CO_2, CO Concentration Distribution for the 9-Hole Module

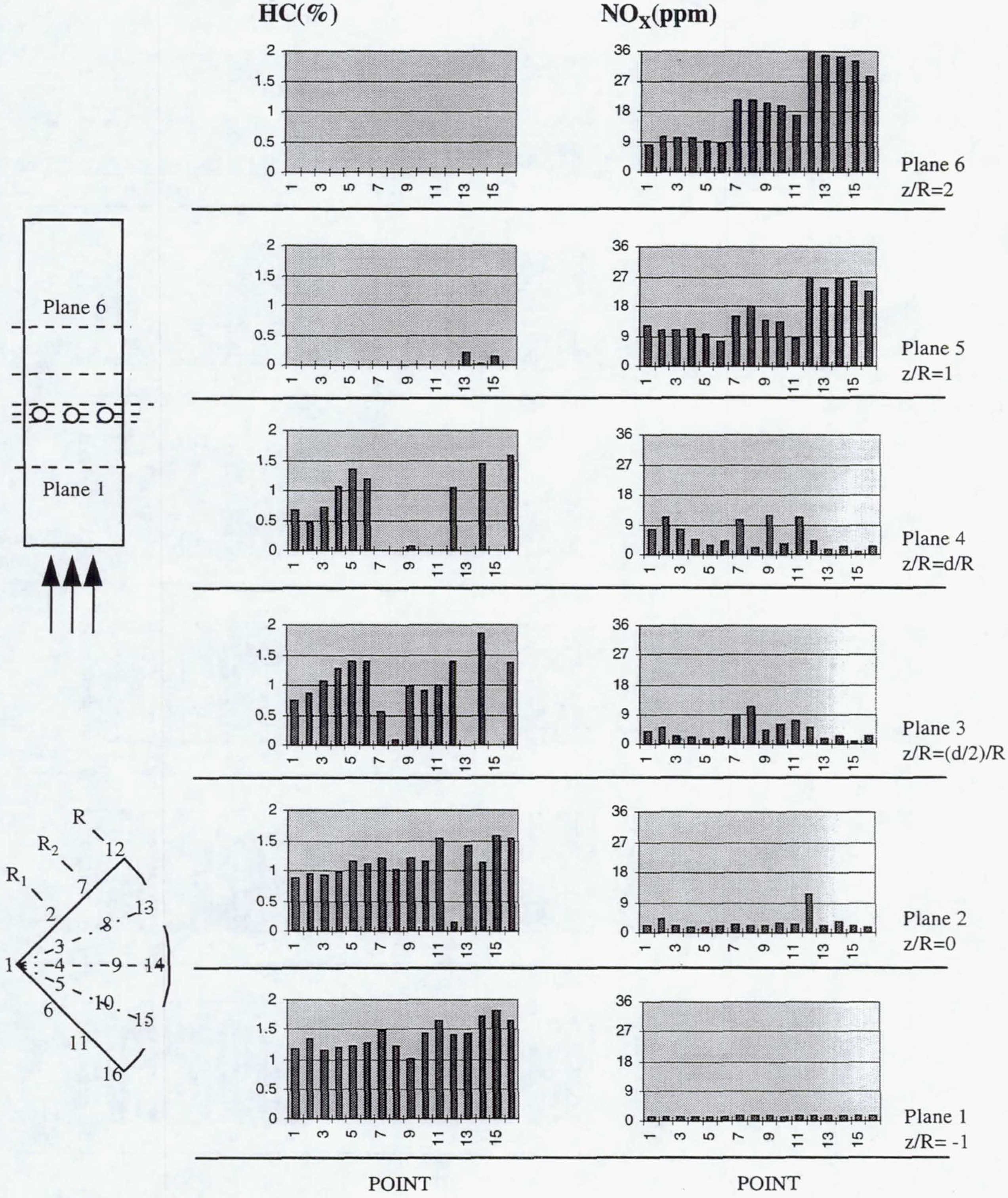

Figure E.2b HC and NO$_X$ Concentration Distribution for the 9-Hole Module

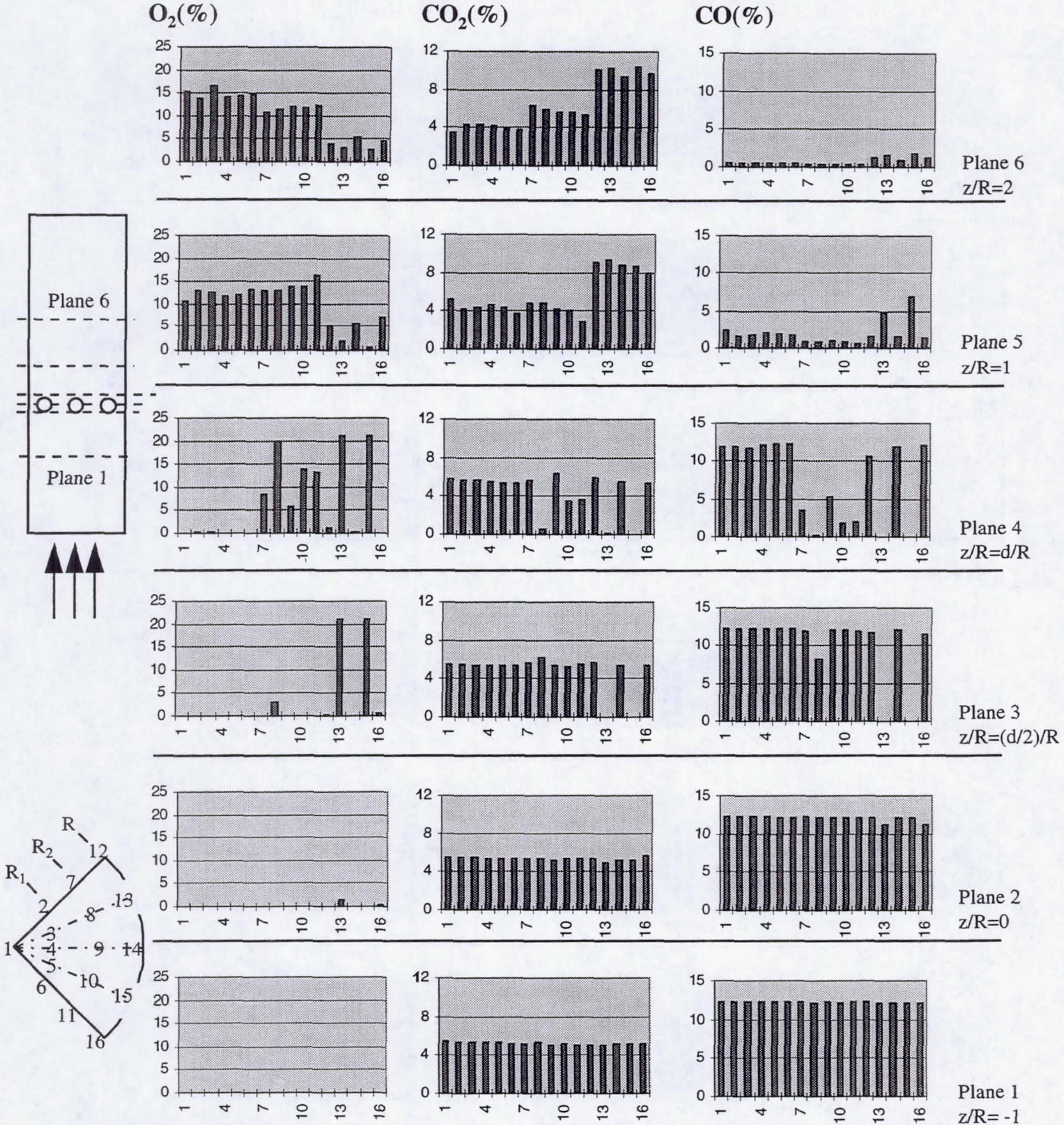

Figure E.3a O_2, CO_2, CO Concentration Distribution for the 10-Hole Module

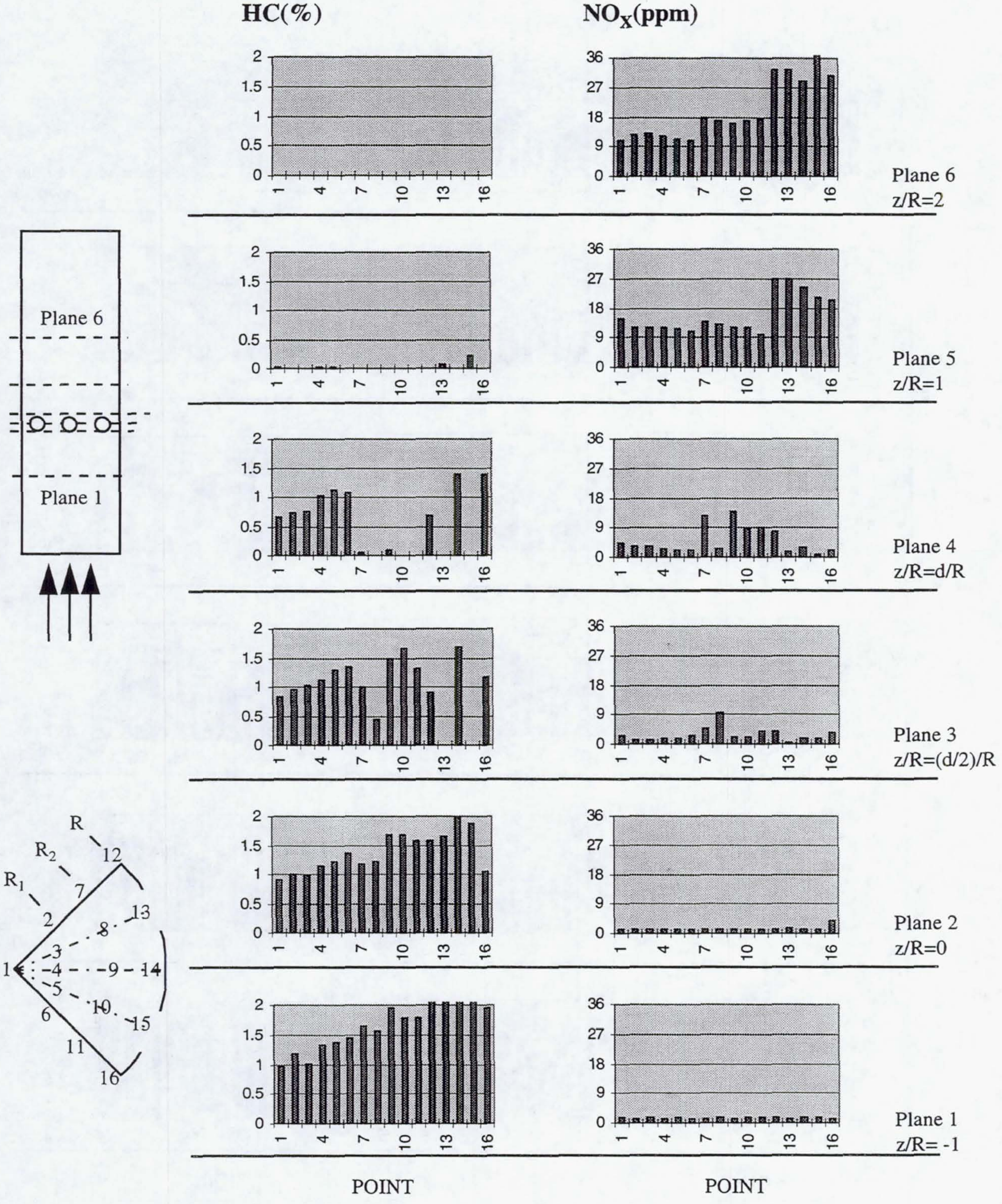

Figure E.3b HC and NO$_X$ Concentration Distribution for the 10-Hole Module

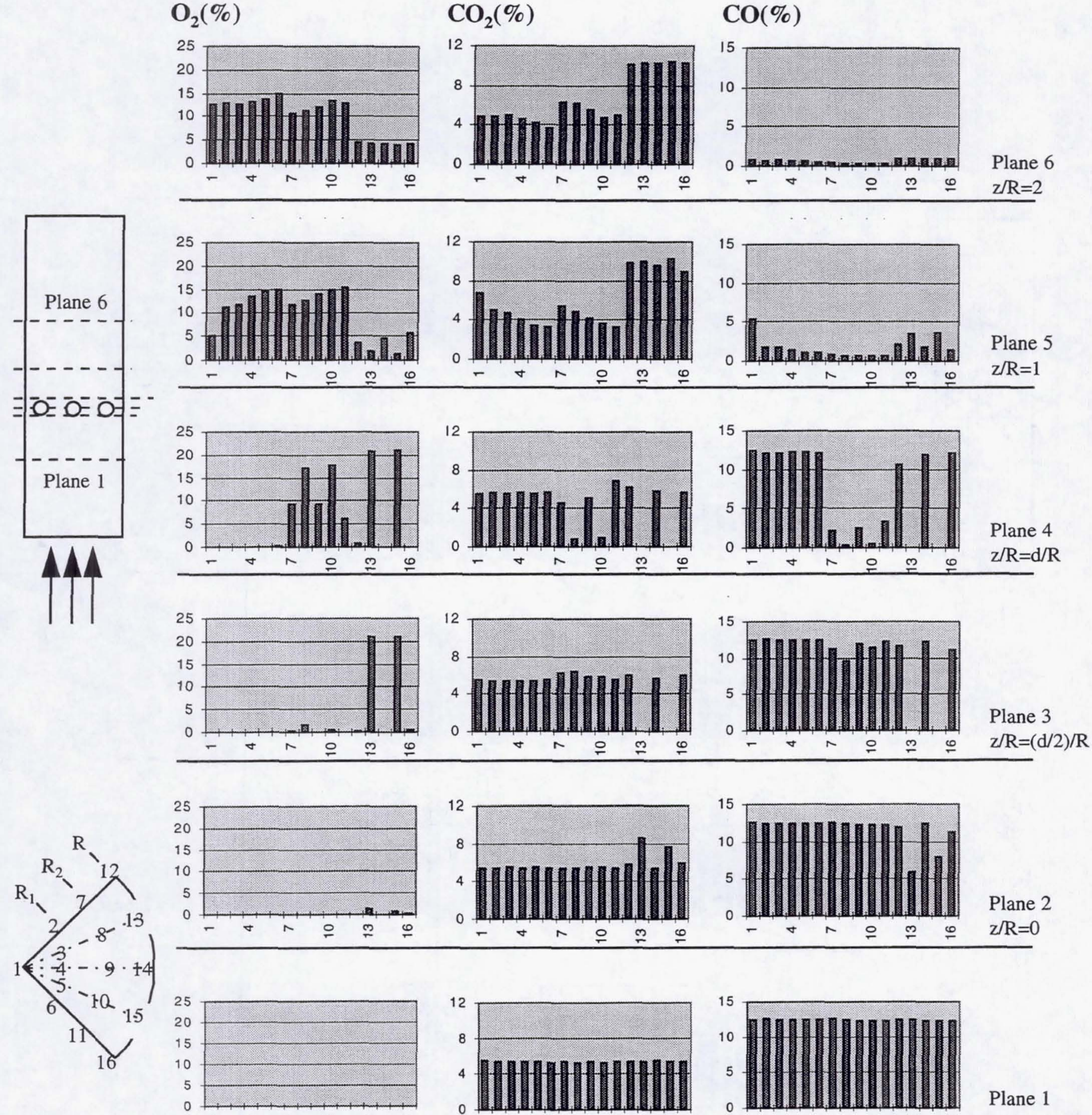

Figure E.4a O_2, CO_2, CO Concentration Distribution for the 12-Hole Module

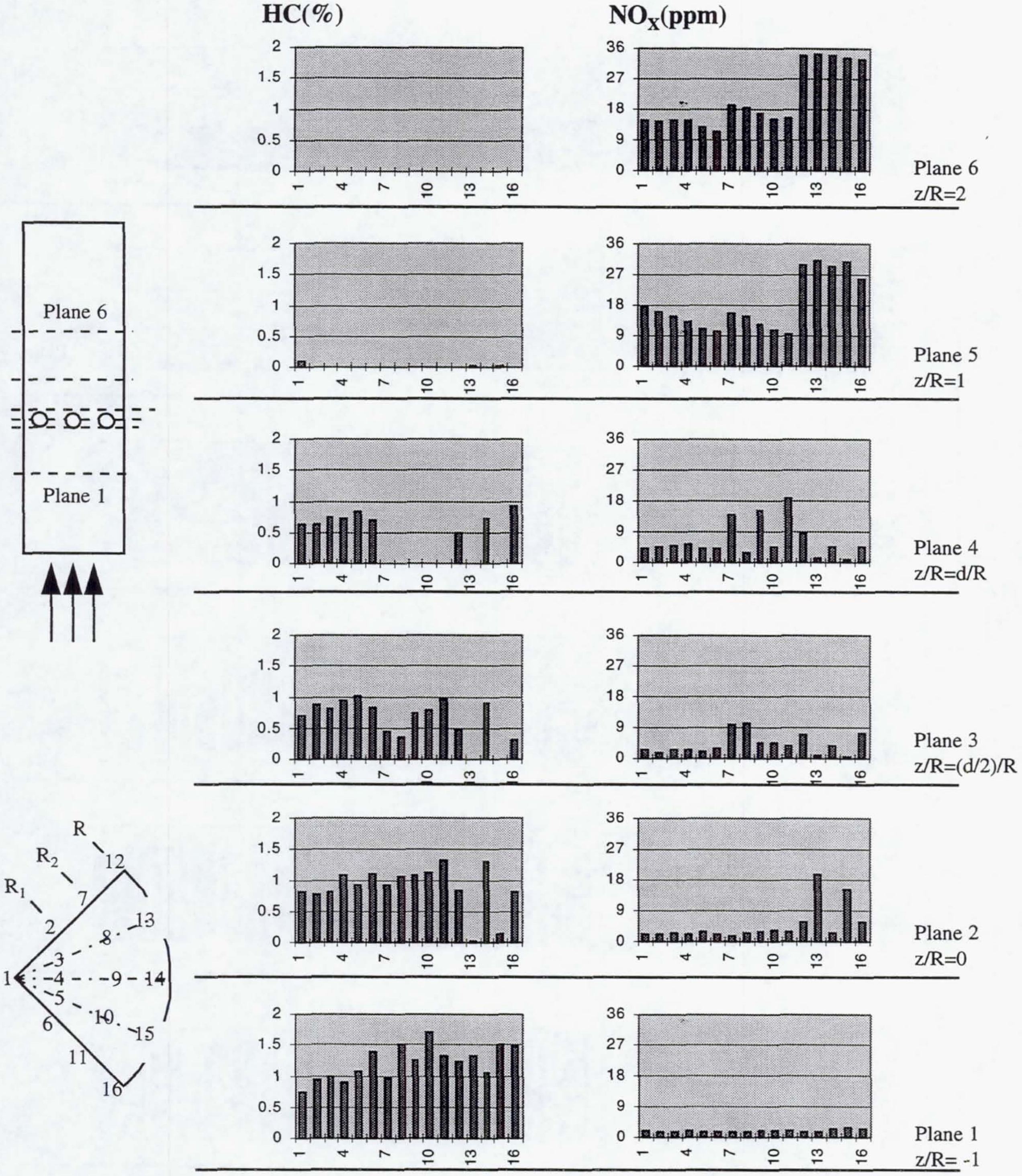

Figure E.4b HC and NO_X Concentration Distribution for the 12-Hole Module

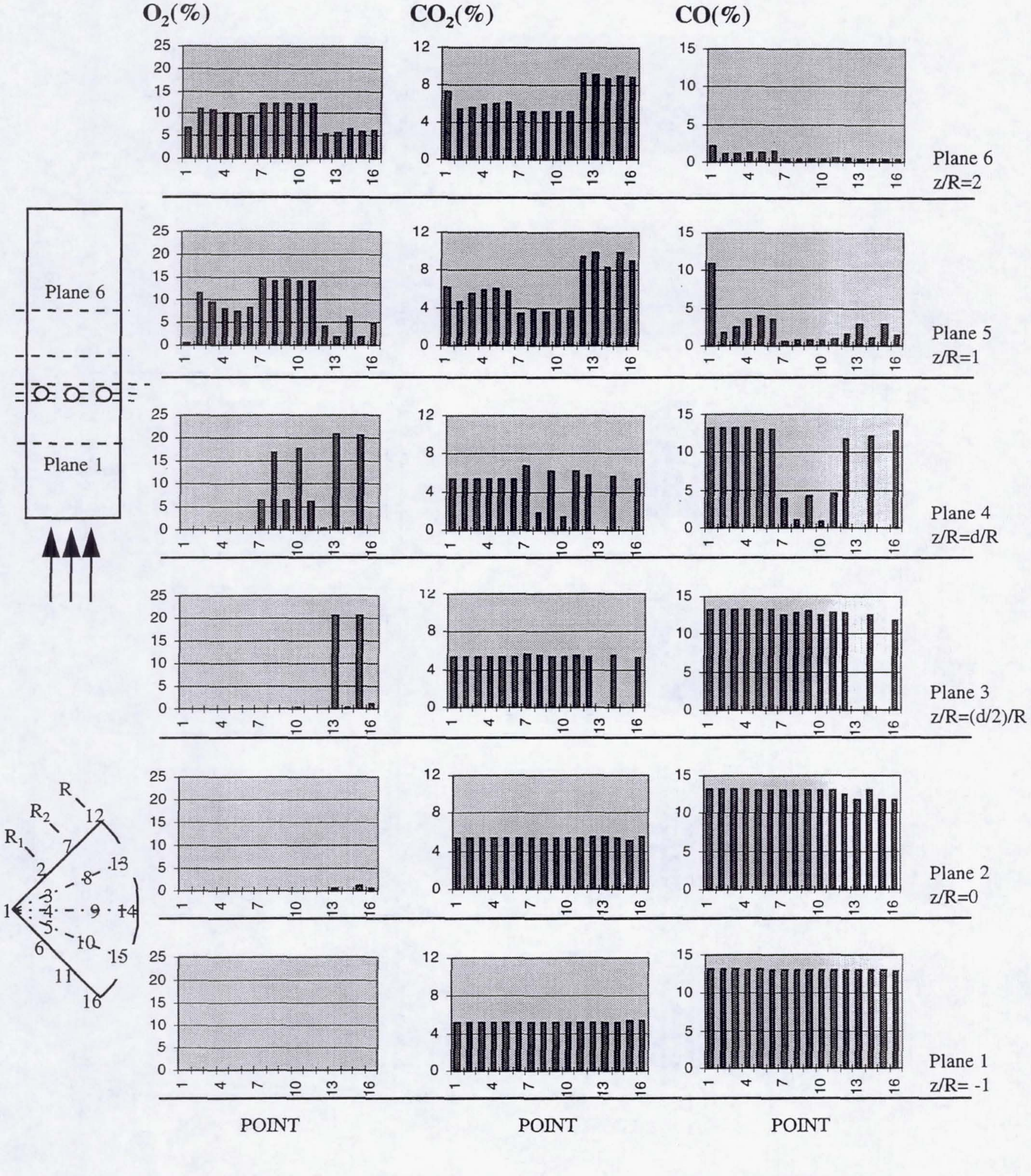

Figure E.5a O_2, CO_2, CO Concentration Distribution for the 14-Hole Module

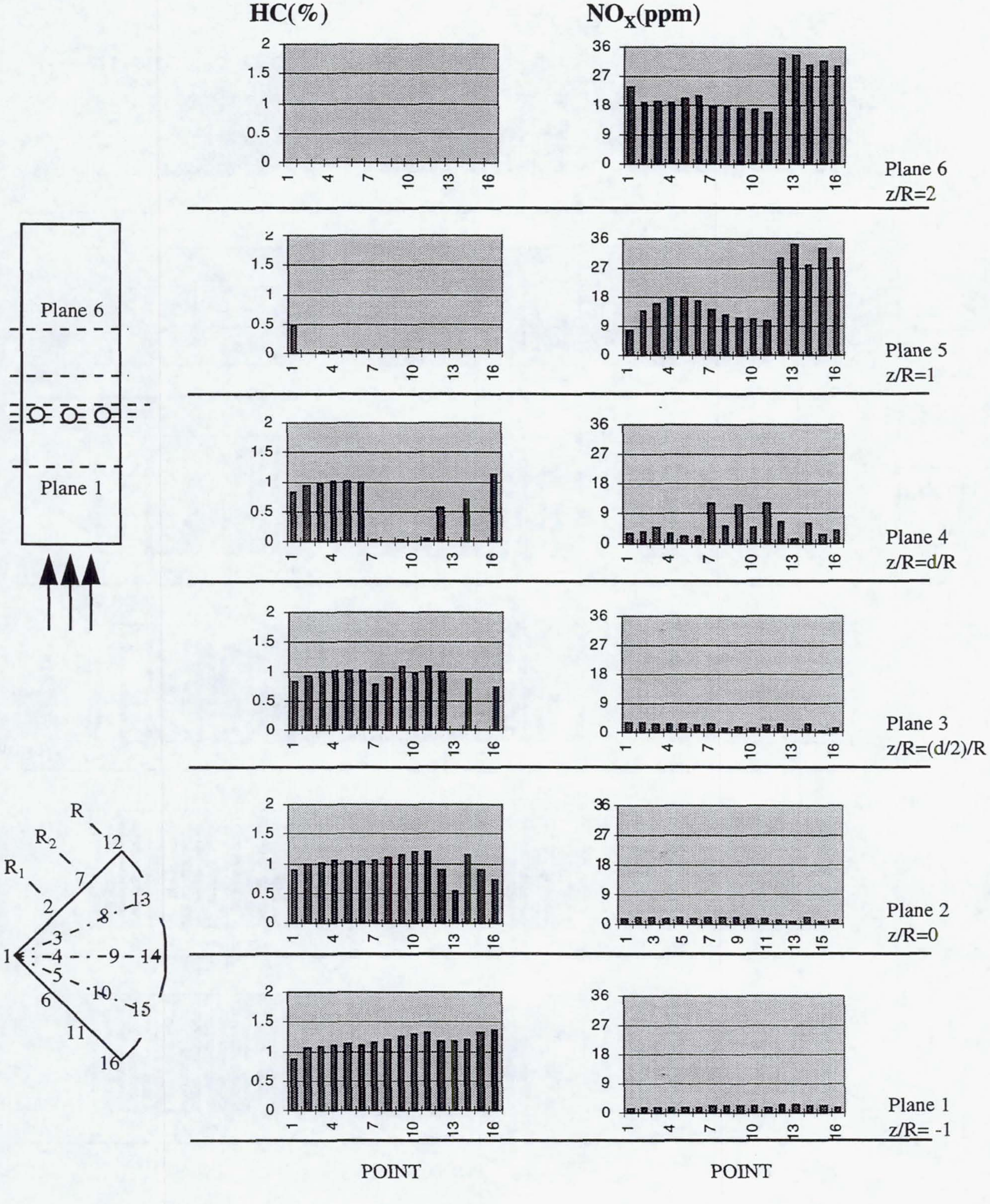

Figure E.5b HC and NO_X Concentration Distribution for the 14-Hole Module

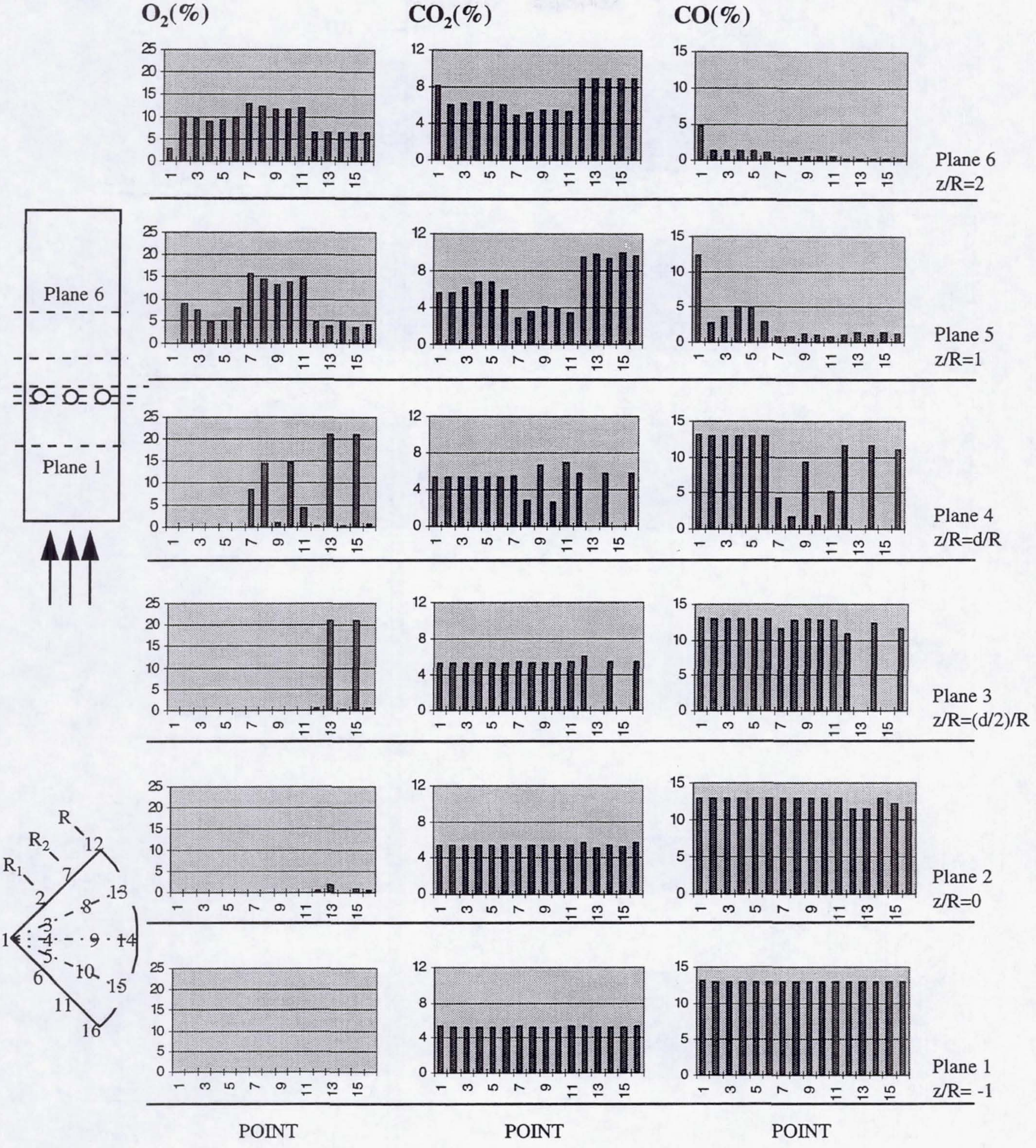

Figure E.6a O_2, CO_2, CO Concentration Distribution for the 18-Hole Module

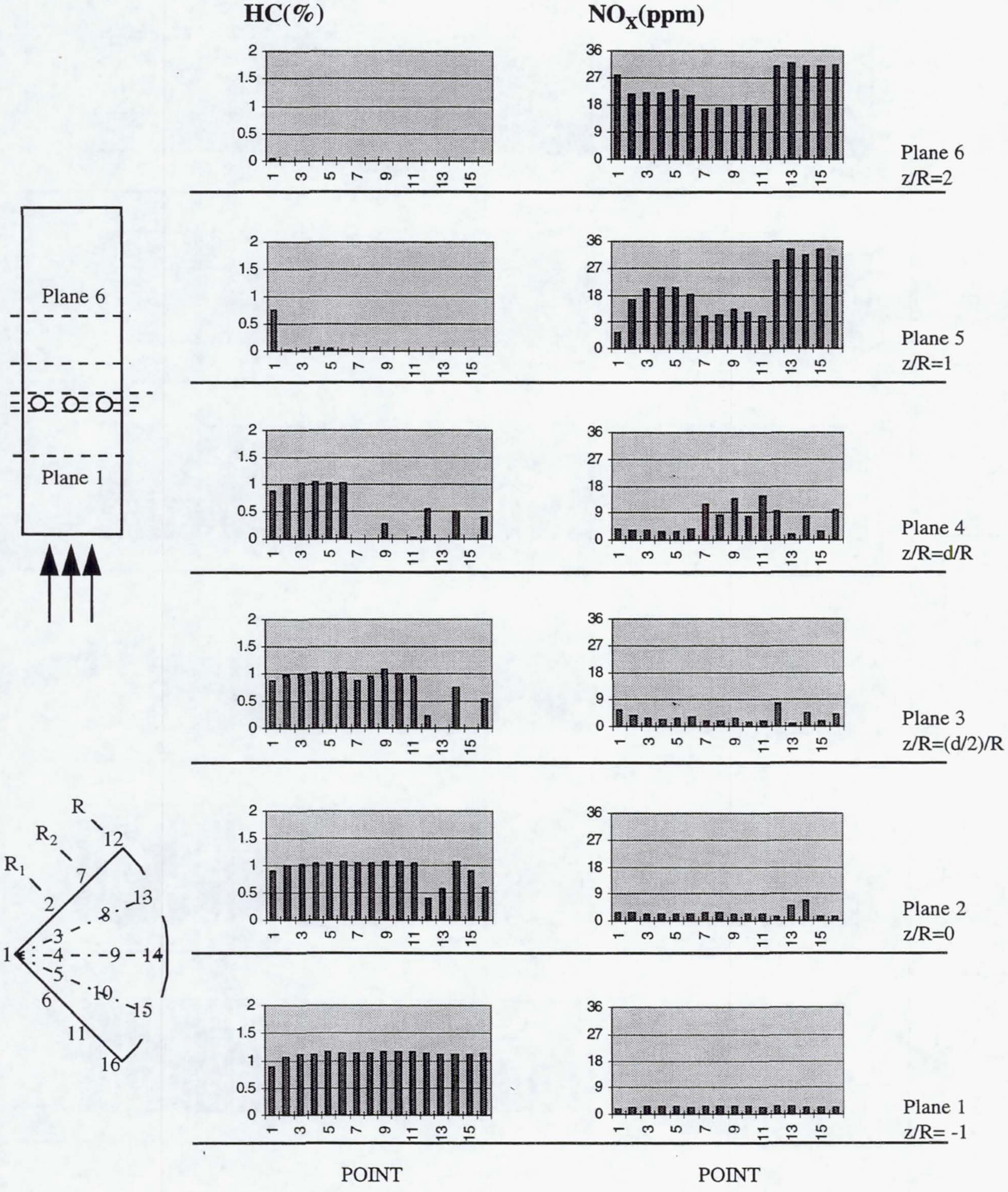

Figure E.6b HC and NO_X Concentration Distribution for the 18-Hole Module

REPORT DOCUMENTATION PAGE

Form Approved
OMB No. 0704-0188

1. AGENCY USE ONLY (*Leave blank*)

2. REPORT DATE
September 1996

3. REPORT TYPE AND DATES COVERED
Final Contractor Report

4. TITLE AND SUBTITLE

Quick-Mixing Studies Under Reacting Conditions

5. FUNDING NUMBERS

WU–537–02–20
G–NAG3–1110

6. AUTHOR(S)

May Y. Leong and G.S. Samuelsen

7. PERFORMING ORGANIZATION NAME(S) AND ADDRESS(ES)

University of California
Irvine California 92697–3550

8. PERFORMING ORGANIZATION REPORT NUMBER

E–9074

9. SPONSORING/MONITORING AGENCY NAME(S) AND ADDRESS(ES)

National Aeronautics and Space Administration
Lewis Research Center
Cleveland, Ohio 44135–3191

10. SPONSORING/MONITORING AGENCY REPORT NUMBER

NASA CR–195375

11. SUPPLEMENTARY NOTES

Project Manager, J. Holdeman, Internal Fluid Mechanics Division, NASA Lewis Research Center, organization code 2650, (216) 433–5846.

12a. DISTRIBUTION/AVAILABILITY STATEMENT

Unclassified - Unlimited
Subject Category 07

This publication is available from the NASA Center for AeroSpace Information, (301) 621–0390.

12b. DISTRIBUTION CODE

13. ABSTRACT ***(Maximum 200 words)***

The low-NO_x emitting potential of rich-burn/quick-mix/lean-burn (RQL) combustion makes it an attractive option for engines of future stratospheric aircraft. Because NO_x formation is exponentially dependent on temperature, the success of the RQL combustor depends on minimizing high temperature stoichiometric pocket formation in the quick-mixing section. An experiment was designed and built, and tests were performed to characterize reaction and mixing properties of jets issuing from round orifices into a hot, fuel-rich crossflow confined in a cylindrical duct. The reactor operates on propane and presents a uniform, non-swirling mixture to the mixing modules. Modules consisting of round orifice configurations of 8, 9, 10, 12, 14, and 18 holes were evaluated at a momentum-flux ratio of 57 and jet-to-mainstream mass-flow ratio of 2.5. Temperatures and concentrations of O_2, CO_2, CO, HC, and NO_x were obtained upstream, downstream, and within the orifice plane to determine jet penetration as well as reaction processes. Jet penetration was a function of the number of orifices and affected the mixing in the reacting system. Of the six configurations tested, the 14–hole module produced jet penetration close to the module half-radius and yielded the best mixing and most complete combustion at a plane one duct diameter from the orifice leading edge. The results reveal that substantial reaction and heat release occur in the jet mixing zone when the entering effluent is hot and rich, and that the experiment as designed will serve to explore satisfactorily jet mixing behavior under realistic reacting conditions in future studies.

14. SUBJECT TERMS

Dilution; Jet mixing flow; Gas turbines; Combustion chamber; Can; Emissions

15. NUMBER OF PAGES
132

16. PRICE CODE
A07

17. SECURITY CLASSIFICATION OF REPORT	**18. SECURITY CLASSIFICATION OF THIS PAGE**	**19. SECURITY CLASSIFICATION OF ABSTRACT**	**20. LIMITATION OF ABSTRACT**
Unclassified	Unclassified	Unclassified	